ON THE STUDY OF NUCLEAR REACTION MECHANISMS USING EXOTIC NUCLEI

by

LUCAS VUSI NDALA

submitted in accordance with the requirements for
the degree of

DOCTOR OF PHILOSOPHY

in the subject

PHYSICS

at the

UNIVERSITY OF SOUTH AFRICA

PROMOTER: PROF. M. L. LEKALA

CO-PROMOTER: DR. B. MUKERU

MAY 2022

Dedication

I dedicate this thesis to my mother, for her love and support and to my loving wife, for being there for me through out this journey and to my lovely kids Musawenkosi and Nkosinathi, for cheering me up.

Acknowledgements

I would like to acknowledge the following people for their support and valuable contribution in the success of my thesis.

- My academic promoters, Prof. M. L. Lekala and Dr. B. Mukeru for their guidance, support, encouragement, discussion during the course of this study.
- National Institute for Theoretical and Computational Sciences (NITheCS), for the financial support that enabled my smooth study progress.
- I would like also to extend my deepest gratitude to Mrs Rene Kotze of NITheCS for commitment, interest, advice and financial assistance through the entire process of this research.
- My darling wife, Kate, and kids, Musawenkosi and Nkosinathi, your love, respect, support and confidence in me, has made my journey so easy to accomplish.
- My mother, Susana and my siblings, Fannie and Lerato, thank you for the love and support that you have given me.
- Above all, I thank the Lord my creator who has made it possible for me to walk and finish this journey with success.

Declaration

I declare that **"ON THE STUDY OF NUCLEAR REACTION MECHANISMS USING EXOTIC NUCLEI"** is my own work and that all the sources that I have used or quoted have been indicated and acknowledged by means of complete references.

.... Date: 11 May 2022

Signature

Ndala LV (Student Number: 67139124)

Summary

We investigated the breakup dynamics of the $^{8}\mathrm{B} + {}^{208}\mathrm{Pb}$, $^{11}\mathrm{Be} + {}^{64}\mathrm{Zn}$, $^{11}\mathrm{Be} + {}^{208}\mathrm{Pb}$, $^{37}\mathrm{Mg} + {}^{208}\mathrm{Pb}$, $^{15}\mathrm{C} + {}^{208}\mathrm{Pb}$, $^{6}\mathrm{Li} + {}^{209}\mathrm{Bi}$ reactions using the continuum discretized coupled channels (CDCC) method. Additionally, we investigated the interesting few-body reaction $^{4}\mathrm{He}_2 + {}^{4}\mathrm{He} \rightarrow {}^{4}\mathrm{He} + {}^{4}\mathrm{He} + {}^{4}\mathrm{He}$ using the CDCC. At a practical level, our choice of these reactions was influenced by the availability of the experimental data on breakup, fusion, and elastic scattering cross sections on one hand, and of the theoretical data on the other which will make the comparison of our results easier. At the fundamental level, these reactions give a window to explore the dynamics of the nuclear reaction mechanisms of exotic nuclei.

It is found that the breakup cross section at deep sub-barrier energies is enhanced when the continuum-continuum couplings are included for the $^{8}\mathrm{B} + {}^{208}\mathrm{Pb}$ reaction. The complete fusion cross section is also enhanced at sub-barrier energies but suppressed at above-barrier energies due to the continuum-continuum couplings. The breakup observables such as total reaction, fusion and breakup cross sections, become almost independent of the ground-state binding energy in the limit approaches zero for the $^{11}\mathrm{Be}+{}^{64}\mathrm{Zn}$ reaction.

It is observed that the first-order perturbation theory can not explain the breakup of a system whose ground state wave function becomes unbound whereas, in the CDCC calculation, when the pure scattering wave function is replaced by the square-integral bin wave functions, the breakup matrix elements have no convergence issues for both $^{11}\mathrm{Be} + {}^{208}\mathrm{Pb}$ and $^{37}\mathrm{Mg} + {}^{208}\mathrm{Pb}$ reactions. We found that the continuum-continuum couplings and higher-order multipole transitions strongly suppress the nuclear breakup cross section compared to the Coulomb breakup cross section in the reaction of $^{15}\mathrm{C}$ nucleus on heavy target. It is found that the resonant states are strongly dominant for lower energies while the non-resonant states are dominant for higher energies for $^{6}\mathrm{Li} + {}^{209}\mathrm{Bi}$ reaction. A strong effect of the Helium-dimer continuum-continuum couplings is found on the elastic and dissociation cross sections in the $^{4}\mathrm{He}_2 + {}^{4}\mathrm{He} \rightarrow {}^{4}\mathrm{He} + {}^{4}\mathrm{He} + {}^{4}\mathrm{He}$ reaction. We then conclude that these couplings are as important in atomic reactions as they are in nuclear reactions, and should be given attention in the analysis of reactions involving loosely-bound molecules.

Keywords: Breakup cross section; Elastic scattering cross section; Complete cross section; Continuum-continuum couplings; Exotic nuclei; Proton- and Neutron-halo nucleus.

Publications

Part of the work of this thesis has been published in the following scientific journals:

- B. Mukeru, **L. V. Ndala** and M. L. Lekala, Deep sub-barrier breakup dynamics in the ^{8}B+^{208}Pb reaction, Pramana - J. Phys. **95** 106 (2021). DOI: https://doi.org/10.1007/s12043-021-02146-5
- B. Mukeru, **L. V. Ndala** and M. L. Lekala, Breakup of s-wave neutron-halo systems with near zero binding energy. Published online on 21 January 2022 with DOI: https://doi.org/10.1016/j.nuclphysa.2022.122397
- B. Mukeru, **L. V. Ndala** and M. L. Lekala, Importance of multi-step processes in the Coulomb and nuclear breakups of 15 C halo nucleus. Published online on 12 March 2022 with DOI: https://doi.org/10.1142/S0218301322500252

Contents

List of Tables

List of Figures

Chapter 1

Introduction

The study of the nuclear reaction mechanisms involving unstable exotic nuclei have been an active area of research [1–9]. Since the discovery of these nuclei in Radioactive Ion Beam facilities more exotic nuclei have become experimentally accessible. These nuclei are short-lived and characterized by the high ratio of neutron (N) to proton (Z) numbers. The most important observed features of exotic nuclei, found in nuclei far from the valley of stability in the nuclear chart, are proton- and neutron-halos. The most well known halo nucleus are the one proton halo ^{8}B, two proton halo ^{7}Ne, one neutron halo ^{11}Be, two neutron halo ^{6}He, two neutron halo ^{11}Li and four neutron halo ^{8}He [10,11]. The halo nucleus is composed of a core nucleus with one or more valence nucleons which are weakly bound. One valence nucleon halo nuclei are described as a two-body model, whereas two valence nucleons halo nuclei are described as a three-body model [12–22]. Some of these halo nuclei reveal Borromean structure whose binary subsystems are unbound [23]. The term Borromean was named after a Renaissance heraldic symbol composed of the three bound rings without bound pairs. The ^{14}Be nucleus is an example of Borromean halo nuclei. This nucleus has a very small binding energy, in which, its relative motion is described as a significant part of the wave function which is defined as a diffuse neutron cloud that is so-called nuclear halo. The term nuclear halos were introduced and used as early as in 1969 [24]. The first experiment of nuclear halo was reported in the 1980s [25]. In this experiment, a large interaction cross section for ^{6}He, ^{8}He and ^{11}Li nuclei, and a large unexpected dipole response function for ^{11}Be nucleus were observed [25,26]. An unexpected large interaction cross section was due to a spatially extended matter distribution or large deformation. In other experiment in 1992 it was concluded that the diffuse neutron cloud was responsible for the large cross section where the quadrupolar deformation of the ^{9}Li and ^{11}Li nuclei were confirmed to be quite similar [27]. The halo nuclei far from the valley of stability are regarded as loosely bound, as a results, in nuclear reactions they show a large breakup probability. Their properties and mechanisms of these nuclei as well as the effects of the core nucleus have been investigated and documented in this field [23, 28–37]. The study of these halo nuclei which reveal novel properties of nuclear and the origin of chemical elements in the nucleosynthesis has received considerable attention within the field of nuclear physics. This makes it interesting to study their properties.

Due to the low breakup threshold the halo nuclei easily breakup by passing through a Coulomb field of a heavy target or once in contact with a target nucleus. In this case, the breakup threshold is regarded as the most important parameter in the breakup process. The importance of the breakup process on any other reaction observables relies on how low this parameter is. From computational point of view, low threshold leads to strong continuum-continuum couplings, owing to the fact that in this case, the ground-state is closer to the continuum. This leads to computational challenges since many continuum-continuum couplings would be required to guarantee convergence of the results, and are thus difficult to handle numerically.

The predominance of the breakup threshold parameter in the breakup process, overshadows any other factor that may be at play in the reaction process. For example, in Ref. [38], larger ^{6}Li breakup cross sections than those corresponding to ^{7}Li were reported, even in Coulomb-dominated reactions. This was understood as due to a lower breakup threshold in the former case (1.47 MeV), compared to (2.47 MeV) in the latter case. However, the Coulomb breakup is known to be dominated by the low-energy Coulomb dipole response, which vanishes for ^{6}Li nucleus, but is nonzero for ^{7}Li nucleus. The Coulomb quadruple response which is much larger for ^{6}Li nucleus, than for ^{7}Li nucleus, amounts to a very small contribution to the breakup cross section. In Ref. [39], the qualitative and quantitative differences in the breakups of these nuclei was also attributed to the difference in their breakup threshold. These results, among many others highlight the fact that the interplay of dynamic effect (related to the projectile-target interaction) is not well understood. It is not yet clear to which extend individual interactions of the projectile fragments with the target nucleus may influence the reaction mechanism.

Some of these reaction mechanisms that occur during the interaction of the projectile nucleus with the target nucleus are elastic breakup and fusion reactions. During a collision, the elastic breakup reaction can happen when none of the fragments are captured by the target. On the other hand, most important fusion reaction that occur are the so-called complete fusion. The complete fusion, in turn, can be separated into two processes, namely direct complete and sequential complete fusions. For direct complete fusion, the whole projectile is fused with the target, while sequential complete fusion can happen when two fragments, after the breakup process, are captured by the target. Incomplete fusion occurs when one of the fragments is fused and the other flies to continuum. The summation of both complete and incomplete fusions can lead to the total fusion.

The Coulomb and nuclear forces are regarded as responsible for the breakup process of the projectile with the target nuclei. In this case the reaction that involve the heavy targets show the Coulomb cross section dominated the nuclear breakup cross section. Due to the short-range nature of nuclear forces and a strong Coulomb repulsion in the interaction region, in a reaction that involve a heavy target is regarded to be dominated by Coulomb breakup. However, it is not clearly established whether the long-range nature of Coulomb forces and the large charge of the target nucleus alone can justify the larger dominance of the Coulomb breakup over the nuclear breakup in reactions involving loosely-bound projectiles, despite the effects on other prevailing reaction dynamics. In the case of a light target, where there is a weak Coulomb repulsion, the reaction is dominated by nuclear breakup. An unambiguous separation of the Coulomb breakup from nuclear breakup remains one of the outstanding challenges in this field. It has been demonstrated that in a Coulomb dominated reaction, the negligible nuclear contribution does not necessarily imply negligible Coulomb-nuclear interference, which give rise to the Coulomb-nuclear interference problem [40–42]. The summation of the Coulomb interaction as well as nuclear interaction is called the Coulomb barrier.

Most studies of the breakup reactions are done at the Coulomb barrier, around and above the incident energies. Very few studies have been done at deep sub-barrier incident energies. Yet it is known that the continuum-continuum couplings are strongly hindered or suppressed at deep sub-barrier energies [43–46]. In this work we investigate breakup reactions at deep sub-barrier energies.

The breakup cross section of the ^{6}Li projectile on different target masses is enhanced as reported in Ref. [47]. Further investigation has to be done for the other loosely-bound reactions with an effort of understanding the important role of the breakup process at deep sub-barrier incident energies in nuclear astrophysics. This study will also address some of the outstanding issues of the origin of the suppression of the complete fusion.

It is believed that the suppression of the complete fusion depends on the projectile binding energies [3]. Other studies suggested that the main cause of the suppression of the complete fusion is other reaction mechanisms [48–52]. It is concluded that a charge clustering contributes towards the complete fusion suppression than a weak projectile binding in Refs. [48, 49]. In this study we aim to share some light on these.

Furthermore, one of the major universal problem of nuclear physics is the investigation of open-quantum reactions which have attracted considerable attention with the recent developments in Ref. [53], with applications in different research fields. In this regards what is not yet clear is how the breakup reaction of an open neutron-halo resemble or differ with that of a loosely-bound reaction. This is an important question that can settle our understanding of the breakup dependence of the breakup threshold. Another interesting question of this study is to verify whether the breakup cross section converges in the breakup of an s-state neutron halo projectile in the zero ground state binding energy limit. This is a challenge to obtained the finite breakup observables in the breakup of an s-wave neutron halo system in the zero binding energy limit. Since the ground-state wave function is unbound, the breakup matrix elements for the transition to and from the ground-state wave will fail to converge and the radial integral which contains the product of the projectile ground-state wave function and scattering scattering wave functions, will oscillate in the same manner as the scattering wave function. This is the case for theoretical methods such as the first-order approximation perturbation theory [54, 55]. However, although there has been a lot of progress in breakup dynamics of loosely-bound nuclear systems, this is not the case for atomic systems. For example, while weakly-bound atoms such as ^{4}He-^{4}He, ^{4}He-^{6}Li, ^{4}He-^{7}Li, have been long identified (see for example Refs. [56–58]), very little is known about their breakup dynamics, contrary to their nuclear counterparts. It is not therefore clear whether the results obtained in nuclear systems can be extended to their atomic counterparts. For example, what is the importance of the continuum-continuum couplings in weakly-bound atomic systems? How does the breakup process affect the elastic scattering cross sections? What is the role of higher-order effects in the breakup of a loosely-bound atomic systems? These, among others, are interesting questions to address in order to understand the breakup dynamics of a weakly-bound atomic system. Investigating this reaction in Refs. [59, 60], it was concluded that due to the hard-core nature of the Helium-dimer potential, higher-order partial-waves should be included in future breakup calculations. Therefore, we aim to check which higher-order partial-waves should be considered in order to guarantee converged breakup cross sections. On the other hand, in Ref. [61], the importance of bound, resonant and non-resonant continuum states are found to be important in the recombination process, where transitions to and from bound-states were investigated. However, this study did not consider transitions between continuum couplings. We will also consider this aspect in the present study. One would expect couplings among continuum states to also play an important role in the reaction under study given the weakly-bound nature of Helium-dimer.

To answer the some of the aforementioned questions, the continuum discretized coupled channels (CDCC) method that includes continuum-continuum couplings is a suitable method and tool to use [62–64]. Due to the importance of these couplings, the adequacy of any theoretical method used to handle such breakup reactions is judged on whether it accurately takes care of these couplings. The formalism has been shown to accurately take into account these couplings. This formalism has been found to be the most adequate theoretical tool to handle breakup reactions induced by weakly-bound projectiles, and is by far the most theoretical tool used in this field. Its popularity in this field comes from the fact that it accurately includes the continuum-continuum couplings, which have been reported to have a large effect on the breakup observables. Starting from the truncation and discretization of the projectile continuum, and after the projectile starting wave functions have been transformed into square-integrable wave functions, it leads to a set of finite coupled differential equations, which are numerically tractable. It has been also utilized to analyze the breakup process of neutron and proton halo reactions, where finite breakup and scattering cross sections were obtained in the ground state binding energy zero limit [65, 66]. In this case, it is found that the ground state

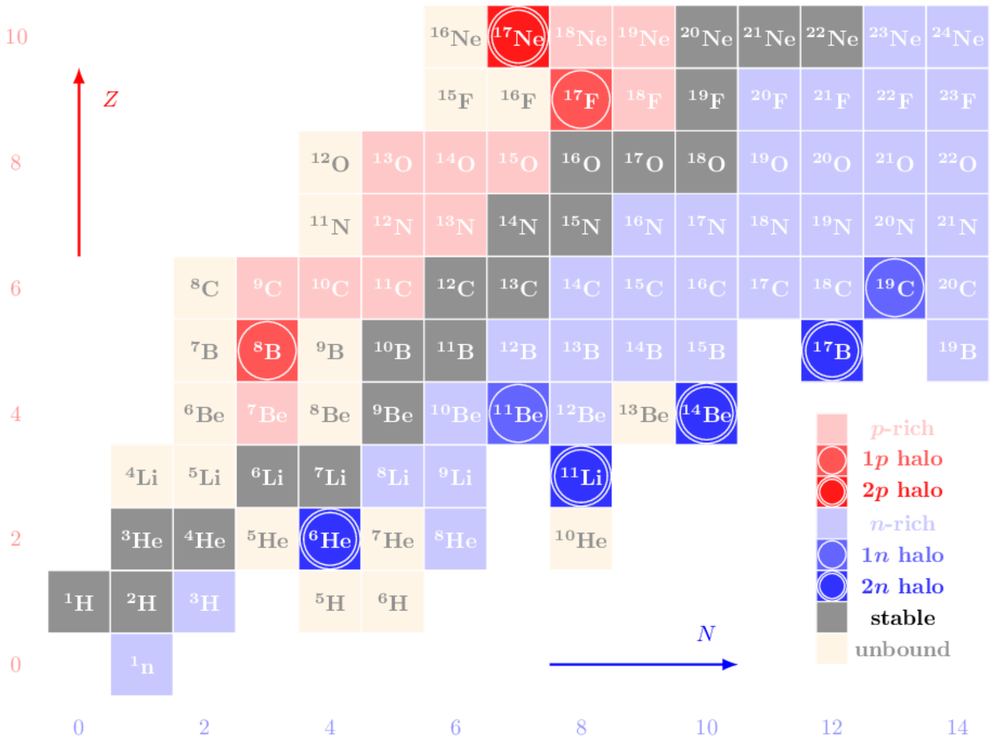

Figure 1.1: A schematic diagram of the halo nuclei taken from Ref. [10].

wave functions remain square-integrable in the zero binding energy limit for both neutron and proton halo reactions due to the centrifugal and the core-proton Coulomb barrier. For this and other reasons it is our method of choice. The numerical calculations of the $^{8}\mathrm{B} + {}^{208}\mathrm{Pb}$, $^{11}\mathrm{Be} + {}^{64}\mathrm{Zn}$, $^{11}\mathrm{Be} + {}^{208}\mathrm{Pb}$, $^{37}\mathrm{Mg} + {}^{208}\mathrm{Pb}$, $^{15}\mathrm{C} + {}^{208}\mathrm{Pb}$, $^{6}\mathrm{Li} + {}^{209}\mathrm{Bi}$, and $^{4}\mathrm{He}_2 + {}^{4}\mathrm{He} \rightarrow {}^{4}\mathrm{He} + {}^{4}\mathrm{He} + {}^{4}\mathrm{He}$ reactions are carried out utilizing the Fresco code [67] programme. The contribution of this study will address some of the questions that will be outlined at the end of this chapter.

1.1 Aims and objectives of the study

The main goal of this study is to contribute towards a better understanding of the dynamics of the breakup processes and their effects on other reaction observables such as elastic scattering and fusion cross sections at deep sub-barrier energies. To this end, our main focus is to investigate the $^{8}\mathrm{B} + {}^{208}\mathrm{Pb}$ reaction at deep sub-barrier, around, and above the Coulomb barrier incident energies in order to make a systematic study.

The objectives of this study are:

- to investigate whether the continuum-continuum couplings will enhance the complete fusion and breakup cross sections at deep sub-barrier incident energies as suggested in Ref. [47]. This will include studying the effect of the continuum-continuum couplings on the complete fusion cross section of the aforementioned reaction in order to understand better the origin of the complete fusion.

- to compare the total fusion, breakup and total reaction cross sections to the conclusions made in Ref. [68].

- to study the dynamics of the breakup of an open neutron-halo $^{11}\text{Be} + {}^{64}\text{Zn}$ reaction in the binding energy ($\varepsilon_b \to 0$). To the best of our knowledge studies of a weakly-bound reaction in this binding energy region are not yet available. This investigation will study the linearity effect of the ground-state wave function on the breakup and elastic scattering cross sections, starting with the convergence analysis.

- to investigate the dependence of the total fusion, breakup, and total reaction cross sections on the binding energy.

- to analyze the breakups of the ^{11}Be and ^{37}Mg neutron halo nuclei on a ^{208}Pb target in the zero ground state binding energy limit. This study intends to elucidate whether the converged breakup cross section can be obtained in this binding energy zero limit in the breakup of an s-state neutron halo projectile. Since the s-wave neutron halo, the matter density extends to infinity and becomes unbound when the binding energy approaches zero due to the hindrance of the centrifugal or Coulomb barrier.

- to study the importance of the higher-order multipole transition and the continuum-continuum couplings effects on the nuclear and Coulomb breakups of the ^{15}C nucleus on heavy target. This reaction is regarded as dominated by Coulomb breakup, due to the large charge target nucleus. The investigation will clarify on whether the large target charge alone can explain the importance of the Coulomb breakup over its nuclear counter part.

- to investigate the effects of resonant and non-resonant states on the breakup cross sections of ^{6}Li nucleus on ^{209}Bi target. This study play an important role in understanding the continuum structure in the breakup of this reaction and also the contribution of the different partial waves of the angular differential breakup cross sections.

- to study the effect of the Helium-dimer continuum-continuum couplings on the elastic and dissociation cross sections in the $^4\mathrm{He}_2 + {}^4\mathrm{He} \rightarrow {}^4\mathrm{He} + {}^4\mathrm{He} + {}^4\mathrm{He}$ reaction. This study will investigate in detail the role of the continuum-continuum couplings in the breakup of an atomic system, the importance of higher-order transitions and the effect of the breakup channel on the elastic scattering cross section.

1.2 Motivation of the study

The study of loosely-bound reactions and nuclear halos is very important in understanding nuclear astrophysics processes. For example, the breakup effect in the $^8\mathrm{B} + {}^{208}\mathrm{Pb}$ reaction at deep sub-barrier incident energies plays an important role in understanding the astrophysical implications of this reaction. This is because this reaction, plays a significant role in the production of high energy neutrinos in the sun [69, 70]. The study is motivated by the recent measurements, where the breakup cross section in the $^8\mathrm{B} + {}^{208}\mathrm{Pb}$ reaction was measured for the first time at $E_{lab} = 30$ MeV [68]. It is therefore important to investigate the reaction dynamics that lead to the predominance of the breakup channel at deep sub-barrier energies, which is not fully elucidated. Another measurement is the complete fusion cross section in the $^{7,8}\mathrm{Li} + {}^{209}\mathrm{Bi}$ reaction [48, 49] which is important to understand how the breakup effect suppresses the complete fusion, which remains an outstanding issue. This study is also motivated by the need to understand the neutron-rich loosely-bound reaction with the binding energy less than 0.1 MeV. For example, the loosely-bound reactions of ^{19}B nuclei with few electronvolts of binding energy are observable [9]. In this case, this study will pave a way of understanding the breakup dynamics. The choice of ^{64}Zn target is motivated by the availability of the breakup cross sections data in the vicinity of the Coulomb barrier and the angular distributions differential elastic cross sections [71]. This study is also motivated by a number of studies of ^{11}Be structure and reactions that are involved with it (for more information see Refs. [72–88]). The interesting thing about the choice of the ^{11}Be and ^{37}Mg projectiles are the unusual properties of a matter density that extends to the peripheral region, due to the weak ground state binding energy compared to tightly bound nuclei. The correlation between the matter density and the ground state binding energy are interesting because they play an important role in the understanding of the breakup reactions induced by loosely bound systems. The importance of studying the Coulomb and nuclear breakups of ^{15}C on heavy target is that the Coulomb is dominant over its nuclear counterpart. The nuclear reaction that involve the heavy target is regarded as Coulomb dominant, whereas for a light target, where there is a weak Coulomb repulsion, the reaction is dominated by nuclear breakup. This is due to the fact that in this case there is a large Coulomb repulsion such that the projectile breakup occurs in the peripheral region where only Coulomb forces are available, given the short-range nature of nuclear forces. The choice of ^{6}Li nucleus is motivated by a low breakup threshold of 1.47 MeV compare to ^{7}Li nucleus with 2.47 MeV. It is established that the breakup heavily depends on the ground state binding energy. That is, if this energy is lower, then the breakup cross section will be larger. In this case, one expects the ^{6}Li breakup cross section to be larger than that of ^{7}Li nucleus. It is also influenced by the continuum states that represents the ^{6}Li breakup of alpha particles and deuteron. Last but not least, we considered the breakup reaction of the Helium trimer (^{4}He$_2$+^{4}He $\rightarrow$ ^{4}He+^{4}He+^{4}He). This is one of the most documented weakly-bound atomic system. The reaction will thus serve as a testing ground of our methods in investigating the dynamics of atomic systems.

1.3 Outline of the thesis

This thesis is organized as follows: Chapter 2 discusses the basic theory of the nuclear scattering which involves the two-body system, three-body system, and fusion reaction mechanism. This chapter also describes the continuum discretized coupled channels (CDCC) method that is used in this study. Chapter 3 presents the results of the investigation of the ^{8}B + ^{208}Pb reaction at deep sub-barrier, around, and above the Coulomb barrier incident energies. Chapter 4 details the results of an open neutron-halo ^{11}Be + ^{64}Zn reaction in the binding energy ($\varepsilon_b \to 0$) and also elucidates the results of the breakup process of the ^{11}Be and ^{37}Mg neutron halo nuclei on a ^{208}Pb target in the zero ground state binding energy limit. Chapter 5 analyses the results of the Coulomb and nuclear breakup cross sections of

^{15}C nucleus on heavy target. Chapter 6 contains the results of the effects of resonant and non-resonant states on the breakup cross sections of ^{6}Li nucleus on ^{209}Bi target. Chapter 7 explains the results of a strong effect of the Helium-dimer continuum-continuum couplings on the elastic and dissociation cross sections in the $^{4}\text{He}_2+{}^{4}\text{He} \rightarrow {}^{4}\text{He}+{}^{4}\text{He}+{}^{4}\text{He}$ reaction. Finally Chapter 8 provides the concluding remarks and future perspectives.

Chapter 2

Theory of nuclear scattering

In this chapter, we discuss the nuclear scattering in the context of the continuum discretized coupled channels (CDCC) method that is used in this study. For simplicity we first discuss in detail a two-body system where the internal structure of the projectile nucleus is taken into account. The method is then extended to describe the three-body system that is composed of a core nucleus and valence fragment of the projectile and target nucleus. Finally, we explain in the framework of this method, how the fusion reaction occurs when the projectile nucleus collides with the target nucleus.

2.1 Two-body system

In two-body system, we assume a system consisting of a core nucleus and fragment, with $\boldsymbol{r}$ their centre of mass coordinate. In our description of the system, we consider an inert core, meaning that the core internal degrees of freedom, such as spin, among others, are not taken into account. The core-fragment relative motion is described by the following Schrödinger equation

$$(H_p - \varepsilon)\, \Phi_\beta^{m_j}(\boldsymbol{k}, \boldsymbol{r}) = 0, \tag{2.1}$$

where H_p, is the Hamiltonian of the system, ε is energy, and $\Phi_\beta^{m_j}(\boldsymbol{k}, \boldsymbol{r})$ the two-body wave function, which is an eigenfunction of the Hamiltonian H_p, and $\boldsymbol{k}$ is the wave number defined in terms of the energy ε of the system as follows

$$k = \sqrt{\frac{2\mu_{cv}\varepsilon}{\hbar^2}}, \tag{2.2}$$

where μ_{cv} is the core-fragment reduced mass. In equation (2.1), the subscript $\beta \equiv (\ell, s, j)$, is a set of quantum numbers that describe the state of the system, with ℓ being the orbital angular momentum associated with the coordinate $\boldsymbol{r}$, s, the fragment spin, j the total orbital angular momentum, obtained from the coupling of the angular momentum ℓ and the spin s ($\boldsymbol{j} = \boldsymbol{\ell} + \boldsymbol{s}$), with m_j, its z-projection. Equation (2.1) can be solved for bound states when $\varepsilon < 0$ and scattering states when $\varepsilon > 0$. The Hamiltonian H_p is given by

$$\begin{aligned} H_p &= -\frac{\hbar^2}{2\mu_{cv}}\nabla^2_{\boldsymbol{r}} + V_{cv}(r) \\ &= T_r + V_{cv}(r), \end{aligned} \tag{2.3}$$

where the first term represents the kinetic energy term ($\nabla^2_{\boldsymbol{r}}$ is the usual nabla operator), and $V_{cv}(r)$, is the core-fragment interacting potential. In spherical coordinates, the kinetic energy operator is determined as

$$-\frac{\hbar^2}{2\mu_{cv}}\nabla^2_{\boldsymbol{r}} = -\frac{\hbar^2}{2\mu_{cv}}\left[-\frac{1}{r^2}\frac{\partial}{\partial r}\left(r^2\frac{\partial}{\partial r}\right) + \frac{\hat{\ell}^2}{r^2}\right], \tag{2.4}$$

where $\hat{\ell}$ is the orbital angular momentum operator and is given by the following expression

$$\hat{\ell} = -\hbar^2\left[\frac{1}{\sin^2\theta_r}\frac{\partial^2}{\partial\varphi_r^2} + \frac{1}{\sin\theta_r}\frac{\partial}{\partial\varphi_r}\left(\sin\theta_r\frac{\partial}{\partial\varphi_r}\right)\right], \tag{2.5}$$

with its z-component given by

$$\hat{\ell}_z = \frac{\hbar}{i}\frac{\partial}{\partial\varphi_r}, \tag{2.6}$$

where (θ_r, φ_r) are the angular coordinates of the vector $\boldsymbol{r}$, and r, its radial coordinate. The wave function $\Phi_\beta^{m_j}(\boldsymbol{k}, \boldsymbol{r})$, which is an eigenfunction of the Hamiltonian H_p, can be written as

$$\Phi_{\beta}^{m_j}(\boldsymbol{k},\boldsymbol{r}) = \frac{\phi_{\ell}^{j}(k,r)}{r}\left[Y_{\ell}^{m_\ell}(\Omega_r)\otimes X_s^{\nu}\right]_{jm_j}, \tag{2.7}$$

where $\phi_{\ell}^{j}(k,r)$, is the radial wave function, $Y_{\ell}(\Omega_r)$, is a spherical Harmonics, with $\Omega = (\theta_r, \varphi_r)$, a solid angle in the direction of $\boldsymbol{r}$ expressed in spherical coordinates, and X_s , the spin wave function. The radial wave function satisfy the following radial Schrödinger equation

$$\left[-\frac{\hbar^2}{2\mu_{cv}}\left(\frac{d^2}{dr^2}-\frac{\ell(\ell+1)}{r^2}\right)+V_{cv}(r)-\varepsilon\right]\phi_{\ell}^{j}(k,r)=0. \tag{2.8}$$

The potential $V_{cv}(r)$ is a crucial input that enters this equation. It contains both nuclear and Coulomb terms, i.e.,

$$V_{cv}(r) = V_{nucl}(r) + V_{Coul}(r), \tag{2.9}$$

where $V_{nucl}(r)$, and $V_{Coul}(r)$, are respectively the nuclear and Coulomb components. When the orbital angular momentum is nonzero ($\ell \neq 0$), the nuclear potential contains two terms, a central term, and a spin-orbit coupling term. Different parametrisations of the nuclear potential exist in literature. In the present work, we adopt the Woods-Saxon shape and write the nuclear potential $V_{nucl}(r)$ as

$$\begin{aligned} V_{nucl}(r) &= V_c(r) + V_{\rm so}(r) \\ &= V_0 f(r, R_0, a_0) + V_{\rm so}(\boldsymbol{\ell}\cdot\boldsymbol{s})\left(\frac{\hbar}{m_\pi c}\right)^2\frac{1}{r}\frac{d}{dr}f(r, R_{\rm so}, a_{\rm so}) \end{aligned} \tag{2.10}$$

where V_0, and $V_{\rm so}$, are the depths of the central and spin-orbit coupling terms , (R_0, $R_{\rm so}$) and (a_0, $a_{\rm so}$), the corresponding absolute nuclear radii and diffuseness, respectively, $(\boldsymbol{\ell}\cdot\boldsymbol{s}) = (j^2-\ell^2-s^2)/2$, is the spin-orbit coupling, m_π, the pion mass, and c, the spin of the light in the vacuum. The absolute nuclear radii are given by $R_x = r_x\left(A_c^{1/3} + A_v^{1/3}\right)$ (r_x is the reduced radius), with A_c core and $A_v = 1$, being the core nucleus and fragment atomic mass numbers. The function $f(r, R_x, a_x)$ ($x \equiv 0, \rm so$) is given by

$$f(r, R_x, a_x) = \frac{1}{1+\exp\left[(r-R_x)/a_x\right]}. \tag{2.11}$$

The nuclear potential is naturally short-ranged, meaning that $V_{nucl}(r) \rightarrow 0$, for $r \geq R_x$. The Coulomb potential is generally given by a point-charge as

$$V_{Coul}(r) = \begin{cases} \frac{Z_c Z_v e^2}{R_c} & r > R_c \\ \left(\frac{3}{2} - \frac{r^2}{2R_c^2}\right) & r \leq R_c, \end{cases} \tag{2.12}$$

where $R_c = r_c \left(A_c^{1/3} + A_v^{1/3}\right)$ is the Coulomb radius with r_c reduced Coulomb radius.

2.1.1 Scattering states

When the core and fragment are far away from each other in the continuum, the nuclear component of the potential $V(r)$ vanishes, due to its short-range nature and only its Coulomb component is available. In this case, the potential $V(r)$ looses its attractive nature, and the scattering wave functions $\phi_\ell^j(k,r)$ are normalized in the asymptotic region $(r \rightarrow \infty)$ according to

$$\phi_\ell^j(k,r) \overset{r\rightarrow\infty}{\rightarrow} F_\ell(\eta, kr)\cos\delta_\ell(k) + G_\ell(\eta, kr)\sin\delta_\ell(k), \tag{2.13}$$

where $\delta_\ell(k)$ is the nuclear phase shift and $F_\ell(z)$ and $G_\ell(z)$ are Coulomb functions, [89], and they are asymptotically defined as

$$\begin{aligned} F_\ell(\eta, kr) &\overset{r\rightarrow\infty}{\rightarrow} \sin\left[kr - \eta\ln(2kr) - \frac{\pi}{2}\ell + \sigma_\ell^\eta\right] \\ G_\ell(\eta, kr) &\overset{r\rightarrow\infty}{\rightarrow} \cos\left[kr - \eta\ln(2kr) - \frac{\pi}{2}\ell + \sigma_\ell^\eta\right], \end{aligned} \tag{2.14}$$

where σ_ℓ^η is the Coulomb phase shift given by

$$\begin{aligned} \sigma_\ell^\eta &= \frac{1}{2i}\ln\left[\frac{\Gamma(\ell+1+i\eta)}{\Gamma(\ell+1-i\eta)}\right] \\ &= \arg\Gamma(\ell+1-i\eta), \end{aligned} \tag{2.15}$$

with η the Sommerfeld parameter defined as

$$\eta = \frac{\mu_{cv}}{\hbar^2}\frac{Z_c Z_v e^2}{k}, \tag{2.16}$$

with $Z_c e$ and $Z_v e$, the core and fragment charges, respectively. When the fragment is a neutron ($Z_v e = 0$), equation (2.14) reduces to

$$\begin{aligned} F_\ell(0,kr) &\overset{r\to\infty}{\to} \sin\left(kr - \frac{\ell\pi}{2}\right) \\ G_\ell(0,kr) &\overset{r\to\infty}{\to} \cos\left(kr - \frac{\ell\pi}{2}\right). \end{aligned} \tag{2.17}$$

The substitution of equation (2.17) into (2.13), gives

$$\begin{aligned} \phi_\ell^j(k, r\to\infty) &\to \sin\left(kr - \frac{\ell\pi}{2}\right)\cos\delta_\ell(k) + \cos\left(kr - \frac{\ell\pi}{2}\right)\sin\delta_\ell(k) \\ &\to \sin\left[kr - \frac{\ell\pi}{2} + \delta_\ell(k)\right]. \end{aligned} \tag{2.18}$$

For $\ell = 0$ (s-state) the equation (2.18) reduces to

$$\phi_\ell^j(k,r) \overset{r\to\infty}{\to} \sin\left[kr + \delta_{\ell_0}(k)\right]. \tag{2.19}$$

To accurately describe the core-fragment breakup process, one needs the exact scattering wave functions $\psi^{(+)}_{\boldsymbol{k}m_\ell\nu}(\boldsymbol{k}, r)$, which are obtained by the following expansion

$$\psi^{(+)}_{\boldsymbol{k}m_\ell\nu}(\boldsymbol{k}, r) = \sum_\beta C_\beta \Phi_\beta^{m_j}(\boldsymbol{r}), \tag{2.20}$$

where C_β are the expansion coefficients to be determined. In the asymptotic region, the wave function $\psi^{(+)}_{\boldsymbol{k}m_\ell\nu}(\boldsymbol{k}, r)$ is a sum of an incoming Coulomb function and an outgoing spherical wave, i.e

$$\psi^{(+)}_{\boldsymbol{k}m_\ell\nu}(\boldsymbol{k}, r) \overset{r\to\infty}{\to} \psi_C(\boldsymbol{k}, r)X_s + \frac{e^\Theta}{r}\sum_{\nu'} f'_\nu(\Omega_r)X'_s, \tag{2.21}$$

where $\psi_C(\boldsymbol{k}, r)$ is the Coulomb wave function, f'_ν the scattering amplitude, and

$$\Theta = ikr - \eta\ln(2kr). \tag{2.22}$$

In order to determine the coefficient C_β, we first expand the Coulomb wave function in partial waves as follows,

$$\psi_C(\boldsymbol{k}, r) = \frac{4\pi}{kr}\sum_{\ell m_\ell} i^\ell e^{\sigma_\ell(k)} F_\ell(\eta, kr) Y_\ell^*(\Omega_k) Y_\ell(\Omega_r) X_s, \tag{2.23}$$

where $Y_\ell(\Omega_k)$ is the spherical harmonic associated with the wave number vector $\boldsymbol{k}$, and where $\Omega_k \equiv (\theta_k, \varphi_k)$ is the solid angle in the direction of $\boldsymbol{k}$. From equation (2.7), we can deduce that

$$X_s = \sum_j \langle \ell m_\ell s\nu | j m_j \rangle \left[Y_\ell(\Omega_r) \otimes X_s \right]_{jm_j}, \tag{2.24}$$

such that equation (2.23), reduces to

$$\begin{aligned} \psi_C(\boldsymbol{k}, r) X_s &= \frac{4\pi}{kr}\sum_{\ell m_\ell} i^\ell e^{i\sigma_\ell(k)} F_\ell(\eta, kr) Y_\ell^*(\Omega_k) \\ &\times \sum_j \langle \ell m_\ell s\nu | j m_j \rangle \left[Y_\ell(\Omega_r) \otimes X_s \right]_{jm_j}, \end{aligned} \tag{2.25}$$

comparing equation (2.25) with equation (2.20), the coefficients C_β can be identified as

$$C_\beta = \frac{4\pi}{kr} e^{i[\delta_\ell(k) + \sigma_\ell(k)]} \sum_{m_\ell} \langle \ell m_\ell s\nu | j m_j \rangle \, Y_\ell^{m_\ell *}(\Omega_k). \tag{2.26}$$

2.1.2 Resonant states

The resonant states have the following asymptotic behavior

$$\phi_\ell^j(k, r) \overset{r\to\infty}{\to} e^{-ik} - S_\ell(k) e^{ik}, \tag{2.27}$$

with $S_\ell(k)$ the scattering S-matrix element. The resonance behavior is associated with the resonance amplitude f_{res}, given by

$$\begin{aligned} f_{res} &\simeq -\frac{1}{k}\left[\frac{\Gamma/2}{(\varepsilon - \varepsilon_r) + i\Gamma/2} \right] \\ &= \frac{i}{2ik}\left(e^{2i\delta_{res}} - 1 \right), \end{aligned} \tag{2.28}$$

where ε_r is the resonance energy and Γ the resonance width, and δ_{res}, the resonance phase shift. This equation (2.28) is used with the trigonometrical relation

$$\tan(2\delta) = \frac{2\tan\delta}{1-\tan^2\delta}, \tag{2.29}$$

to obtain the resonant phase shift defined as

$$\delta_{res} = \tan^{-1}\left[\frac{\Gamma/2}{\varepsilon-\varepsilon_r}\right]. \tag{2.30}$$

In the case of resonance the angle integrated cross section will reduced to

$$\begin{aligned}\sigma_{res} &\simeq \frac{4\pi}{k^2}(2\ell+1)\sin^2\delta_{res} \\ &= \frac{4\pi}{k^2}(2\ell+1)\frac{\Gamma^2/4}{(\varepsilon-\varepsilon_r)^2+\Gamma^2/4},\end{aligned} \tag{2.31}$$

with

$$\begin{aligned}\sin\delta_{res} &= \frac{\tan\delta_{res}}{\sqrt{1+\tan^2\delta_{res}}} \\ &= \frac{\Gamma/2}{\sqrt{(\varepsilon-\varepsilon_r)^2+\Gamma^2/4}},\end{aligned} \tag{2.32}$$

to obtained

$$\sigma_{res} \simeq \frac{\pi}{k^2}(2\ell+1)\left[\frac{\Gamma^2}{(\varepsilon-\varepsilon_r)^2+\Gamma^2/4}\right], \tag{2.33}$$

where $\Gamma = \tau\hbar$ is associated with the half-life

$$\begin{aligned}t_{\frac{1}{2}} &= \frac{\ln 2}{\tau} \\ &= \frac{\hbar}{\Gamma}\ln 2.\end{aligned} \tag{2.34}$$

2.1.3 Bound states

For bound states the two-body system have the following asymptotic boundary conditions ($r \to \infty$)

$$\phi_{\ell_0}^{j_0}(k_0, r) \overset{r\to\infty}{\to} C_{\ell_0,j_0} W_{-\eta_0,\ell_0+\frac{1}{2}}(2k_0 r), \tag{2.35}$$

where C_{ℓ_0,j_0} is the asymptotic normalization constant (ANC) and $W_{-\eta_0,\ell_0+\frac{1}{2}}(2k_0 r)$ a Whittaker function [89], where $k_0 = ik = i\sqrt{\frac{2\mu_{cv}\varepsilon_0}{\hbar^2}}$ ($\varepsilon_0 < 0$, is the core-fragment binding energy) is the ground-state wave number, and $\eta_0 = -i\eta$, with η, given by equation (2.16). In the asymptotic region, the Whittaker function reads

$$W_{-\eta_0,\ell_0+\frac{1}{2}}(2k_0 r) \to \exp[-k_0 r + \eta_0 \ln(2k_0 r)]. \tag{2.36}$$

For a neutron fragment where $\eta_0 = 0$, equation (2.35) becomes

$$\phi_{\ell_0}^{j_0}(k_0, r) \overset{r\to\infty}{\to} C_{\ell_0,j_0} k_0 r h_{\ell_0}^{+}(k_0 r), \tag{2.37}$$

where $h_{\ell_0}^{+}(k_0 r)$, is the spherical Hankel function [89]. In the asymptotic region, the wave function becomes

$$\phi_{\ell_0}^{j_0}(k_0, r) \overset{r\to\infty}{\to} C_{\ell_0,j_0} \exp(-k_0 r). \tag{2.38}$$

2.1.4 Bound-state wave functions in the $\varepsilon_0 \to 0$ limit

As we have indicated elsewhere in the work, one of the characteristic of halo and other loosely-bound systems is a large spacial extension to peripheral region of the bound-state wave function, as a consequence of the small binding energy. Therefore, for an extremely weak binding energy ($\varepsilon_0 \to 0$), the core-neutron bound-state wave function can extend to infinity, particularly for an s-wave bound-state, where there is neither Coulomb nor centrifugal barrier to confine the neutron within the core nucleus field. For a discussion on bound-state wave functions in the zero binding energy limit, an interested reader can find more details in Ref. [90]. In order to derive the bound-state wave function in this limit for a proton-halo system, we recall that the Whittaker function $W_{-\eta_0,\ell_0+\frac{1}{2}}(2k_0r)$ can be written in terms of the outgoing Coulomb wave function $H_\ell^+(\eta_0,k_0r)$ as follows

$$W_{-\eta_0,\ell_0+\frac{1}{2}}(2k_0r) = H_\ell^+(\eta_0,k_0r)\exp\left(i\frac{\eta_0\pi}{2}+\frac{\ell_0\pi}{2}-i\sigma_{\ell_0}^{\eta_0}\right). \tag{2.39}$$

From the standard properties of the Coulomb functions and following Ref. [91], we can derive the following asymptotic expression for the Whittaker function in the $\eta_0 \to +\infty$ limit (for which $\varepsilon_0 \to 0$)

$$W_{-\eta_0,\ell_0+\frac{1}{2}}(2k_0r) \simeq \left(\frac{\kappa_0 r}{2\eta_0}\right)^{1/4}\exp[\eta_0-\eta_0\ln(\eta_0)-2\sqrt{2\eta_0\kappa_0 r}]. \tag{2.40}$$

In the zero binding energy limit, the bound-state wave function in equation (4.1), becomes [91]

$$\phi_{\ell_0}^{j_0}(k_0,r) \overset{r\to\infty}{\to} C_{\ell_0 j_0}\left(\frac{\kappa_0 r}{2\eta_0^2}\right)^{1/4}\exp[\eta_0-\eta_0\ln(\eta_0)-2\sqrt{2\kappa_0 r}]. \tag{2.41}$$

From this equation, one can deduce that in the $\varepsilon_0 \to 0$ limit,

$$\int_0^\infty |\phi_{\ell_0}^{j_0}(k_0,r)|^2 dr < \infty, \tag{2.42}$$

which shows that in this limit, the proton-halo system for which $\eta_0 \neq 0$, has a square-integrable wave function, as also observed in Ref. [65], for the ^{7}Be+p proton-halo system. For a neutron-halo system where $\eta_0 = 0$, from equation (2.37), and following [91], in the zero binding energy limit one obtains the following expression for the bound-state wave function

$$\phi_{\ell_0}^{j_0}(k_0,r) \overset{r\to\infty}{\to} C_{\ell_0 j_0}\frac{(2\ell_0-1)!!}{(k_0 r)^{\ell_0}}, \tag{2.43}$$

where $C_{\ell_0 j_0} \propto k_0^{\ell_0}$ [91]. According to this proportionality, the wave function falls asymptotically as $\sim 1/r^{\ell_0}$. Therefore, the wave function also satisfies equation (2.42), depending on the value of ℓ_0. This emphasizes the crucial relevance of the orbital angular momentum ℓ_0 in the breakup of the neutron-rich systems in the $\varepsilon_0 \to 0$ limit. For an s-wave bound-state ($\ell_0 = 0$), the asymptotic behavior of the wave function in the zero binding energy limit is given by equation (2.38). In this case, $\lim\limits_{\varepsilon_0 \to 0} \phi_{\ell_0}^{j_0}(k_0, r) \to C_{\ell_0 j_0}$, such that the wave function does not satisfy equation (2.42).

2.1.5 Discretization of the two-body continuum space

Naturally, the scattering states of any quantum system are infinite, and the corresponding wave functions, as normalized according to equation (2.13), are indefinitely oscillating functions. This renders a theoretical investigation of transitions between two scattering states almost impossible, given the fact that the matrix elements that governs such transitions contain a radial integral that includes two scattering wave functions, leading to convergence issues. As we have mentioned elsewhere in this work, this problem is circumvented by the Continuum Discretized Couple Channel (CDCC) formalism [63]. Within this formalism, the scattering wave functions are transformed into bin wave functions, which are square integrable. In this case, the transition matrix elements between two scattering states will converge. In order to obtain the bin wave functions, the continuous linear momentum k by a maximum value k_{max} (subject to convergence requirements) and the $[0, k_{max}]$ interval discretized into N_b momentum bins spaced by $\Delta k_i = [k_i - k_{i-1}]\,(i = 1, 2, 3, ..., N_b)$. The bin wave function in each bin is defined as [92]

$$\varphi_\ell^j(k_i, r) = \sqrt{\frac{2}{\pi W_{\beta_i}}} \int_{k_i - 1}^{k_i} \mathrm{g}_{\beta_i}(k) \phi_\ell^j(k, r) dk, \tag{2.44}$$

where $\varphi_\ell^j(k_i, r)$ are square integrable bin wave function that can be normalized according to $(r \to \infty)$

$$\langle \varphi_{k_i \ell}^j(r) | \varphi_{k_i \ell}^j(r) \rangle = 1, \tag{2.45}$$

and W_{β_i} a normalization coefficient

$$W_{\beta_i} = \int_{k_i - 1}^{k_i} |\mathrm{g}_{\beta_i}(k)|^2 \, dk. \tag{2.46}$$

This equation (2.44), is associated with the bin energies

$$\varepsilon_{\beta_i} = \frac{\hbar^2}{2\mu_{cv} W_{\beta_i}^2} \int_{k_i - 1}^{k_i} k^2 \, |\mathrm{g}_{\beta_i}(k)|^2 \, dk, \tag{2.47}$$

where $\mathrm{g}_{\beta_i}(k)$ is the weight function that depend on the bin states with the subscript $\beta_i \equiv (i, \ell, s, j)$, whereas the ground state $\beta_0 \equiv (0, \ell_0, s, j_0)$. For the s-wave non-resonant bins is common to use $\mathrm{g}_{\beta_i}(k) = 1$ such that a normalization constant becomes

$$\begin{aligned} W_{\beta_i} &= \sqrt{\Delta k_i} \\ &= \sqrt{k_i - k_{i-1}}, \end{aligned} \tag{2.48}$$

where ε_{β_i} the bin energies correspond to

$$\varepsilon_{\beta_i} = \frac{\hbar^2 \hat{k}^2}{2\mu_{cv}}, \tag{2.49}$$

with

$$\hat{k}_i^2 = \frac{k_i^2 + k_i k_{i-1} + k_{i-1}^2}{3}. \tag{2.50}$$

On the other hand, the s-wave resonant bins, $g_i(k) = k$ such that

$$\begin{aligned} W_{\beta_i}^2 &= \int_{k_{i-1}}^{k_i} |k|^2 \, dk \\ &= \Delta k_i \hat{k}_{i-1}^2, \end{aligned} \tag{2.51}$$

where ε_{β_i} the bin energies are related to

$$\varepsilon_{\beta_i} = \frac{\hbar^2}{10\mu_{cv} W_{\beta_i}^2} \left(k_i^5 - k_{i-1}^5 \right). \tag{2.52}$$

In this case the resonant bins as in Refs. [12, 93–96], is give as

$$\mathrm{g}_{\beta_i}(k) = \left| \frac{\frac{i}{2}\Gamma}{\varepsilon_{\beta_i} - \varepsilon_r + \frac{i}{2}\Gamma} \right|, \tag{2.53}$$

where Γ is the resonance width, ε_{β_i} a continuum intrinsic energy and ε_r the resonant energy as mention earlier.

2.2 Three-body system

The three-body system we are considering in this section is described by the interaction of a two-body projectile "p" (which we have described in Section 2.1) with a target nucleus. It is represented by the diagram of figure 2.1, where the projectile fragments, the core "c" and valence nucleus "v" interact individually with the target nucleus "t", i.e., $p+t \to c+v+t$. In our description of the three-body system, we not take into account any explicit target excitations other than those stimulated by the different projectile-target interactions. In this diagram, $\boldsymbol{R}$, represents the relative projectile-target centre-of-mass coordinate, $\boldsymbol{R}_{ct}$, and $\boldsymbol{R}_{vt}$, the core-target and nucleon-target coordinates, and $\boldsymbol{r}$, the projectile internal coordinate, or the core-nucleon relative coordinate as indicated in Section 2.1. This diagram shows that the three-body system involves at least three different interactions, namely, the core-target potential $[U_{ct}(\boldsymbol{R}_{ct})]$, the nucleon-target interaction $[U_{vt}(\boldsymbol{R}_{vt})]$, and the core-nucleon interaction $[V_{cv}(\boldsymbol{r})]$, which we have already described in Section 2.1. The fragments-target coordinates $\boldsymbol{R}_{ct}$, and $\boldsymbol{R}_{vt}$, are defined in terms of the relative coordinates $\boldsymbol{R}$ and $\boldsymbol{r}$ as follows

$$\begin{aligned} \boldsymbol{R}_{ct} &= \boldsymbol{R} + \frac{m_v}{m_p}\boldsymbol{r} \\ \boldsymbol{R}_{vt} &= \boldsymbol{R} - \frac{m_c}{m_p}\boldsymbol{r}, \end{aligned} \tag{2.54}$$

where m_c, m_v and $m_p = m_c + m_v$ are the core, valence nucleon and projectile masses, respectively.

The three-body system is described by the three-body wave function $\Psi^{JM}_{\boldsymbol{K}_\gamma}(\boldsymbol{r}, \boldsymbol{R})$, that satisfies the following Schrödinger equation

$$(H_{3b} - E)\,\Psi^{JM}_{\boldsymbol{K}_\gamma}(\boldsymbol{r}, \boldsymbol{R}) = 0, \tag{2.55}$$

where H_{3b} is the three-body Hamiltonian of the system, for which $\Psi^{JM}_{\boldsymbol{K}_\gamma}(\boldsymbol{r}, \boldsymbol{R})$ is an eigenfunction [we will define the linear momentum $\boldsymbol{K}$ and the subscript γ in Section 2.2.1], J, is the total angular momentum with M its z-projection, E, is the total energy of the system. The Hamiltonian H_{3b} is written as

$$H_{3b} = T_R + H_p + U(\boldsymbol{r}, \boldsymbol{R}), \tag{2.56}$$

where T_R is the projectile-target kinetic energy operator, given by

$$T_R = -\frac{\hbar^2}{2\mu_{pt}} \nabla^2_{\boldsymbol{R}}, \tag{2.57}$$

with μ_{pt} the projectile-target reduced mass and the projectile Hamiltonian H_p, is given by equation (2.3). In equation (2.55, $U(\boldsymbol{r}, \boldsymbol{R})$ the projectile-target optical potential, which is a sum of the core-target $[U_{ct}(\boldsymbol{R}_{ct})]$and nucleon-target $[U_{vt}(\boldsymbol{R}_{vt})]$ optical potentials. That is

$$\begin{aligned} U(\boldsymbol{r}, \boldsymbol{R}) &= U_{ct}(\boldsymbol{R}_{ct}) + U_{vt}(\boldsymbol{R}_{vt}) \\ &= V_{ct}^{Coul}(\boldsymbol{R}_{ct}) + V_{ct}^{Nucl}(\boldsymbol{R}_{ct}) + V_{vt}^{Coul}(\boldsymbol{R}_{vt}) + V_{vt}^{Nucl}(\boldsymbol{R}_{vt}), \end{aligned} \tag{2.58}$$

where $V_x^{Coul}(\boldsymbol{R}_x)$ and $V_x^{Nucl}(\boldsymbol{R}_x)$, are Coulomb and nuclear components of the potential $U_x(\boldsymbol{R}_x)$, $(x \equiv ct, vt)$.

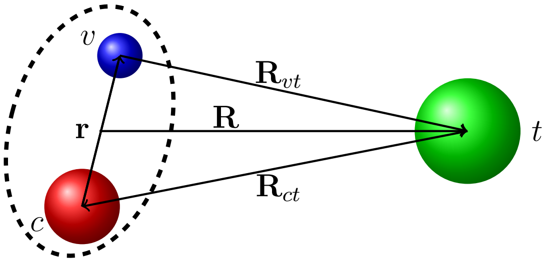

Figure 2.1: Three-body coordinate system for the collision between a two-body projectile and the target.

2.2.1 Construction of the three-body wave function

To construct the three-body wave function that describes the projectile-target motion before and after interaction, we need consider the fact that on the entrance channel, the projectile remains in the bound-state. After interaction, many scenario may take place. Among others, projectile may remain in the ground-state in the exit channel (elastic scattering) or it may get excited (inelastic scattering) or dissociate into its constituent fragments (breakup). The later case is the one we are interested with in this work. The wave function $\Psi^{JM}(\boldsymbol{r},\boldsymbol{R})$ then has two components, one which accounts for the elastic scattering (entrance channel) and the other one for the breakup (exit channel).

$$\Psi^{JM}_{\mathbf{K}_\gamma}(\boldsymbol{r},\boldsymbol{R}) = \sum_{\beta_0,L} \frac{\chi^{LJ}_{\beta_0}(R)}{R}\mathcal{Y}^{LJ}_{\beta_0}(\boldsymbol{r},\boldsymbol{\Omega_R}) + \sum_{\beta,L}\int \frac{\chi^{LJ}_{\beta}}{R}\mathcal{Y}^{LJ}_{\beta}(\boldsymbol{r},\boldsymbol{\Omega_R})dk, \tag{2.59}$$

where L, is the relative orbital angular momentum of the projectile-target relative motion, $\gamma \equiv (\beta_0,\beta)$, $\beta_0 = (\ell_0, s, j_0)$, and $\beta = (\ell, s, j)$, are sets of quantum numbers that describe the projectile bound and scattering states, respectively. The linear momentum $\boldsymbol{K}_\gamma$ corresponds to the linear momentum $\boldsymbol{K}_{\beta_0}$ in the entrance channel, and to the linear momentum $\boldsymbol{K}_\beta$, in the exit channel. The momentum $\boldsymbol{K}_\beta$ is associated with $\boldsymbol{K}_{\beta_0}$ through the following energy conservation principle

$$\frac{\hbar^2}{2\mu_{pt}}K^2_\beta + \varepsilon_\beta = \frac{\hbar^2}{2\mu_{pt}}K^2_{\beta_0} + \varepsilon_0. \tag{2.60}$$

In equation (2.59), the channel wave functions $\mathcal{Y}^{LJ}_{\beta_0}(\boldsymbol{r},\boldsymbol{\Omega_R})$ and $\mathcal{Y}^{LJ}_{\beta}(\boldsymbol{r},\boldsymbol{\Omega_R})$ are defined as

$$\begin{aligned}
\mathcal{Y}^{LJ}_{\beta_0}(\boldsymbol{r},\boldsymbol{\Omega_R}) &= i^L\left[\Phi^{m_j}_{\beta_0}(\boldsymbol{k},\boldsymbol{r})\otimes Y^{M_L}_L(\boldsymbol{\Omega_R})\right]_{JM}\\
\mathcal{Y}^{LJ}_{\beta}(\boldsymbol{r},\boldsymbol{\Omega_R}) &= i^L\left[\Phi^{m_j}_{\beta}(\boldsymbol{k},\boldsymbol{r})\otimes Y^{M_L}_L(\boldsymbol{\Omega_R})\right]_{JM},
\end{aligned} \tag{2.61}$$

where $Y^{M_L}_L(\Omega_{\boldsymbol{R}})$, is the spherical harmonics associated with the orbital angular momentum L, with M_L its z-projection, $\Omega_{\boldsymbol{R}} \equiv (\theta,\phi)$, is the solid angle in the direction of the coordinate $\boldsymbol{R}$, expressed in spherical coordinates, $\Phi^{m_j}_{\beta_0}(\boldsymbol{k},\boldsymbol{r})$, and $\Phi^{m_j}_{\beta}(\boldsymbol{k},\boldsymbol{r})$ corresponds to the projectile bound and scattering wave functions, given by equation (2.7). While the first term in equation (2.59) is finite, the second term is not, given the infinite number of scattering states. As we have indicated in Section 2.1.5, this problem is addressed by the CDCC formalism, where the scattering wave function is transformed into square-integrable bin wave function. In this case, equation (2.59), becomes

$$\Psi^{JM}_{\boldsymbol{K}_{\gamma_i}}(\boldsymbol{r},\boldsymbol{R}) = \sum_{\beta_0,L}\frac{\chi^{LJ}_{\beta_0}(R)}{R}\mathcal{Y}^{LJ}_{\beta_0}(\boldsymbol{r},\boldsymbol{\Omega_R}) + \sum_{\beta_i,L}\frac{\chi^{LJ}_{\beta_i}(R)}{R}\mathcal{Y}^{LJ}_{\beta_i}(\boldsymbol{r},\boldsymbol{\Omega_R}), \tag{2.62}$$

where $\gamma_i \equiv (\beta_0, \beta_i)$, and $\mathcal{Y}^{LJ}_{\beta_0}(\boldsymbol{r},\boldsymbol{\Omega_R})$ is given by

$$\mathcal{Y}^{LJ}_{\beta_i}(\boldsymbol{r},\boldsymbol{\Omega_R}) = i^L\left[\Phi^{m_j}_{\beta_i}(\boldsymbol{k}_i,\boldsymbol{r})\otimes Y^{M_L}_L(\boldsymbol{\Omega_R})\right]_{JM}, \tag{2.63}$$

with

$$\Phi^{m_j}_{\beta_i}(\boldsymbol{k}_i,\boldsymbol{r}) = \frac{\varphi^j_{\beta_i}(k_i,r)}{r}\Bigg[Y^{m_\ell}_\ell(\boldsymbol{\Omega_r})\otimes X_s\Bigg]_{jm_j}. \tag{2.64}$$

2.2.2 Coupled differential equations

The substitution of the expansion (2.59) into the Schrödinger equation (2.55), results in the following set of coupled differential equations for the coefficients $\chi^{LJ}_{\gamma_i}(R)$ given by

$$\begin{aligned}\left(-\frac{\hbar^2}{2\mu_{pt}}\frac{d^2}{dR^2} - \frac{L(L+1)}{R^2} + V^{LJ}_{\gamma_i\gamma_i}(R) + \varepsilon_{\gamma_i} - E\right)\chi^{LJ}_{\gamma_i}(R)&\\ - \sum_{\gamma_i\neq\gamma_i'} V^{LL'J}_{\gamma_i\gamma_i'}(R)\chi^{L'J}_{\gamma_i'}(R) = 0,&\end{aligned} \tag{2.65}$$

where $\varepsilon_{\gamma_i} \equiv (\varepsilon_0, \varepsilon_{\beta_i})$ [$\varepsilon_0 < 0$, is the ground-state binding energy, and ε_{β_i} are bin energies defined by equation (2.47)], and $V^{LL'J}_{\gamma_i\gamma_i'}(R)$, are off-diagonal coupling potential matrix elements, couplings different γ_i and γ_i' states. They are defined by

$$\begin{aligned} V^{LL'J}_{\gamma_i\gamma_i'}(R) &= V_{\beta_0\gamma}(R) + V_{\gamma_i\gamma_i'}(R) \\ &= \left\langle\mathcal{Y}^{LJ}_{\beta_0}(\boldsymbol{r},\boldsymbol{\Omega_R})\left|U_{pt}(\boldsymbol{r},\boldsymbol{R})\right|\mathcal{Y}^{LJ}_{\beta_i}(\boldsymbol{r},\boldsymbol{\Omega_R})\right\rangle \\ &+ \left\langle\mathcal{Y}^{LJ}_{\beta_i}(\boldsymbol{r},\boldsymbol{\Omega_R})\left|U_{pt}(\boldsymbol{r},\boldsymbol{R})\right|\mathcal{Y}^{L'J}_{\beta_i'}(\boldsymbol{r},\boldsymbol{\Omega_R})\right\rangle, \end{aligned} \tag{2.66}$$

where the channel wave functions are given by equation (2.61), the potential $U_{pt}(\boldsymbol{r},\boldsymbol{R})$, by equation (2.58). The first term in this equation represents couplings to and from the bound-state, whereas the second stands for the couplings among continuum states (continuum-continuum couplings). On the left-hand side of equation (2.65), $V^{LJ}_{\gamma\gamma}(R)$, represents the diagonal couplings, and reads

$$V_{\gamma_i\gamma_i}(R) = V^{LJ}_{\beta_0\beta_0}(R) + V^{LJ}_{\beta_i\beta_i}(R). \tag{2.67}$$

In this equation, $V^{LJ}_{\beta_0\beta_0}(R)$, represents the matrix elements in the elastic scattering channel. In most cases, it only contains the diagonal monopole Coulomb interaction between the projectile and the target, $Z_pZ_te^2/R$, where Z_pe, and Z_te are respectively the projectile and target charges. Although this potential is most valid in the asymptotic region, where $R \gg r$, such that $R_{ct} \simeq R_{vt} \simeq R$, in which case the projectile can be regarded as a tightly-bound system, in the inner region, where $R \simeq r$, it disregards the two-body nature of the projectile and hence its crucial halo properties in the breakup process. One of the ways to correct this potential in the inner region, is to consider a potential that is obtained by folding the interactions between the fragments and the target, with the square of the ground-state projectile wave function, i.e.,

$$\widetilde{V}_{\beta_0\beta_0}(R) = \int d^3\boldsymbol{r}|\Phi^{m_j}_{\beta_0}(\boldsymbol{k}_b, \boldsymbol{r})|^2 U_{pt}(\boldsymbol{r}, \boldsymbol{R}), \tag{2.68}$$

where $|\Phi^{m_j}_{\beta_0}(\boldsymbol{k}_b, \boldsymbol{r})|^2$, represents the projectile ground-state density, and hence $\widetilde{V}_{\beta_0\beta_0}(R)$ contains the long-range behavior of the ground-state wave function. However, we leave the practical aspect of this potential to future investigations.

2.2.3 Analytical evaluation of the coupling matrix elements

In order to numerically solve the coupled differential equations (2.65), one needs to first couple the different angular momenta. To this end, as a first step, the potential $U_{pt}(\boldsymbol{r}, \boldsymbol{R})$ is expanded into multipoles as follows

$$U_{pt}(\boldsymbol{r}, \boldsymbol{R}) = \sum_{\lambda=0}^{\lambda_{max}} V_\lambda(r, R) P_\lambda(\cos\theta), \tag{2.69}$$

where $V_\lambda(r, R)$ are potential multipoles of multipole order λ (λ_{max}, being the maximum expansion order which is selected based on the convergence requirements), and $P_\lambda(\cos\theta)$, are Legendre polynomials, with θ the angle between the $\boldsymbol{r}$ and $\boldsymbol{R}$ vectors. The potential multipoles are then calculated as

$$V_\lambda(r,R) = \frac{2\lambda+1}{2}\int_{-1}^{1} U_{pt}(\boldsymbol{r},\boldsymbol{R}) P_\lambda(z)dz, \tag{2.70}$$

with $z = \cos\theta$. Legendre polynomials are expressed in terms of spherical harmonics as follows

$$\begin{aligned} P_\lambda(\cos\theta) &= \frac{4\pi}{2\lambda+1}\sum_{\alpha=-\lambda}^{\lambda} Y_\lambda^{\alpha}(\Omega_R)\cdot Y_\lambda^{\alpha *}(\Omega_r) \\ &= \frac{4\pi}{2\lambda+1} Y_\lambda(\Omega_R)\cdot Y_\lambda(\Omega_r). \end{aligned} \tag{2.71}$$

With this equation, the potential (2.69), becomes

$$U_{pt}(\boldsymbol{r},\boldsymbol{R}) = \frac{4\pi}{2\lambda+1}\sum_{\lambda=0}^{\lambda_{max}} V_\lambda(r,R) Y_\lambda(\Omega_R) Y_\lambda(\Omega_r). \tag{2.72}$$

The substitution of this expansion into the coupling matrix elements (2.66), gives (considering only the off-diagonal part)

$$V_{\beta_i\beta_{i'}}^{LL'J}(R) = \sum_{\lambda=0}^{\infty}\frac{4\pi}{2\lambda+1}\left\langle \mathcal{Y}_{\beta_i}^{LJ}(\boldsymbol{r},\boldsymbol{\Omega_R})\middle| Y_\lambda(\Omega_R)Y_\lambda(\Omega_r)V_\lambda(r,R)\middle| \mathcal{Y}_{\beta_i'}^{L'J}(\boldsymbol{r},\boldsymbol{\Omega_R})\right\rangle. \tag{2.73}$$

With the channel wave function $\mathcal{Y}_{\beta_i}^{LJ}(\boldsymbol{r},\boldsymbol{\Omega_R})$, is given by equation (2.63), and applying the Wigner-Eckart theorem [97–99], we obtain

$$\begin{aligned} V_{\beta_i\beta_{i'}}^{LL'J}(R) &= \sum_{\lambda=0}^{\lambda_{max}} (-1)^{j'+L+J}\sqrt{\frac{4\pi}{\hat{\lambda}}}\left\langle L\| Y_\lambda(\Omega_R)\| L'\right\rangle \begin{Bmatrix} J & L & j \\ \lambda & j' & L' \end{Bmatrix} \\ &\times \left\langle \Phi_{\beta_i}^{m_j}(\boldsymbol{r})\| Y_\lambda(\Omega_r)V_\lambda(r,R)\|\Phi_{\beta_i'}^{m_{j'}}(\boldsymbol{r})\right\rangle, \end{aligned} \tag{2.74}$$

where $\begin{Bmatrix} J & L & j \\ \lambda & j' & L' \end{Bmatrix}$ is the Wigner 6j coefficients,

$$\left\langle L \| Y_\lambda(\Omega_R) \| L' \right\rangle = (-1)^L \sqrt{\frac{\hat{L}\hat{\lambda}\hat{L}}{4\pi}} \begin{pmatrix} L & \lambda & L' \\ 0 & 0 & 0 \end{pmatrix}, \tag{2.75}$$

and

$$\left\langle \Phi_{\beta_i}^{m_j}(\boldsymbol{r}) \| Y_\lambda(\Omega_r) V_\lambda(r,R) \| \Phi_{\beta_i'}^{m_{j'}}(\boldsymbol{r}) \right\rangle = (-1)^{\ell'+s+j} \left\langle \ell \| Y_\lambda(\Omega_r) \| \ell' \right\rangle \begin{Bmatrix} s & \ell & j \\ \lambda & j' & \ell' \end{Bmatrix} \mathcal{I}_{\beta_i \beta_{i'}}^{\lambda}(R) \tag{2.76}$$

with

$$\left\langle \ell \| Y_\lambda(\Omega_r) \| \ell' \right\rangle = (-1)^\ell \sqrt{\frac{\hat{\ell}\hat{\lambda}\hat{\ell}}{4\pi}} \begin{pmatrix} \ell & \lambda & \ell' \\ 0 & 0 & 0 \end{pmatrix}, \tag{2.77}$$

where $\hat{x} = 2x+1$. In equation (2.76), $\mathcal{I}_{\beta_i \beta_{i'}}^{\lambda}(R)$ is the radial integral that is to be evaluated numerically, and it is given by

$$\begin{aligned} \mathcal{I}_{\beta_i \beta_{i'}}^{\lambda}(R) &= \left\langle \varphi_{\beta_i}^{j}(k_i, r) \left| V_\lambda(r,R) \right| \varphi_{\beta_{i'}}^{j'}(k_{i'}, r) \right\rangle \\ &= \int_0^\infty dr \varphi_{\beta_i}^{j*}(k_i, r) V_\lambda(r,R) \varphi_{\beta_{i'}}^{j'}(k_{i'}, r). \end{aligned} \tag{2.78}$$

This radial integral contains the most important information regarding the couplings among various bin states. Notice that, because the bin wave functions are square integrable, this integral converges without any issues. For couplings to and from the ground-state, the bin wave function $\varphi_{\beta_i}^{j*}(k_i, r)$, is replaced by the ground-state wave function $\phi_{\ell_0}^{j_0}(k_0, r)$, i.e.,

$$\mathcal{I}_{\beta_0 \beta_{i'}}^{\lambda}(R) = \int_0^\infty dr \phi_{\ell_0}^{j_0}(k_0, r) V_\lambda(r,R) \varphi_{\beta_{i'}}^{j'}(k_{i'}, r). \tag{2.79}$$

In this case, the radial integral convergence even faster, given the natural boundary conditions of the ground-state wave function in the asymptotic region. For the elastic scattering where the projectile remains the its ground-state on both incoming and outgoing trajectories, the radial integral becomes

$$\mathcal{I}^{\lambda}_{\beta_0\beta_0}(R) = \int_0^{\infty} dr|\phi^{j_0}_{\ell_0}(k_0, r)|^2 V_\lambda(r, R). \tag{2.80}$$

In the zero binding energy limit, where the tail of the ground-state wave function extends to infinity, we expect the radial integral in equations (2.78), and (2.79) to converge. This is due to the square integrability of the bin wave function, such that the integrand of this integral will collapse to zero in the asymptotic region, despite the fact that the ground-state wave function becomes unbound. Therefore, one can expect converged breakup observables of a projectile with binding energy in the zero limit. However, the radial integral in equation (2.80), will fail to converge in the zero binding energy limit.

2.2.4 Coupling matrix of pure Coulomb interactions

As we have shown in equation (2.58), the potential $U_{pt}(\boldsymbol{r}, \boldsymbol{R})$, contains both Coulomb and nuclear interactions. Due to the short-range nature of nuclear forces, because they vanish for $R \geq R_n = r_0(A_p^{1/3} + A_t^{1/3})$, in the asymptotic region, only Coulomb interaction is available to due the long-range nature of Coulomb forces. In this region, this potential $U_{pt}(\boldsymbol{r}, \boldsymbol{R})$, reduces to Coulomb components in the asymptotic region.

$$V^{Coul}_{pt}(\boldsymbol{r}, \boldsymbol{R}) \overset{R\to\infty}{\to} 4\pi Z_t e \sum_{\lambda=0}^{\lambda_{max}} \frac{\sqrt{2\lambda+1}}{R^{\lambda+1}} \left[\mathcal{M}^{\varepsilon}_{\lambda}(\boldsymbol{r}) \otimes Y^{M_L}_{L}(\Omega_R)\right]_{\lambda_0}, \tag{2.81}$$

where $Z_t e$ is the target charge and

$$\mathcal{M}^{\varepsilon}_{\lambda}(\boldsymbol{r}) = Z_\lambda r^\lambda Y^{\nu}_{\lambda}(\Omega_r), \tag{2.82}$$

is the projectile electric operator with Z_λ the effective charge

$$Z_\lambda = e\left[Z_v\left(\frac{m_c}{m_p}\right)^{\lambda} + Z_c\left(-\frac{m_v}{m_p}\right)^{\lambda}\right]. \tag{2.83}$$

Following the same procedure in Section 2.2.3, together with the Coulomb excitation theory [100], the Coulomb coupling matrix elements are given by

$$\begin{aligned} V^{Coul}_{\beta_i,\beta'_i}(R) &= Z_t e(-1)^{\ell+L}\sum_{\lambda=0}^{\lambda_{max}}\sqrt{\frac{\hat{\ell}\hat{\ell}'\hat{L}\hat{L}'\hat{\lambda}'}{4\pi}}(-1)^{\lambda+s+\ell'+j'+j+L+J} \qquad (2.84)\\ &\times \begin{pmatrix} L & \lambda & L' \\ 0 & 0 & 0 \end{pmatrix}\begin{Bmatrix} J & L & j \\ \lambda & j' & L' \end{Bmatrix}\Big\langle \Phi_{\beta_i}(\boldsymbol{k}_i,\boldsymbol{r})\|(M^{\varepsilon}_{\lambda}(\boldsymbol{r}))\|\Phi_{\beta_{i'}}(\boldsymbol{k}_{i'},\boldsymbol{r})\Big\rangle \mathcal{I}_{\beta_i\beta_{i'}}(R), \end{aligned}$$

with the radial integral is given by

$$\mathcal{I}_{\beta_i\beta_{i'}}(R) = \int_{R_n+\delta R}^{\infty} F_L(K_{\beta_i R})\frac{1}{R^{\lambda+1}}F_{L'}(K_{\beta_{i'}R})dR, \qquad (2.85)$$

where $F_L(K_{\beta_i R})$, are Coulomb functions [89]. The function δR is introduced to ensure that nuclear forces are restricted to $R \leq R_n + \delta R$. Many interesting properties of the projectile can be obtained from the integral $\langle \Phi_{\beta_i}(\boldsymbol{k}_i,\boldsymbol{r})\|(M^{\varepsilon}_{\lambda}(\boldsymbol{r}))\|\Phi_{\beta_{i'}}(\boldsymbol{k}_{i'},\boldsymbol{r})\rangle$. For example, the projectile reduced transition probabilities $B(E\lambda)$ from β_i states to $\beta_{i'}$ states are given by

$$\begin{aligned} B(E\lambda : \beta_i \to \beta'_i) &= \frac{2j'+1}{2j+1}\Big| \langle \Phi_{\beta_i}(\boldsymbol{k}_i,\boldsymbol{r})\|(M^{\varepsilon}_{\lambda}(\boldsymbol{r}))\|\Phi_{\beta_{i'}}(\boldsymbol{k}_{i'},\boldsymbol{r})\rangle \Big|^2 \\ &= \frac{2j'+1}{2j+1}\Big|\frac{Z_\lambda}{4\pi}(-1)^{s+\ell+j+\lambda+\ell'}\sqrt{\hat{\ell}\hat{j}\hat{\lambda}\hat{\ell}'} \qquad (2.86)\\ &\times \begin{pmatrix} \ell & \lambda & \ell' \\ 0 & 0 & 0 \end{pmatrix}\begin{Bmatrix} s & \ell & j \\ \lambda & j' & \ell' \end{Bmatrix}\int_0^{\infty}\varphi^{j*}_{\beta_i}(k_i,r)^{\lambda}\varphi^{j'}_{\beta_i}(k_{i'},r)dr\Big|^2. \end{aligned}$$

The reduced probabilities for transitions to and from the ground-state are obtained by replacing the bin wave function $\varphi^{j*}_{\beta_i}(k_i,r)$ with the ground-state wave function.

2.2.5 Breakup cross sections

After the coupling matrix elements have been numerically evaluated, the coupled differential equations (2.65) can be solved with the usual asymptotical boundary conditions

$(R \to \infty)$

$$\chi^{LJ}_{\beta_i}(R) \overset{R\to\infty}{\to} \frac{i}{2}\left[H^-_{\beta_i}(K_{\beta_i}R)\delta_{\beta_i\beta'_i} - H^+_{\beta_i}(K_{\beta_i}R)S^J_{\beta_i\beta_{i'}}(K_{\beta'_i})\right], \tag{2.87}$$

where $H^{\pm}_{\beta_i}(K_{\beta_i})$ are the Coulomb-Hankel functions [89], and $S^J_{\beta_i\beta_{i'}}(K_{\beta_i})$ is the breakup S-matrix elements.

The breakup observables can be directly obtained from the breakup S-matrix. The inelastic scattering amplitudes for populating each bin state (β'_i) from the initial state (β_i), is related to the breakup S-matrix through the following expression [92, 101]

$$\begin{aligned} F^{m'_j}_{m_j}(\Omega) &= \frac{\sqrt{\pi}}{iK_{\beta_0}}\sqrt{\frac{K_{\beta'_i}}{K_{\beta_0}}}\sum_{LL'}\sum_{J}\sqrt{2L+1}\langle LM_L j m_j|JM\rangle\langle L'M_{L'}j'm_{j'}|JM\rangle \\ &= \times e^{i(\sigma_L+\sigma_{L'})}S^J_{\beta_i\beta_{i'}}(K_{\beta'_i})Y^{M_{L'}}_{L'}(\Omega), \end{aligned} \tag{2.88}$$

where $\Omega \equiv \Omega_{\boldsymbol{R}}$, σ_L, and $\sigma_{L'}$ are Coulomb phase shifts, given by

$$\sigma_L = \arg\Gamma(1 + L + i\eta), \tag{2.89}$$

with $\eta = \dfrac{\mu_{pt}}{\hbar^2}\dfrac{Z_pZ_te^2}{K_{\beta_0}}$. In order to obtain the different breakup observables, such as the angular and energy distributions breakup cross sections of the projectile fragments, we need to calculate the corresponding transition matrix elements. For projectile and projectile-target final state momenta $\boldsymbol{k}$ and $\boldsymbol{K}$, the transition matrix elements are given by [102, 103]

$$T^{m_j}_{\nu}(\boldsymbol{k},\boldsymbol{K}) = \langle\psi^{(+)}_{\boldsymbol{k}m_\ell\nu}(\boldsymbol{k},\boldsymbol{r})e^{i\boldsymbol{K}\cdot\boldsymbol{R}}|U(\boldsymbol{r},\boldsymbol{R})|\Psi^{JM}_{\boldsymbol{K}}(\boldsymbol{r},\boldsymbol{R})\rangle, \tag{2.90}$$

where $\psi^{(+)}_{\boldsymbol{k}m_\ell\nu}(\boldsymbol{k},\boldsymbol{r})$ is the scattering wave function in projectile final state, given by equation (2.21), $e^{i\boldsymbol{K}\cdot\boldsymbol{R}}$, the plane wave that describes the final state of the projectile-target motion, and $\Psi^{JM}_{\boldsymbol{K}}(\boldsymbol{r},\boldsymbol{R})$ is the original projectile-target wave function. To evaluate these transitions matrix elements is a formidable task given the fact that they contain pure scattering wave functions. In order to address this problem, we replace the original projectile-target wave function by its CDCC approximated wave function $\Psi^{JM}_{\boldsymbol{K}_{\beta_i}}(\boldsymbol{r},\boldsymbol{R})$, and insert the square-integrable bin wave functions $\Phi^{m_j}_{\beta_i}(\boldsymbol{k}_i, r)$ in the bra and ket of equation (2.90), to obtain [92,101],

$$\mathcal{T}^{m_j}_{m_\ell\nu}(\boldsymbol{k},\boldsymbol{K}_{\beta_i}) = \sum_{\beta_i}\sum_{m_j}\left\langle \psi^{(-)}_{\boldsymbol{k}m_\ell\nu}(\boldsymbol{k},\boldsymbol{r})|\Phi^{m_j}_{\beta_i}(\boldsymbol{k}_i,r)\right\rangle T^{\beta_i}_{\nu m_j}(\boldsymbol{K}_{\beta_i}), \tag{2.91}$$

where the projectile final state wave function $\psi^{(-)}_{\boldsymbol{k}m_\ell\nu}(\boldsymbol{k},\boldsymbol{r})$ is obtained by applying the time-reversal operator [89] on the wave function $\psi^{(+)}_{\boldsymbol{k}m_\ell\nu}(\boldsymbol{k},\boldsymbol{r})$, and

$$T^{\beta_i}_{\nu m_j}(\boldsymbol{K}_{\beta_i}) = \left\langle \Phi^{m_j}_{\beta_i}(\boldsymbol{r})e^{i\boldsymbol{K}_{\beta_i}\cdot\boldsymbol{R}}|U(\boldsymbol{r},\boldsymbol{R})|\Psi^{JM}_{\boldsymbol{K}_{\beta_i}}(\boldsymbol{r},\boldsymbol{R})\right\rangle, \tag{2.92}$$

and $\langle\psi^{(-)}_{\boldsymbol{k}m_\ell\nu}(\boldsymbol{k},\boldsymbol{r})|\Phi^{m_j}_{\beta_i}(\boldsymbol{k}_i,\boldsymbol{r})\rangle$ the smoothing factor [12,102,103], is given by

$$\begin{aligned}\langle\psi^{(-)}_{\boldsymbol{k}m_\ell\nu}(\boldsymbol{k},\boldsymbol{r})|\Phi^{m_j}_{\beta_i}(\boldsymbol{k}_i,\boldsymbol{r})\rangle &= \frac{4\pi}{k}\sum_{\beta}(-i)^{\ell}e^{i\left[\sigma_\ell(k)+\delta_{\ell j}(k)\right]}\sum_{\nu}\langle \ell m_\ell s\nu|jm_j\rangle \\ &\times\ Y^{m_\ell}_{\ell}(\Omega_k)\int\Phi^{m_j\star}_{\beta}(\boldsymbol{k},\boldsymbol{r})\Phi^{m_j}_{\beta_i}(\boldsymbol{k}_i,\boldsymbol{r})d^3\boldsymbol{r}. \end{aligned}\tag{2.93}$$

Applying the spherical harmonics as well as the orthogonality of the Clebsh-Gordon coefficients, the radial integral is given by

$$\begin{aligned}\int\Phi^{m_j\star}_{\beta}(\boldsymbol{k},\boldsymbol{r})\Phi^{m_j}_{\beta_i}(\boldsymbol{k}_i,\boldsymbol{r})d^3\boldsymbol{r} &= \sqrt{\frac{2}{\pi W_{\beta_i}}}\int\phi^{j\star}_{\ell}(k,r)\int_{k_{i-1}}^{k_i}dk\mathrm{g}_{\beta_i}(k)\phi^{j}_{\ell}(k,r) \\ &= \sqrt{\frac{2}{\pi W_{\beta_i}}}\mathrm{g}_{\beta_i}(k)\quad if\quad k\in[k_{i-1},k_i]. \end{aligned}\tag{2.94}$$

This integral vanishes if $k\notin[k_{i-1},k_i]$. Then, smoothing factor becomes

$$\langle\psi^{(-)}_{\boldsymbol{k}m_\ell\nu}(\boldsymbol{k},\boldsymbol{r})|\Phi^{m_j}_{\beta_i}(\boldsymbol{k}_i,\boldsymbol{r})\rangle = \frac{4\pi}{k}\sum_{\beta}(-i)^{\ell}\alpha(k)\sum_{\nu}\langle \ell m_\ell s\nu|jm_j\rangle\, Y^{m_\ell}_{\ell}(\Omega_k) \tag{2.95}$$

where

$$\alpha(k) = e^{i\left[\sigma_\ell(k)+\delta_{\ell j}(k)\right]}\sqrt{\frac{2}{\pi W_{\beta_i}}}\int_{k_{i-1}}^{k_i}dk\mathrm{g}_{\beta_i}(k). \tag{2.96}$$

Since the breakup process can be generally regarded as an inelastic excitation of the projectile, the transition matrix elements $T^{\beta_i}_{\nu m_j}(\boldsymbol{K}_{\beta_i})$ can be related to the inelastic scattering amplitude $F^{m_{j'}}_{m_j}(\Omega)$, as follows [92]

$$T^{\beta_i}_{\nu m_j}(\boldsymbol{K}_{\beta_i}) = -\frac{2\pi\hbar^2}{\mu_{pt}}\sqrt{\frac{K_{\beta_0}}{K_{\beta'_i}}}F^{m_{j'}}_{m_j}(\Omega). \tag{2.97}$$

The breakup transition matrix elements then become

$$\begin{aligned}\mathcal{T}^{m_j}_{m_\ell\nu}(\boldsymbol{k},\boldsymbol{K}_{\beta_i}) &= -\frac{8\pi^{5/2}\hbar^2}{\mu_{pt}}\frac{1}{ikK_{\beta_0}}\sum_{\beta_i}\sum_{m_j}\sum_{\beta_i}(-i)^\ell\alpha(k)\sum_{\nu}\langle\ell m_\ell s\nu|jm_j\rangle\, Y^{m_\ell}_\ell(\Omega_k)\\ &\times \sum_{LL'}\sum_{J}\sqrt{2L+1}\langle LM_Ljm_j|JM\rangle\langle L'M_{L'}j'm_{j'}|JM\rangle\\ &\times e^{i(\sigma_L+\sigma_{L'})}S^J_{\beta_i\beta_{i'}}(K_{\beta'_i})Y^{M_{L'}}_{L'}(\Omega).\end{aligned} \tag{2.98}$$

After the breakup transition matrix elements are constructed, the differential breakup cross sections can be obtained following for example [92, 104]

$$\frac{d^3\sigma}{d\Omega_{\boldsymbol{k}}d\Omega d\varepsilon_{\beta_i}} = \frac{\mu_{cv}\mu^2_{pt}kK_{\beta_i}}{(2\pi)^5\hbar^6K_{\beta_0}}\frac{1}{2j+1}\sum_{\nu}\sum_{m_j}\left|\mathcal{T}^{m_j}_{m_\ell\nu}(\boldsymbol{k},\boldsymbol{K}_{\beta_i})\right|^2. \tag{2.99}$$

Integrating over the angle $\Omega_{\boldsymbol{k}}$, and substituting equation (2.98) into equation (2.99), one obtains the following double-differential breakup cross section

$$\begin{aligned}\frac{d^2\sigma}{d\Omega d\varepsilon_{\beta_i}} &= \int\frac{d^3\sigma}{d\Omega_{\boldsymbol{k}}d\Omega d\varepsilon_{\beta_i}}d\Omega_{\boldsymbol{k}}\\ &= \frac{\mu_{cv}}{\hbar^2k}\frac{1}{4\pi^{5/2}}\frac{K_{\beta_i}}{K^3_{\beta_0}}\frac{1}{2j+1}\sum_{\nu m_j}\sum_{\ell jm_j}\sum_{\ell'j'm'_j}\langle\ell m_\ell s\nu|jm_j\rangle\langle\ell'm'_\ell s\nu|j'm'_j\rangle\\ &\times \int d\Omega_{\boldsymbol{k}}Y^{m_\ell\star}_\ell(\Omega_{\boldsymbol{k}})Y^{m_{\ell'}}_{\ell'}(\Omega_{\boldsymbol{k}})\left|\sum_{i'}\alpha(k)\sqrt{\frac{K_{\beta'_i}}{K_{\beta_i}}}\sum_{LL'}\sum_{J}\sqrt{2L+1}\right.\\ &\times \left.\langle LM_Ljm_j|JM\rangle\langle L'M'_Lj'm'_j|JM\rangle e^{i(\sigma_L+\sigma_{L'})}S_{\beta_i\beta'_i}(K_{\beta'_i})Y^{M_{L'}}_{L'}(\Omega)\right|^2.\end{aligned} \tag{2.100}$$

Applying the properties of Clebsh-Goden and spherical harmonics, the expression above reduces to

$$\begin{aligned}
\frac{d^2\sigma}{d\Omega d\varepsilon_{\beta_i}} &= \int \frac{d^3\sigma}{d\Omega_{\boldsymbol{k}} d\Omega d\varepsilon_{\beta_i}} d\Omega_{\boldsymbol{k}} \\
&= \frac{\mu_{cv}}{\hbar^2 k}\frac{1}{4\pi^{5/2}}\frac{K_{\beta_i}}{K^3_{\beta_0}}\frac{1}{2j+1}\sum_{\ell j}\left|\sum_{i'}\alpha(k)\sqrt{\frac{K_{\beta'_i}}{K_{\beta_i}}}\sum_{LL'}\sum_{J}\sqrt{2L+1}\right. \qquad (2.101)\\
&\times \left.\langle LM_L j m_j|JM\rangle\langle L'M'_L j'm'_j|JM\rangle e^{i(\sigma_L+\sigma_{L'})} S_{\beta_i\beta'_i}(K_{\beta'_i}) Y_{L'}^{M_{L'}}(\Omega)\right|^2 .
\end{aligned}$$

Integrating the double-differential breakup cross sections, the angular and energy distributions breakup cross sections become

$$\begin{aligned}
\frac{d\sigma}{d\Omega} &= \int d\varepsilon \frac{d^2\sigma}{d\Omega d\varepsilon} \\
\frac{d\sigma}{d\varepsilon} &= \int d\varepsilon \frac{d^2\sigma}{d\Omega d\varepsilon}, \qquad (2.102)
\end{aligned}$$

$\varepsilon \equiv \varepsilon_{\beta_i}$.

2.2.6 First-order approximation theory

The first-order approximation theory [54, 55, 105, 106], is a straightforward theory that directly links the breakup cross section to the projectile internal structure. Although approximate, in many cases, it provides a satisfactory description of the experimental data (see for example Refs. [31, 107–109]). Following Refs. [54, 55, 105, 106], the first-order breakup probability defined as

$$\frac{dP^{E1}(\varepsilon, b)}{d\varepsilon} = \frac{16\pi}{9}\left(\frac{Z_t e^2}{\hbar v}\right)^2\left(\frac{z}{b}\right)^2[\mathcal{K}_0^2(z) + \mathcal{K}_1^2(z)]\frac{dB(E1)}{d\varepsilon}, \qquad (2.103)$$

where v is the projectile velocity $v = \sqrt{\frac{2E}{\mu_{pt}}}$, $\mathcal{K}_{0(1)}(z)$ are the second kind modified Bessel functions of order 0(1) [89], v, the projectile relative velocity, $\frac{dB(E1)}{d\varepsilon}$, the dipole electric response function and z, related to the minimum impact parameter b, as

$$z = \frac{\varepsilon - \varepsilon_0}{\hbar v} b. \qquad (2.104)$$

The dipole electric response function for the transition to and from the ground-state is given by

$$\frac{dB(E1)}{d\varepsilon} = \frac{\mu_{cv}}{\hbar^2 k} \sum_j (2j+1)|G_{\beta_0\beta}(r)|^2, \tag{2.105}$$

where $G_{\beta_0\beta}(r)$ is given by

$$G_{\beta_0\beta}(r) = eZ_\lambda(-1)^{\ell_0+\ell+j+s+\lambda} \begin{pmatrix} \ell_0 & \lambda & \ell \\ 0 & 0 & 0 \end{pmatrix} \begin{Bmatrix} s & \ell_0 & j_0 \\ \lambda & j' & \ell \end{Bmatrix} \int_0^\infty \varphi_{\ell_b}^{j_0}(k_0 r)^\lambda \varphi_\ell^j(k,r)dr, \tag{2.106}$$

where the effective charge Z_λ is given by equation (2.83).

In terms of the first-order breakup probability, the first-order Coulomb breakup cross section is given by

$$\frac{d\sigma_C^{E1}}{d\varepsilon} = 2\pi \int_{b_{min}}^\infty \frac{dP^{E1}(\varepsilon,b)}{d\varepsilon} bdb, \tag{2.107}$$

where the minimum impact parameter b_{min} is given by

$$b_{min} = \frac{\varepsilon-\varepsilon_0}{\hbar v}\left[\frac{Z_p Z_t e^2}{2E\tan(\theta_c/2)}\right], \tag{2.108}$$

with θ_c is the maximum cutoff scattering angle up to which the Coulomb breakup is dominant, ε and ε_b, are projectile excitation and binding energies, respectively. Know that [110],

$$\int z\mathcal{K}_n(z)dz = \frac{1}{2}z^2[\mathcal{K}_n(z) - \mathcal{K}_{n-1}\mathcal{K}_{n+1}], \tag{2.109}$$

and using the recurrence relation [110], the first-order Coulomb breakup cross section reduces to

$$\frac{d\sigma_C^{E1}}{d\varepsilon} = \frac{32\pi^2}{9}\left(\frac{Z_t e}{\hbar v}\right)^2 z_m \mathcal{K}_0(z_m)\mathcal{K}_1(z_m)\frac{dB(E1)}{d\varepsilon}. \tag{2.110}$$

2.3 Fusion reaction mechanism

In terms of the fusion reaction mechanism, the summation of both complete and incomplete fusion cross sections can lead to the total fusion cross section. The total fusion cross sections are evaluated as

$$\begin{aligned}\sigma_{TF} &= \frac{\pi}{k^2}\sum_J (2J+1)\left(1-\left|S^J_{\beta\beta'_i}\right|^2\right) \\ &= \frac{\pi}{k^2}\sum_J (2J+1)\,P_J, \qquad (2.111)\end{aligned}$$

where $P_J = 1-\left|S^J_{\beta\beta'_i}\right|^2$ represents the tunneling probability. The complete fusion cross section can be written as

$$\sigma_{CF} = \frac{\pi}{k^2}\sum_i (2J+1)\,T_{Ji}P_{Ji}, \qquad (2.112)$$

where T_{Ji} and P_{Ji} are the fusion transmission coefficient and the breakup survival probability, respectively.

To summarize, the two-body, three-body and fusion reactions have been discussed in more details in this chapter. The CDCC method has also been described in detail and will be used throughout this study. In the next chapter, this method is used to determine the breakup cross section as well as the complete cross section owing to the continuum-continuum couplings effect at deep sub-barrier, around, and above the Coulomb barrier incident energies.

Chapter 3

Deep sub-barrier breakup dynamics of the $^{8}\mathrm{B} + {}^{208}\mathrm{Pb}$ reaction

In this chapter we present the results of our investigation of the deep sub-barrier breakup dynamics for the $^{8}\mathrm{B} + {}^{208}\mathrm{Pb}$ reaction practical. The effects of these continuum-continuum couplings on the breakup cross section at the incident energies are analyzed. This will provide a better understanding of the predominance of the breakup channel at deep sub-barrier energies. The comparison of the total fusion, breakup, and total reaction cross sections are reported in this study. The complete fusion as a consequence of the continuum-continuum couplings effect is investigated in order to better understand the origin of the complete fusion. As reported the previous chapter in CDCC method is used in calculations and below we give the details of the numerical calculations.

3.1 Details of numerical calculations

The $^{8}\mathrm{B}$ nucleus considered in this study, is modeled as beryllium a core nucleus plus the proton a valence nucleus is loosely bound $^{8}\mathrm{B} \to {}^{7}\mathrm{Be} + p$. The ground state of nucleus ($\tilde{j}_b^{\pi} = 2^{+}$ and $\ell_b = 1$) is obtained by coupling the $0p_{3/2}$ proton orbit to the $\frac{3}{2}^{-}$ ground state of $^{7}\mathrm{Be}$, with a proton binding energy $\varepsilon_b = 0.137\,\mathrm{MeV}$ [111]. The continuum wave functions as well as bound-state were obtained with Woods-Saxon potentials taken from Ref. [112]. These potential parameters are listed in table (3.1). This table, V_0 is usual the depth of the central term, V_{so} the spin-orbit coupling term of the nuclear component, (R_0, R_{so}) the nuclei radii, (a_0, a_{so}) the diffuseness, and R_C the Coulomb radius, respectively.

The value of the Coulomb radius is 2.391 fm.

Table 3.1: The value of the depth of the central term (V_0), spin-orbit coupling ($V_{\rm so}$) terms, nuclei radii ($R_0 = R_{\rm so}$) and diffuseness ($a_0 = a_{\rm so}$) parameters of the $V_{cv}(r)$ potential for $^7{\rm Be} + p$ system, used to calculate the binding energies, as well as bound and continuum wave functions

	V_0(MeV)	R_0(fm)	a_0(fm)	$V_{\rm so}({\rm MeV \cdot fm^2})$	$R_{\rm so}$(fm)	$a_{\rm so}$(fm)
$^7{\rm Be} + p$	-44.65	2.391	0.52	-19.59	2.391	0.52

The depth of the central term V_0 was adjusted to obtain the binding energy from $\varepsilon_b = 0.137$ MeV to $\varepsilon_b = 1.0$ MeV. We follow the same procedure as in Ref. [68]. The $p + {}^{208}{\rm Pb}$ potential parameters were taken from Ref. [113], while for the $^7{\rm Be} + {}^{208}{\rm Pb}$ potential we adopted the parameters of the ^{6}Li global potential [114].

The coupled differential equations (2.65), are numerically integrated with the parameters calculated as follows: the maximum angular momentum between the ^{7}Be core nucleus and the proton was truncated, by $\ell_{\rm max} = 4\hbar$, for $E_{\rm c.m.}/V_{\rm B} < 1.0$ and by $\ell_{\rm max} = 5\hbar$, for $E_{\rm c.m.}/V_{\rm B} \geq 1.0$ (where $V_{\rm B} = 49.36$ MeV is the Coulomb barrier height calculated with the São Paulo potential (SPP) [115]). The maximum matching radius for bin integration was truncated by $r_{\rm max} = 100\,{\rm fm}$, whereas the maximum order of the potential multipole expansion, was taken to be $\lambda_{\rm max} = 5$, and the maximum matching radius of the integration of the coupled differential equations, by $R_{\rm max} = 1000\,{\rm fm}$. The maximum angular momentum of the relative center-of-mass motion, was set at $L_{\rm max} = 1000\hbar$, and the ^{7}Be-p maximum relative momentum, at $k_{\rm max} = 0.6\,{\rm fm}^{-1}$, for $E_{\rm c.m.}/V_{\rm B} < 1.0$, and $k_{\rm max} = 1.0\,{\rm fm}^{-1}$, for $E_{\rm c.m.}/V_{\rm B} \geq 1.0$. The $[0, k_{\rm max}]$ interval was then sliced into momentum bins of widths, $\Delta k = 0.1\,{\rm fm}^{-1}$, for *s*- and *p*-states, $\Delta k = 0.2\,{\rm fm}^{-1}$, for *f*- and *d*-states, and $\Delta k = 0.25\,{\rm fm}^{-1}$ for higher-order partial-waves. The Fresco code [92] was used to performed the numerical calculations.

3.2 Results and Discussion

In figure 3.1, we show the integrated breakup cross sections against the incident energy in the centre-of-mass between $0.4 \leq E_{\rm c.m.}/V_{\rm B} \leq 1.5$, which is obtained in the absence of the continuum-continuum couplings ("No ccc") and in the presence of all the different couplings (“All coupl.”) considered in the coupling matrix elements. One notices that at deep sub-barrier incident energies (i.e., $E_{\text{c.m.}}/V_{\text{B}} \leq 0.6$), the breakup cross sections are indeed enhanced as a consequence of the continuum-continuum couplings, while at ($E_{\text{c.m.}}/V_{\text{B}} > 0.6$), these couplings are usually substantial suppressed the breakup cross section. From these results it can be seen that the continuum-continuum couplings at deep sub-barrier incident energies show the opposite effect when compared with the effect around and above the Coulomb barrier. This result is similar to the one reported in Ref. [47] for the reaction ^{6}Li + ^{208}Pb in the same incident energy range, where the ^{6}Li nucleus has three resonances ($j^{\pi} = 1^{+}, 2^{+}, 3^{+}$) in the $\ell = 2$ continuum states. We noticed that the probabilities for the projectile breakup when entering the region of the absorption or on the outgoing trajectory as a bound system will be high at deep sub-barrier energies. This is further facilitated by the multi-step continuum-continuum couplings which are known to delay the breakup process.

These continuum-continuum couplings are also known to increase the breakup irreversibility and as a result to decrease the flux that penetrates the Coulomb barrier [116]. The projectile-target Coulomb repulsion is strong in the diagonal channel when the projectile as the bound system penetrates the region of the absorption. This is due to the resulting weak nuclear absorption in which is subsequently leading to a large Coulomb breakup. The results of Ref. [68] support this assertion, although when these continuum-continuum couplings are excluded it can lead to a more prompt breakup. The projectile probabilities that enter the region of absorption as a bound system will be low when compared to the case when the continuum-continuum couplings are considered. In this case, at deep sub-barrier energies at the end will weaken the projectile-target diagonal Coulomb repulsion. When more flux is added from the breakup to the fusion channels, the nuclear absorption is enhanced. Then, we argue that the effect of the dynamic will elucidate these continuum-continuum couplings at deep sub-barrier energies that enhanced the breakup cross section. The enhancement is also related to the breakup of a projectile on its outgoing trajectory. Moreover, the results indicate that the bound-state half-life inside the region of absorption is enhanced at deep sub-barrier energies owing to the continuum-continuum couplings. Therefore, we also concluded that the continuum-continuum couplings enhancement on the breakup cross section can not be explained by the breakup

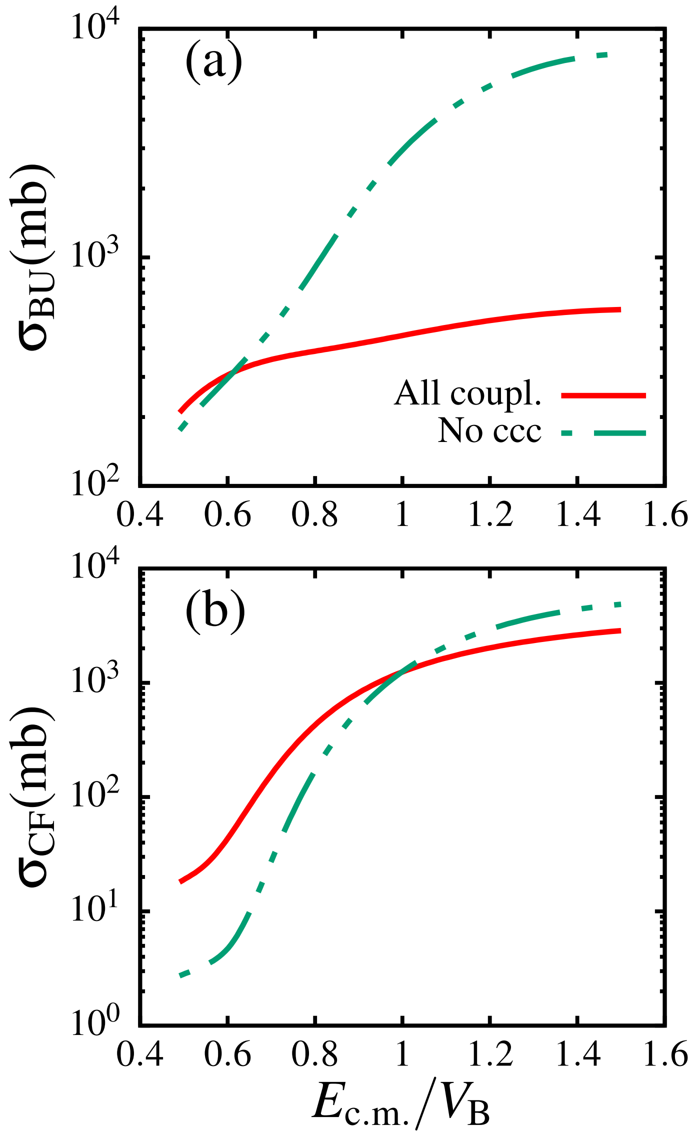

Figure 3.1: Integrated breakup (a) and complete fusion (b) cross sections for different centre-of-mass incident energies scaled by the Coulomb barrier height, in the presence and absence of the continuum-continuum couplings.

prior to reaching the Coulomb barrier.

The complete fusion cross section obtained in the presence and absence of the continuum-continuum couplings is displayed in figure 3.1 (b). From this results the couplings among continuum states is seen to increase the complete fusion cross section at incident energies below and around the Coulomb barrier ($E_{\rm c.m.}/V_{\rm B} \simeq 1.0$), as also observed in Ref. [116]. Notice that this indicates the longer the projectile inside the fusion barrier in a bound-state remains it will contribute more to the complete fusion cross section (i.e., enhancement), as the complete fusion cross section depends on the bound-state. This is an indication that

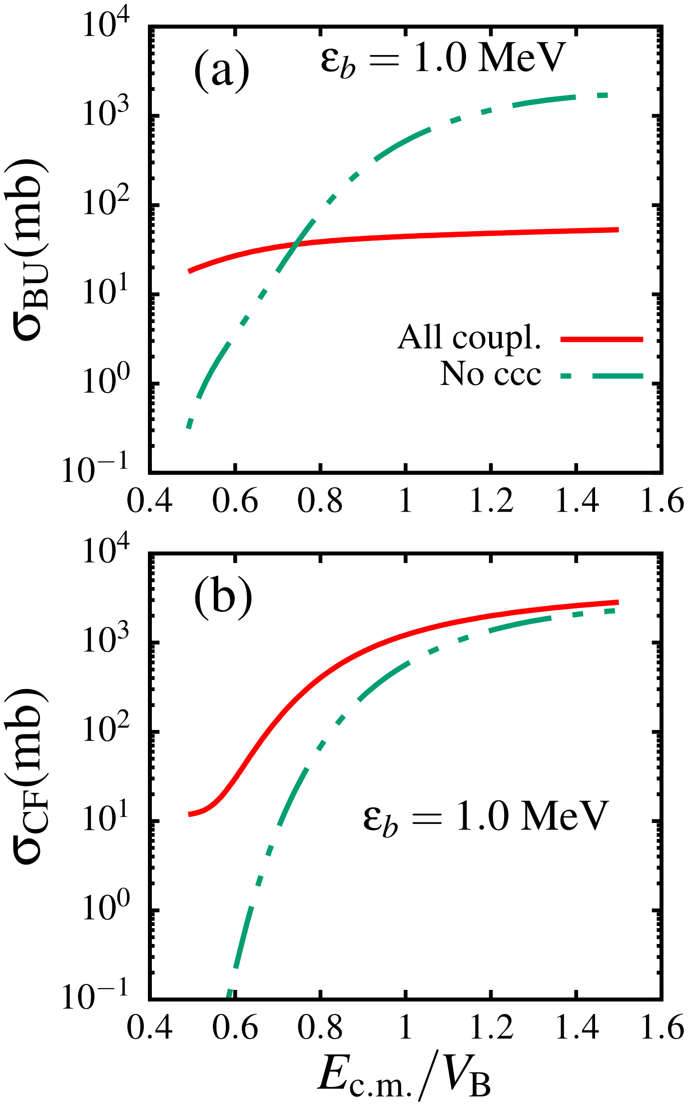

Figure 3.2: Integrated breakup (a) and complete fusion (b) cross sections for different centre-of-mass incident energies scaled by the Coulomb barrier height, in the presence and absence of the continuum-continuum couplings, for the ground-state binding energy $\varepsilon_b = 1.0$ MeV.

the bound-state half-life inside the fusion barrier is increased because of the continuum-continuum couplings. This is also that, in this incident energy region the more flux will contribute to the complete fusion, where the projectile is captured unbroken, which leaves the target inside the Coulomb barrier, in which, the nuclear absorption is less opposed by the Coulomb repulsion. The target strongly repelled the projectile on its incoming trajectory, whereas on its outgoing trajectory it is accelerated. However, the nuclear absorption is expected to act in the same way on both trajectories. Follows from the similar arguments presented in Refs. [50–52], it is also believed that at deep sub-barrier

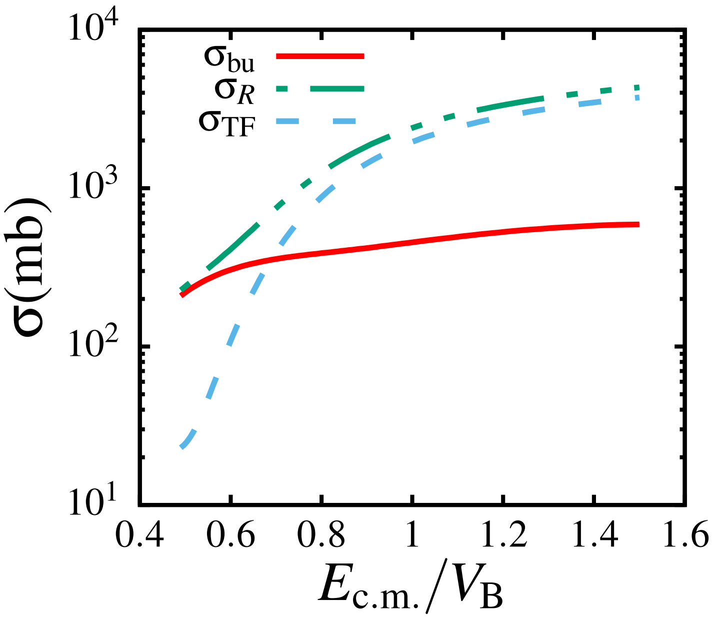

Figure 3.3: Total reaction, total fusion and breakup cross sections as functions of $E_{\text{c.m.}}/V_{\text{B}}$.

energies the complete fusion cross section enhancement cannot be explained by a breakup outside the Coulomb barrier. It is also observed that the continuum-continuum couplings suppressed a complete fusion, as this is reported in other works such as Refs. [47, 116], where the reaction dynamics are quite different above the Coulomb barrier. The breakup probability of the projectile in the asymptotic on the incoming trajectory is high in this energy region, which means this projectile will less likely to reach the absorption region unbroken. This is suggested in Refs. [50–52], that on the incoming trajectory the breakup event location will be crucial to understand the complete fusion suppression.

As the projectile ground-state binding energy is artificially increased a less prompt breakup is further stimulated. This is to ensure that at deep sub-barrier incident energies the breakup process can occur on the outgoing trajectory. The projectile ground-state binding energy from $\varepsilon_b = 0.137$ MeV to 1.0 MeV is artificially increased to get more insights into the conclusions that is made above. In fact the figure 3.2 (a), shows that the breakup cross sections are strongly enhanced at deep sub-barrier energies when compared to lower binding energy in figure 3.1 (a). It seems to suggest that the enhancement of the breakup cross section at deep sub-barrier energies is due to the continuum-continuum couplings, as this indicates that on the outgoing trajectory the projectile is breaking up. It would be interesting to investigate more this assertion. It is also observed in figure 3.2 (b), that

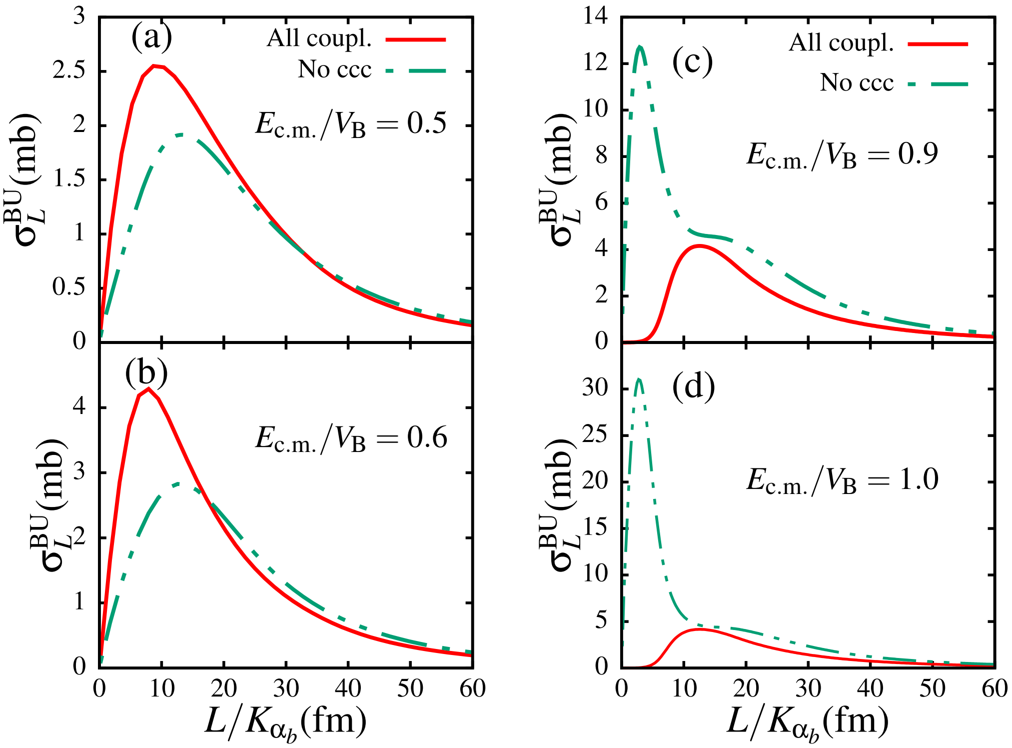

Figure 3.4: Angular momentum distributions cross sections as functions of the ratio L/K_{α_b}, in the presence and absence of the continuum-continuum couplings, for $\varepsilon_{\mathrm{c.m.}}/V_{\mathrm{B}} \leq 1.5$.

the complete fusion cross section is largely enhanced. However, the figure 3.1 (b), shows the transition from enhancement to suppression which does no longer occur above the Coulomb barrier.

The value of $\sigma_{\mathrm{BU}} = 326 \pm 84\,\mathrm{mb}$ is observed in experimental result for the elastic breakup cross section of the reaction under study measured at $E_{lab} = 30$ MeV in Ref. [68]. We obtained the value of 317 mb in our theoretical calculations, which agree quite well with the experimental data. The predominance of the breakup channel where the breakup cross section is reported to exhaust the total reaction cross section (i.e., $\sigma_{\mathrm{BU}}/\sigma_R \simeq 1.0$), is another important result that is confirmed in Ref. [68]. In figure 3.3, we display the breakup cross section, total fusion cross section, and total reaction cross section in order to verify above conclusions. Indeed, one can observe in this figure that, the breakup cross sections accounts for almost the whole total cross sections at deep sub-barrier energies, where we obtained $\sigma_{\mathrm{BU}}/\sigma_R \simeq 0.92$ at $E_{\mathrm{c.m.}}/V_{\mathrm{B}} \leq 0.6$. Therefore, it is clear that the continuum-continuum couplings enhancement on the breakup cross section is the factor that justify the predominance of the breakup channel at deep sub-barrier energies. Although, in our calculation the total fusion cross sections are negligible compared to the total reaction cross section as well as breakup cross section which represents about 30 mb. Therefore, we believed that a measurement of total fusion can be performed for the ^{8}B + ^{208}Pb reaction at 30 MeV and even slightly below. As suggested in Ref. [68], this is an important measurement from an astrophysical perspective.

Let us now discuss the breakup cross section enhancement at deep sub-barrier energies ($E_{\rm c.m.}/V_{\rm B} \leq 0.6$), which is shown in figure 3.1. From this figure, we resorted nuclear absorption concept in the inner region. The breakup cross section in the inner region needed to be enhanced by the continuum-continuum couplings in order for the argument to be corroborated at deep sub-barrier energies. We display the angular momentum distributions breakup cross sections against the ratio L/K_{α_b} in order to verify this argument in figure 3.4, where $L = K_{\alpha_b}R$ is the ratio that denotes the radial distance through the classical relation with K_{α_b} the wave-number in the entrance channel. Observing this figure, one can notice that for $E_{\rm c.m.}/V_{\rm B} \leq 0.6$ (left panels), when these continuum-continuum couplings are excluded seems to prevail the breakup cross section in the peripheral region, while the breakup cross section is more important in the inner region when the continuum-continuum couplings are included. One then concludes that in this energy range the predominance of the breakup channel will elucidate the enhancement of the breakup cross section in the inner region at deep sub-barrier energies due to the continuum-continuum couplings, and among other factors. These results will pave a way towards a further investigation of the breakup effect on nuclear astrophysical quantities of interest.

To summarize in detailed this chapter, the total fusion cross section, breakup cross section as well as the total reaction cross section for proton-halo reaction due to the continuum-continuum couplings effect at deep sub-barrier, around, and above the Coulomb barrier incident energies were investigated. In this case the complete fusion cross section is enhanced at sub-barrier energies, whereas at above-barrier energies is suppressed due to the continuum-continuum couplings. It is observed that when continuum-continuum couplings are included the breakup cross section is enhanced at deep sub-barrier energies. In general, we found that the total fusion cross section is negligible compared to the total reaction cross section or breakup cross section. From this, we concluded that the predominance of the breakup channel will elucidate the breakup cross section enhancement at deep sub-barrier energies. In the following chapter, we investigated the breakups of an open neutron-halo reaction with different target in the zero ground state binding energy limit.

Chapter 4

Breakup dynamics of an open two-body quantum neutron-halo system

---

In this chapter, we investigate the breakup dynamics of an open neutron-halo ^{11}Be$+^{64}$Zn, ^{11}Be $+$ ^{208}Pb and ^{37}Mg $+$ ^{208}Pb reactions in the zero ground state binding energy limit ($\varepsilon_b \to 0$). The effect of the linearity of the ground-state wave function on the breakup and elastic scattering cross sections, starting with a convergence are analyzed for ^{11}Be$+^{64}$Zn reaction. The dependence of the total reaction, total fusion, and breakup cross sections on the binding energy are also investigated. The effects of the convergence on the finite elastic scattering and breakup cross sections are analyzed for both ^{11}Be and ^{37}Mg neutron halo nuclei on a ^{208}Pb target. In order to understand better about the convergence of the s-wave or p-wave neutron halo nuclei. The same method is used to perform the numerical calculations as mentioned in chapter 3.

4.1 The ^{11}Be$+^{64}$Zn reaction

4.1.1 Details of numerical calculations

In this work, the ^{10}Be$\otimes n(2s_{\frac{1}{2}^+})$ ground state configuration for ^{11}Be nucleus is adopted, with a neutron separation energy of $\varepsilon_b = 0.504\,$MeV [117]. The first excited bound state has an excitation energy of $\varepsilon_{\rm ex}$ =0.183 MeV, and parity $j_b^\pi = \frac{1}{2}^-$. A narrow resonance, with ε_{res} =1.274 MeV, is located in the $j^\pi = \frac{5}{2}^+$ partial wave. The parameters of the ^{10}Be-neutron Woods-Saxon potential, which were used to obtain bound-state resonant state and continuum wave functions, similar to those used in Ref. [72] (adopted from Ref. [73]), are $V_0 = -59.5$ MeV, $V_{\text{so}} = -32.8\,\text{MeV}\cdot\text{fm}^2$, $R_0 = R_{\text{so}} = 2.699\,\text{fm}$ and $a_0 = a_{\text{so}} = 0.6\,\text{fm}$, where V_0 and V_{so}, are the depth of the central and spin-orbit coupling terms, and R_0, R_{so}, and a_0, a_{so}, the corresponding radii and diffuseness, respectively. For partial-waves other than $\ell = 0$ (including the $\ell = 2$ resonance), we used $V_{\ell>0} = 40.5\,\text{MeV}$. We adjusted V_0 to obtain the wave functions corresponding to the other binding energies 0.1 MeV, 10.0 keV, 0.10 keV and 0.01 keV. The parameters of the ^{10}Be + ^{64}Zn optical potential, were taken from Ref. [71], whereas for the n + ^{64}Zn optical potential, the global parametrization of Ref. [118], was adopted. The depth of the real part of the latter potential was slightly modified to better fit the experimental data. The different parameters used in the numerical solution of the CDCC coupled differential equations are summarized in Table 4.1. This table,

Table 4.1: Parameters used in the numerical solution of the CDCC coupled differential equations.

ℓ_{max}	λ_{max}	ε_{max}	r_{max}	Δr	L_{max}	R_{max}	Δ_R
($\hbar$)	-	(MeV)	(fm)	(fm)	($\hbar$)	(fm)	(fm)
6	6	10	200	0.1	10000	1000	0.005

ℓ_{max} is the ^{10}Be- neutron maximum angular momentum, λ_{max}, the maximum order of the potential multipole expansion, ε_{max}, the maximum bin energy, r_{max}, the maximum matching radius for bin potential integration, Δr, the integration step size associated with r_{max}, R_{max}, the maximum matching radius in the numerical integration of the coupled differential equations, ΔR, the integration step size associated with R_{max}, and L_{max}, the maximum angular momentum of the relative center-of-mass motion. The $[0 : \varepsilon_{\text{max}}]$ interval was discretized into energy bins of widths, $\Delta\varepsilon = 0.5\,\text{MeV}$, for s- and p-states, $\Delta\varepsilon = 1.0\,\text{MeV}$, for f- and d-states and $\Delta\varepsilon = 1.5\,\text{MeV}$ for g-states, and $\Delta\varepsilon = 2.0\,\text{MeV}$, for higher partial waves. Finer bins were considered for the resonant partial wave. The numerical calculations are carried out using Fresco [67].

4.1.2 Results and Discussion of the $^{11}\mathrm{Be} + {}^{64}\mathrm{Zn}$ reaction

4.1.3 Projectile structure

In figure 4.1, we plot the ground-state wave functions corresponding to the different ground-state binding energies considered. We observe in this figure that for $\varepsilon_b \geq 0.1\,\mathrm{MeV}$, the wave function exhibits the natural boundary conditions, rapidly decaying to zero as r becomes large ($r \geq 30\,\mathrm{fm}$). However, while for $\varepsilon_b \leq 0.10\,\mathrm{keV}$, wave function is negligible in the inner region ($r \leq 5\,\mathrm{fm}$), it becomes linear outside, with $\lim\limits_{r\geq 5} \phi^{j_b}_{\ell_b}(k_b, r) \to -0.1$. This is an indication that the probability of finding the neutron within the core radius decreases to zero. Therefore, considering the linearity of the ground-state wave function to be one of the criteria of an open system, we can conclude that for $\varepsilon_b \leq 0.10\,\mathrm{keV}$, the $^{10}\mathrm{Be} + n$, has already reached the state on open neutron-halo system, with an extended density to infinity, and an infinite scattering length ($a_s \to -\infty$). It is further noted that in the $\varepsilon_b \to 0$ limit, the wave function becomes less sensitive to the binding energy. Given the dependence of the breakup process on the ground-state wave function, this convergence may signal the convergence of the breakup observables in the $\varepsilon_b \to 0$ limit.

To just give a sense of how a linear ground-state wave function plays out on the size of the system, we calculated the root-mean-square radius for each wave function. We truncated the integration by $r = 200\,\mathrm{fm}$, even though the integration would not convergence for a linear wave function. The results in Table 4.1, show how quickly the size of the system can grow as the ground-state binding energy decreases, where a convergence trend is noticed as $\varepsilon_b \to 0$. We can further analyze the effect of the ground-state binding energy of the internal structure of the system, by considering the dipole electric response function $[B(E1)]$. It is connected to the size of the system ($\langle r^2 \rangle$), through the following non-energy-weighted cluster sum rule as proposed in [119]

$$B(E1) = \left(\frac{3}{4\pi}\right)\left(\frac{Z_p e}{A_p}\right)^2 \langle r^2 \rangle, \tag{4.1}$$

where $Z_p = 4$ and $A_p = 11$, are projectile number of protons, and atomic mass number, respectively. Table 4.1, also shows how dramatic $B(E1)$ increase as the binding energy decreases, with a slow convergence as $\varepsilon_b \to 0$.

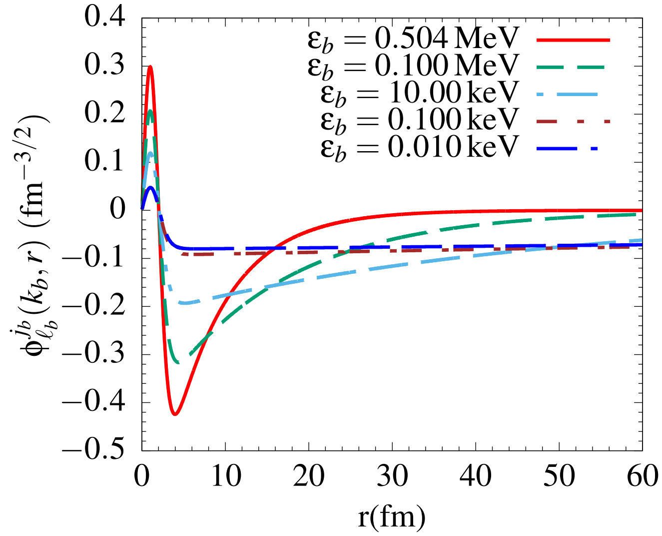

Figure 4.1: Ground-state bound state wave functions for $\varepsilon_b = 0.504\,\mathrm{MeV}$ and $0.10\,\mathrm{keV}$ binding energies.

Table 4.2: Root-mean-square radii and dipole electric response functions, for different ground-state binding energies. The experimental values $\sqrt{\langle r^2\rangle} = 5.77 \pm 0.16\,\mathrm{fm}$, and $B(E1) = 1.05 \pm 0.06\,\mathrm{e^2fm^2}$, were taken from Ref. [75].

Binding energy	0.504 MeV	0.1MeV	10 keV	0.1 keV	0.010 keV
$\sqrt{\langle r^2\rangle}$[fm]	5.62	10.24	28.50	81.85	89.16
$B(E1)$[e^{2}fm^2]	0.99	3.31	25.60	211.20	250.63

4.1.4 Elastic scattering cross sections

In order to verify our assertion in Chapter 2, regarding the convergence of the elastic scattering cross section, figure 4.2, displays the elastic scattering cross section, scaled by the Rutherford cross section, for different values of $r_{\max}$, where only results corresponding to $\varepsilon_b = 0.504\,\mathrm{MeV}$ (upper panel) and $0.010\,\mathrm{keV}$ (lower panel), are shown. As expected, we observe in the upper panel that for $\varepsilon_b = 0.504\,\mathrm{MeV}$, the results have already converged for $r_{\max} = 100\,\mathrm{fm}$. This rapid convergence is due to the fact that at $r_{\max}$=100 fm, the corresponding ground-state wave function has long collapsed to zero, as shown in figure 4.1, such that $r_{\max} \geq 30\,\mathrm{fm}$ do not contribute to the radial integral (2.80). A nice agreement with the experimental data taken from Ref. [74], is also noticed in this figure. Now, as anticipated, the lack of convergence due to the linearity of the ground-state wave function, is clearly verified in the lower panel, for $\varepsilon_b = 0.010\,\mathrm{keV}$, although the elastic scattering cross section keeps decreasing as $r_{\max}$ increases. Therefore, our first conclusion is that, the elastic scattering cross section which depends on the density of the ground-state wave function, does not convergence for an open neutron-halo system, due to the linearity of the associated ground-state wave function.

4.1.5 Angular distributions differential breakup cross sections

We start with a discussion on the comparison of the angular distributions breakup cross sections with the available experimental data of Ref. [71]. As one can see in figure 4.3, our theoretical calculations fairly describe the data, although they miss three data points at the maximum (around 20°), and the trend is to overestimate the data for $\theta > 20^\circ$. Similar calculations in Ref. [74], largely underestimated the data. It was then asserted that the disagreement could be mainly due to the lack of core excitations, in the description of the projectile. However, simple calculations that took into account long-range potentials in Ref. [76], perfectly agreed with the data. A look at figure 3 of Ref. [83] (where CDCC calculations that include core excitations were carried out), shows a fair agreement with the present calculations. One would then argue that the choice of the core-target and fragment-target optical potentials is crucial in these calculations, when one intends to fit experimental data. Such choice would impact on the implicit target excitations stimulated by these potentials.

As mentioned else where in this thesis, we have argued that despite the linearity of the ground-state wave function, the convergence of the breakup cross section of an open quantum system can still be achieved. To demonstrate this, we present in figure 4.4, the angular distributions differential breakup cross sections for different values of $r_{\max}$. Observing this figure, one also notices that for ε_b =0.504 MeV (upper panel), the convergence is already achieved for $r_{\max} = 100\,\text{fm}$, similar to the upper panel of figure 4.2. This rapid convergence can be explained by the fact that for $r \geq 30$ fm, the ground-state wave function has already decayed to zero, implying that $\lim\limits_{r\geq 30} \phi_{\ell_b}^{j_b}(k_b, r) \times \varphi_{\ell}^{j}(k_i, r) \to 0$, and the bin wave functions can be expected to have attained orthogonality for $r \geq 100\,\text{fm}$. Interestingly, for $\varepsilon_b = 0.01\,\text{keV}$ (lower panel), a satisfactory convergence trend for $r_{\max} = 200\,\text{fm}$ is observed, particularly at lower angles ($\theta \leq 40^\circ$). At large angles ($\theta > 40^\circ$), we notice that the breakup cross section decreases as $r_{\max}$ increases, where also a convergence trend is maintained. As shown in equation (2.78), the radial integral of the continuum-continuum couplings is independent of the ground-state wave function, hence it is not affected by the linearity of the latter. On the other hand, due to the orthogonality of the bin wave functions, which is all but guaranteed for $r_{\max} \geq 200\,\mathrm{fm}$, the radial integral of the couplings to and from the bound-state will convergence, despite a linear ground-state wave function, leading to the convergence of the breakup cross section. In conclusion, despite a linear ground-state wave function, a converged breakup cross section in the breakup of an neutron-halo open system is obtained, thanks to the orthogonality of the bin wave functions. This makes the CDCC formalism uniquely valid to handle such calculations.

In order to better analyze the dependence of the breakup cross section on the ground-state binding energy, in figure 4.5, the angular distributions breakup cross sections for the different binding energies are presented. This figure displays an interesting dependence of the breakup cross section on the ground-state binding energy. At forward angles ($\theta \leq 40^\circ$), the breakup cross section is substantially enhanced as the binding energy decreases, but becomes less sensitive as $\varepsilon_b \to 0$, as also observed in figure 4.1, on the ground-state wave function. However, the opposite trend is observed at backward angles, where the breakup cross section decreases with the binding energy. Among other factors, this decrease can be associated with a negligible diagonal Coulomb repulsion as $\varepsilon_b \to 0$, which reduces the natural long tail of the Coulomb breakup cross section in the absorption region.

The total reaction, fusion and breakup cross sections are presented in figure 4.6, as functions of the ground-state binding energies. We observe in this figure that all three cross sections are independent on the ground-state binding energy as $\varepsilon_b \to 0$. Also, as anticipated in the introduction, in this binding energy region, the total breakup cross section is similar to the breakup cross section, whereas the fusion cross section is less relevant compared to its breakup counterpart. What is interesting is that the fusion cross section is non-zero even though it emanates from the absorption due to the imaginary part of the nuclear potential. As the breakup occurs asymptotically, the effect of the nuclear potential, which is short-ranged, is expected to vanish. However, a non-vanishing fusion cross section in this case can be understood to stem from the peripheral nuclear absorption due to the infinite density of the ground-state wave function.

4.2 The $^{11}\mathrm{Be} + {}^{208}\mathrm{Pb}$ and $^{37}\mathrm{Mg} + {}^{208}\mathrm{Pb}$ reactions

4.2.1 Details of numerical calculations

As previously mentioned, for the ^{11}Be projectile, we adopt the $^{10}\mathrm{Be}(0^+) \otimes n(2s_{\frac{1}{2}^+})$ configuration, where the valence neutron is loosely-bound to the inert core nucleus by a binding energy $\varepsilon_b = 0.504\,\mathrm{MeV}$ [111]. Apart from the ground-state this system also exhibits a first excited bound-state with energy $\varepsilon_1 = 0.183\,\mathrm{MeV}$ in $p_{\frac{1}{2}^-}$ state, and a narrow resonance with energy $\varepsilon_{res} = 1.274\,\mathrm{MeV}$, in the $d_{\frac{5}{2}^+}$ continuum state. As for the ^{37}Mg projectile, we consider both $^{36}\mathrm{Mg}(0^+) \otimes n(3s_{\frac{1}{2}^+})$ and $^{36}\mathrm{Mg}(0^+) \otimes n(2p_{\frac{3}{2}^-})$ configurations, where the valence neutron is loosely-bound to the inert core nucleus by a binding energy $\varepsilon_b = 0.22\,\mathrm{MeV}$ [120]. For ^{11}Be nucleus, the ground-state is identified by $\alpha_b \equiv (\ell_b, s, I_c, j_b^\pi) = (0, \frac{1}{2}, 0, \frac{1}{2}^+)$ quantum numbers, where $\ell_b = 0$, is the orbital angular momentum, $s = \frac{1}{2}^+$, the nucleon's spin, $I_c = 0$, the spin of the core nucleus, and $j_b^\pi = \frac{1}{2}^+$ (π is the parity), the total angular momentum ($\boldsymbol{j}_b = \boldsymbol{\ell}_b + \boldsymbol{s}$). For ^{37}Mg nucleus, the ground-state is identified by $\alpha_b \equiv (0, \frac{1}{2}, 0, \frac{1}{2}^+)$ (for s-wave state) and by $\alpha_b \equiv (1, \frac{1}{2}, 0, \frac{3}{2}^-)$ (for p-wave state).

4.2.2 Description of numerical parameters

In order to numerically solve CDCC coupled differential equations, one needs the projectile bound and bin states as inputs. In our case, these are obtained by solving the Schrödinger equation that describes the core-neutron relative motion, using the following parameters of the $V_{cv}(r)$ potential are summarized in Table 4.3. For the $^{10}\mathrm{Be} + n$ system, these parameters were taken from Ref. [73]. These parameters reproduce the ground-state, first excited bound-state as well as the resonance energies. For the $^{36}\mathrm{Mg} + n$ system, the parameters were taken from Ref. [121], except the depth of the central term (V_0) which was adjusted to reproduce the experimental ground-state binding energy. The same approach was followed for both systems in calculating the other binding energies considered.

The parameters of the real and imaginary parts of the $^{10}\mathrm{Be} + {}^{208}\mathrm{Pb}$ optical potential, also taken from Ref. [73], are $V_0 = -70\,\mathrm{MeV}$, $R_0 = 7.43\,\mathrm{fm}$, $a_0 = 1.04\,\mathrm{fm}$, $W_V = -58.9\,\mathrm{MeV}$, $R_W = 7.19\,\mathrm{fm}$, and $a_W = 1.0\,\mathrm{fm}$. The parameters of the the $n + {}^{208}\mathrm{Pb}$ optical potential,

Table 4.3: Values of the central (V_0), spin-orbit coupling ($V_{\rm so}$) terms, nuclei radii ($R_0 = R_{\rm so}$) and diffuseness ($a_0 = a_{\rm so}$) parameters of the $V_{cv}(r)$ potential for both $^{10}\mathrm{Be}+n$ and $^{36}\mathrm{Mg}+n$ systems, used to calculate the binding energies, as well as bound and continuum wave functions

	ℓ_b	j_b^π	V_0(MeV)	$V_{\rm SO}$(MeV $\cdot$ fm^2)	R_0(fm)	a_0(fm)
$^{10}\mathrm{Be}+n$	0	$1/2^+$	-59.5	-32.8	2.699	0.6
$^{36}\mathrm{Mg}+n$	0	$1/2^+$	-66.340	-9.8	3.962	0.7
	1	$3/2^-$	-45.560	-9.8	3.962	0.7

were taken from the global parametrization of Becchetti [118]. In order to compare our calculations with the differential breakup cross section data of Ref. [122] for the $^{11}\mathrm{Be}+{}^{208}\mathrm{Pb}$ reaction, we adjusted the depth of the central term, and removed the surface term. For the $^{36}\mathrm{Mg}+{}^{208}\mathrm{Pb}$ optical potential, we used the global parametrization of Akyuz-Winther [123]. The other numerical parameters needed (CDCC model space) are listed in Table 4.4, where

- $\ell_{\rm max}$: the maximum core-nucleon orbital angular momentum,
- $\lambda_{\rm max}$: the maximum order in the potential multipole expansion,
- $k_{\rm max}$: the maximum relative momentum,
- $r_{\rm max}$: the maximum matching radius for bin integration,
- Δr: the integration step size associated with $r_{\rm max}$,
- $R_{\rm max}$: the maximum matching radius in the numerical integration of the coupled differential equations,
- ΔR: the integration step size associated with $R_{\rm max}$, and
- $L_{\rm max}$: the maximum orbital angular momentum of the projectile-target relative center-of-mass motion.

The interval $[0 : k_{\rm max}]$ was discretized into momentum bins of widths, $\Delta k = 0.05\,\mathrm{fm}^{-1}$, for s- and p-states, $\Delta k = 0.10\,\mathrm{fm}^{-1}$, for f- and d-states, $\Delta k = 0.15\,\mathrm{fm}^{-1}$ for g-states, and $\Delta k = 0.20\,\mathrm{fm}^{-1}$, for higher partial waves. Finer bins were considered in the resonant states. These parameters were selected in order to satisfy the convergence requirement of

Table 4.4: Parameters used in the numerical solution of the CDCC coupled differential equations.

$\ell_{\max}$ ($\hbar$)	$\lambda_{\max}$ -	$k_{\max}$ (fm^{-1})	$r_{\max}$ (fm)	Δr (fm)	$L_{\max}$ ($\hbar$)	$R_{\max}$ (fm)	ΔR (fm)
7	6	1.2	200	0.1	10000	1000	0.05

the numerical calculations, in particular for $\varepsilon_b = 10^{-4}\,\mathrm{MeV}$, where a larger $r_{\max}$ and $L_{\max}$ were required. The numerical calculations were also performed using Fresco [67].

4.2.3 Results and Discussion of the $^{11}\mathrm{Be} + ^{208}\mathrm{Pb}$ and $^{37}\mathrm{Mg} + ^{208}\mathrm{Pb}$ reactions

To show that for an s-wave neutron-halo system, the ground-state density extends to infinity in the zero binding energy limit, we show in figure 4.7 (a), the ground-state density of the $^{36}\mathrm{Mg} + n$ system for the s-wave configuration, where $\ell_b = 0$. Indeed, as one can observe in this figure, for $\varepsilon_b \leq 10^{-3}\,\mathrm{MeV}$, the density is extended to infinity, i.e., it becomes unbound. The same trend was observed for the $^{10}\mathrm{Be} + n$ although the results are not shown here. We notice in figure 4.7 (b) for the p-wave configuration where $\ell_b = 1$, that the ground-state centrifugal barrier prevents the extension to infinity of the ground-state density, as also obtained in Ref. [66], for $\ell_b = 2$.

In order to assess the implication of the unboundness of the ground-state density, figure 4.8 displays the integrand of the radial integral (2.106) for the $^{10}\mathrm{Be}+n$ system. The scattering wave function $\phi_\ell^j(k,r)$, was calculated in the resonance partial wave (i.e., $\ell = 2, j = \frac{5}{2}^+$) at a continuum energy of $\varepsilon = 1.3\,\mathrm{MeV}$, which is approximately the resonance energy, and $\lambda = 1$. The ground-state wave function in figure 4.8 (a) corresponds to the experimental binding energy $\varepsilon_b = 0.504\,\mathrm{MeV}$, and the ground-state wave function in figure 4.8 (b), corresponds to the binding energy $\varepsilon_b = 10^{-4}\,\mathrm{MeV}$, for which is function becomes unbound. One observes in figure 4.8 (a) that this integrand quickly converges to zero for $r \geq 20\,\mathrm{fm}$, due to the natural asymptotic behavior of the ground-state wave function. In this case, the radial integral (2.106), has no convergence issues. However, in figure 4.8 (b), where the ground-state wave function is unbound, the integrand just behaves as a scattering wave function, in which case, the radial integral (2.106) will not converge. Consequently, the first-order Coulomb breakup cross section (2.103), will highly oscillate and cannot converge in the zero binding energy limit. As shown in Ref. [66] (figure 3), the radial integral (2.106), converges when the pure scattering wave functions are replaced by the square-integral bin wave functions.

To prove that the first-order theory cannot handle the breakup of a system whose ground-state wave function becomes unbound, we use equation (2.103), to calculate the first-order Coulomb breakup cross section. The results are show in figure 4.9, only for the ^{11}Be projectile, considering an incident energy $E_{lab} = 140\,\mathrm{MeV}$. Observing this figure, we note that for $\varepsilon_b = 0.504\,\mathrm{MeV}, 10^{-2}\,\mathrm{MeV}$, the breakup cross section curve is smooth and finite around $\varepsilon = 0\,\mathrm{MeV}$. However, for $\varepsilon_b = 10^{-3}\,\mathrm{MeV}$ the cross section not only diverges around $\varepsilon = 0\,\mathrm{MeV}$, but also starts to oscillate and becomes highly oscillatory for $\varepsilon_b = 10^{-4}\,\mathrm{MeV}$. This is a reflection of the integrand of the radial integral (2.106) in figure 4.8.

In figure 4.10, for the same reaction at the same incident energy, we show the results obtained with the CDCC calculations. As shown by equation (2.44), in the CDCC formalism, the projectile pure scattering wave functions are replaced with square-integrable bin wave functions, such that the breakup matrix elements have no convergence issues. We observe in this figure, unlike in figure 4.9, that there is no oscillations in the cross section even for $\varepsilon_b = 10^{-4}\,\mathrm{MeV}$, which reflects a smooth convergence of the radial integral (2.78). We also notice a convergence of the cross section to a finite value as $\varepsilon_b \to 0$.

To further assess the convergence of the s-wave neutron-halo breakup cross section in the zero binding energy limit, we analyze the angular-distributions breakup cross sections for both ^{11}Be and ^{37}Mg projectile. The results are presented in figure 4.11 for ^{11}Be projectile and in figure 4.11 for ^{37}Mg. In figure 4.11, one sees that the breakup cross section becomes insensitive to the variation of the binding energy for $\varepsilon_b \leq 10^{-3}\,\mathrm{MeV}$, and for $\varepsilon_b \leq 10^{-2}\,\mathrm{MeV}$, in figure 4.12. These results are similar to those obtained in Refs. [65,66], for different systems, with nonzero ground-state orbital angular momenta. The data points in figure 4.11, which are well fitted by the breakup cross section corresponding to the experimental ground-state binding energy, were taken from Ref. [122]. As in Ref. [124], an incident energy about $E_{lab} = 211\,\mathrm{MeV}$ (which is about twice the Coulomb barrier height), was considered for ^{37}Mg projectile.

Let us now consider the elastic scattering whose matrix elements contain the projectile ground-state density and does not involve bin wave functions. In the zero binding energy limit where this density becomes unbound for the s-wave neutron-halo system, these matrix elements will not converge. To highlight this, we show in figure 4.13, the elastic scattering cross sections for both s-and p-wave ground-state configurations of the ^{36}Mg$+n$ system. We observe that for the s-wave configuration [figure 4.13 (a)], contrary to the breakup cross section, the elastic scattering cross section does not converge to a finite value since the elastic scattering cross section corresponding to $\varepsilon_b = 10^{-3}\,$MeV is quite different from the one corresponding to $\varepsilon_b = 10^{-4}\,$MeV. For the p-wave configuration [figure 4.13 (b)], one sees that the elastic scattering cross section converges as it becomes fairly independent of the variation of the binding energy in zero limit. This is in accordance with figure 4.7 (b), where the ground-state density appears to remains finite even as $\varepsilon_0 \to 0$.

To summarize this chapter, we focused on the investigation of the elastic scattering, total fusion, breakup, and total reaction cross sections of an open neutron-halo reaction in the binding energy ($\varepsilon_b \to 0$). In particular we studied the linearity effect of the ground-state wave function on the elastic scattering and breakup cross sections. Due to the linearity of the ground-state wave function it is found that the elastic scattering cross section fails to converge as $\varepsilon_b \to 0$. We also found that these breakup observables, i.e., total reaction, fusion and breakup cross sections, become almost independent of the ground-state binding energy in this limit. We assessed the s-wave neutron-halo breakup cross section convergence in the zero ground-state binding energy limit for both ^{11}Be + ^{208}Pb and ^{37}Mg + ^{208}Pb reactions. We found that the first order perturbation theory can not explain the breakup of a system whose ground state wave function becomes unbound. In the CDCC calculation, when the pure scattering wave function is replaced by the square-integral bin wave functions, the breakup matrix elements have no convergence issues. In the next chapter, we focused on the comparison of the total, Coulomb and nuclear breakup cross sections when all the different couplings are included or excluded in the coupling matrix elements in the reaction that involve the heavy target.

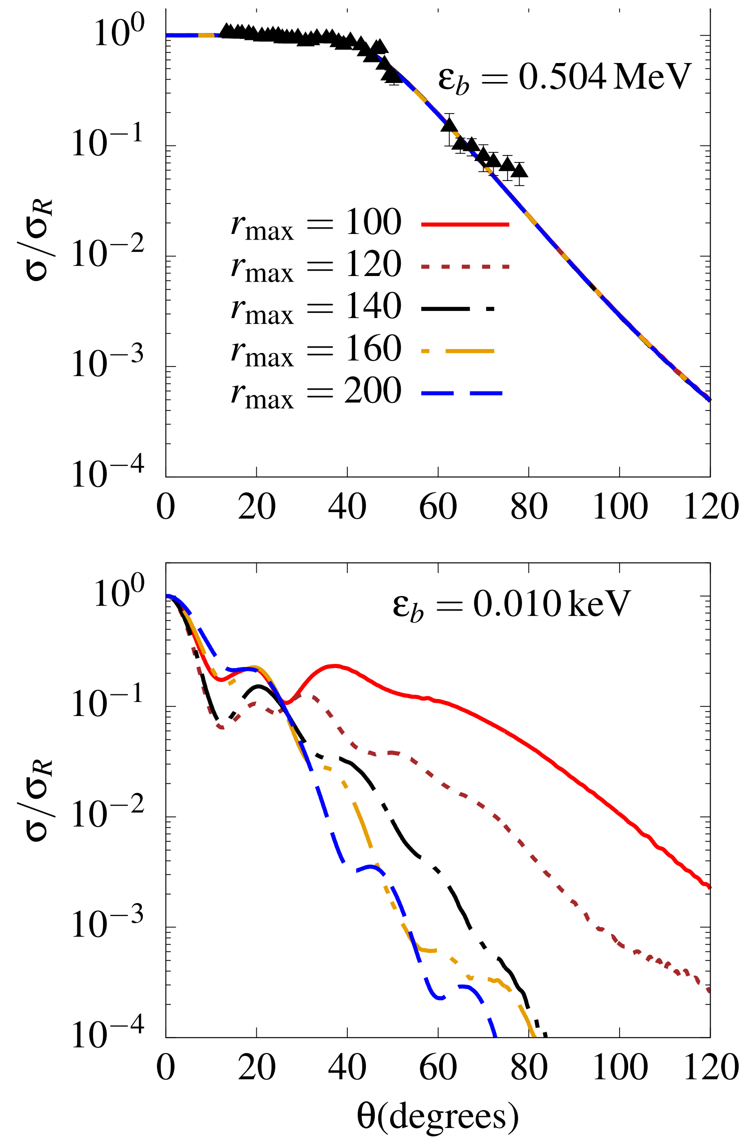

Figure 4.2: Convergence of the elastic scattering cross section (scaled by the Rutherford cross section) in terms of $r_{\max}$, for $\varepsilon_b = 0.504\,\text{MeV}$ (upper panel) and $\varepsilon_b = 0.10\,\text{keV}$ (lower panel) ground state binding energies. The experimental data were taken from Ref. [74].

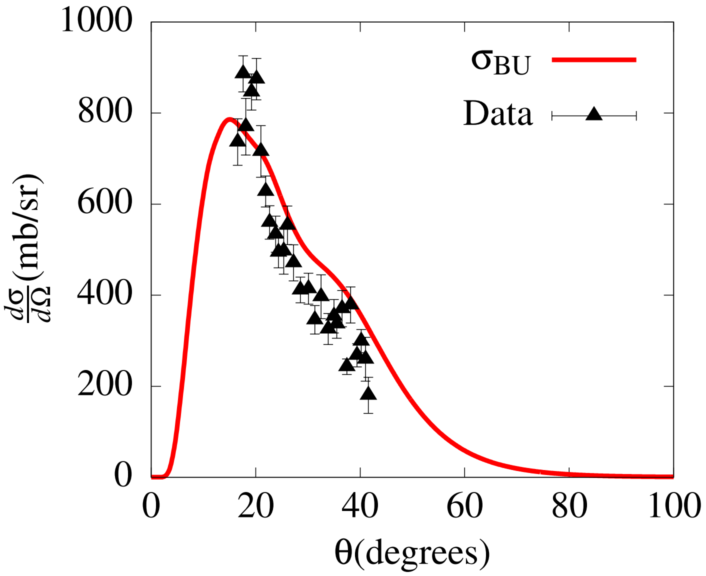

Figure 4.3: Angular distributions differential breakup cross sections, compared with the experimental data, taken from Ref. [71].

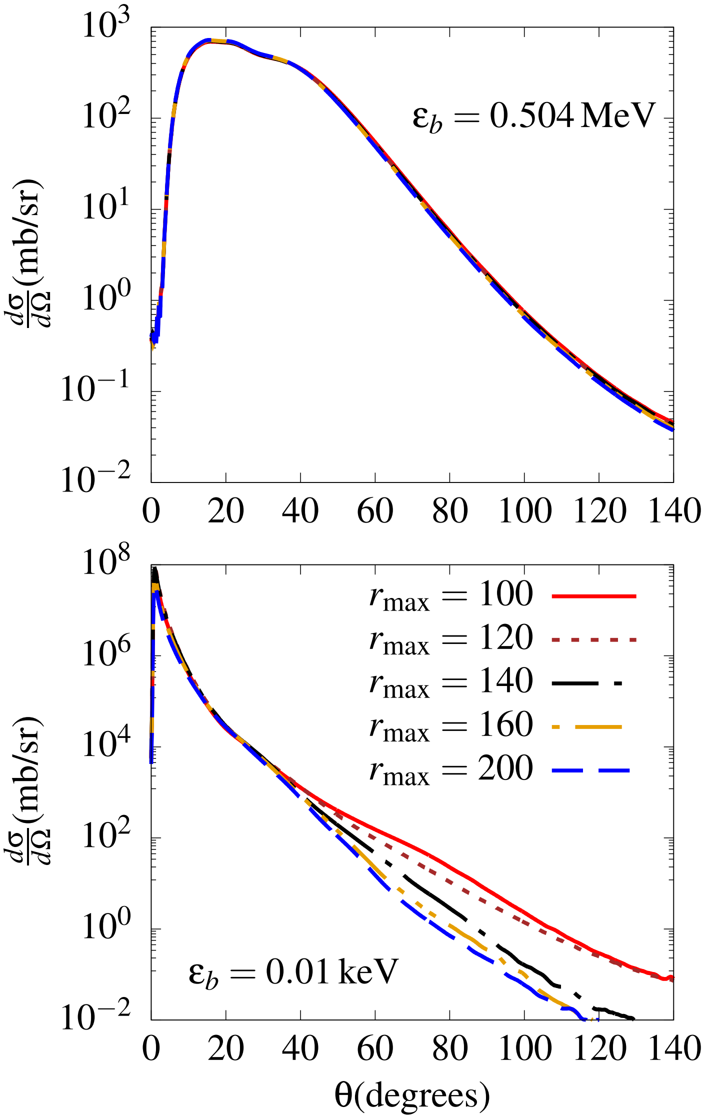

Figure 4.4: Convergence of the angular distributions differential total breakup cross section in terms of r_{max}, for $\varepsilon_b = 0.504\,\text{MeV}$ (upper panel) and $\varepsilon_b = 0.010\,\text{keV}$ (lower panel) ground state binding energies.

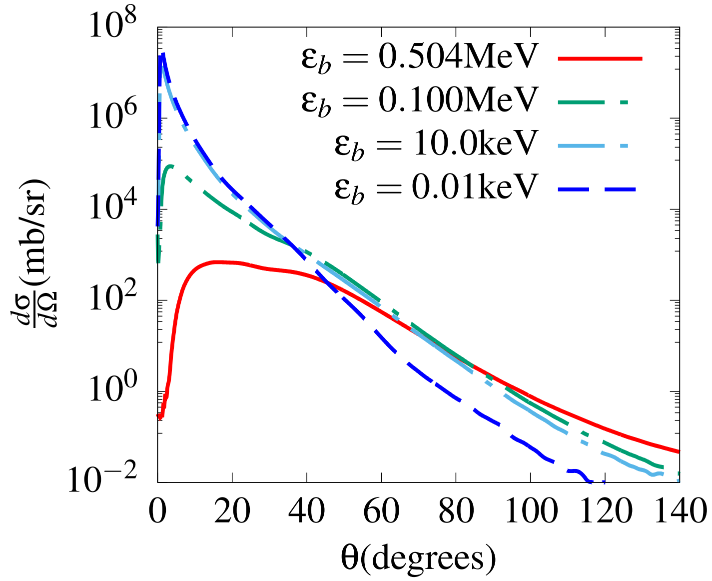

Figure 4.5: Angular distributions differential breakup cross sections for the different ground-state binding energies.

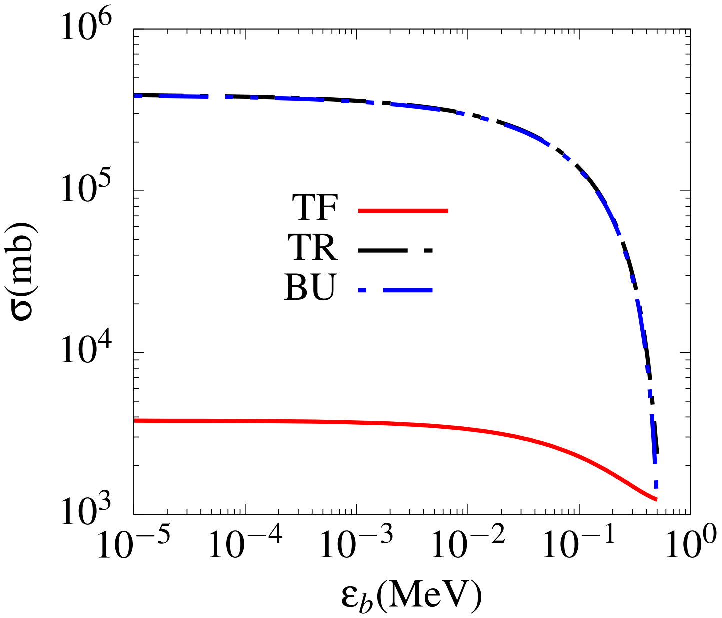

Figure 4.6: Total reaction, fusion and breakup cross sections as function of the ground-state binding energies.

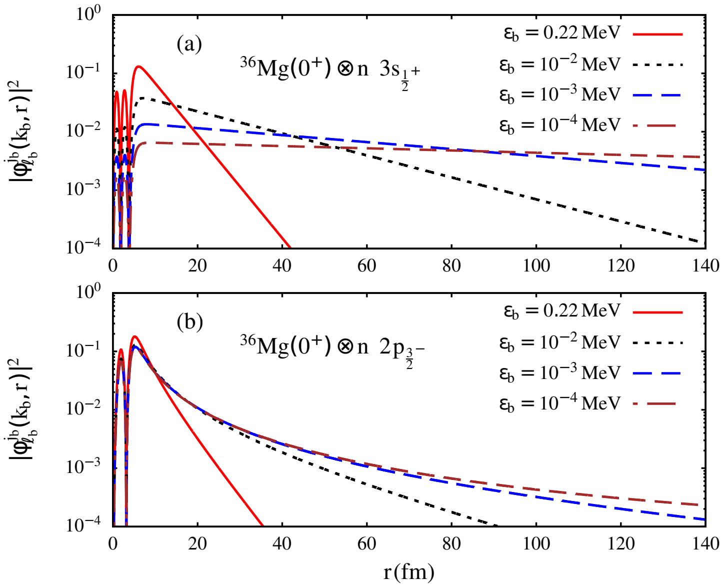

Figure 4.7: Ground-state density for the two different configurations of the ^{36}Mg + n system, corresponding to different ground-state binding energies.

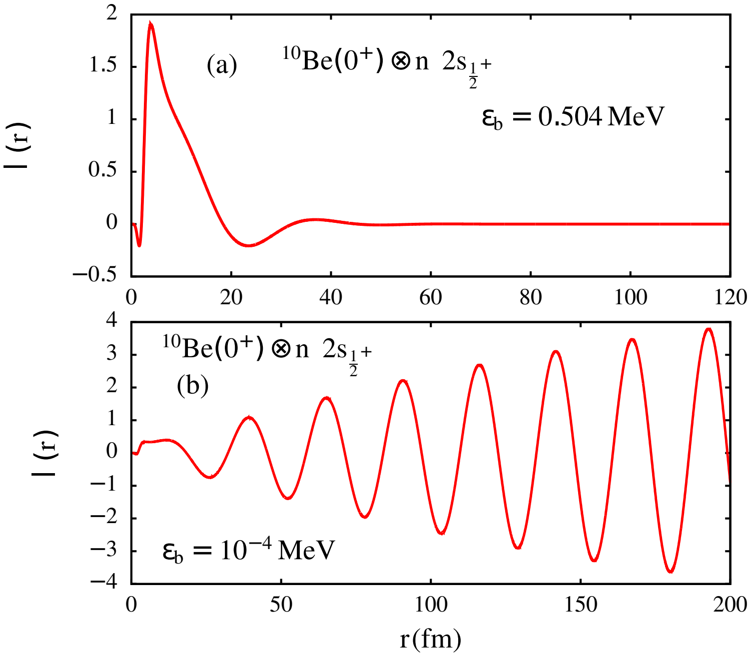

Figure 4.8: Integrand of the radial integral (2.106) for the ^{10}Be + n system, for $\varepsilon_b = 0.504\,\text{MeV}$ and $\varepsilon_b = 10^{-4}\,\text{MeV}$. The scattering wave function was calculated in the resonance partial wave ($\ell = 2, j = \frac{5}{2}^+$) at continuum energy of $\varepsilon = 1.3\,\text{MeV}$, which approximately equal to the resonance energy.

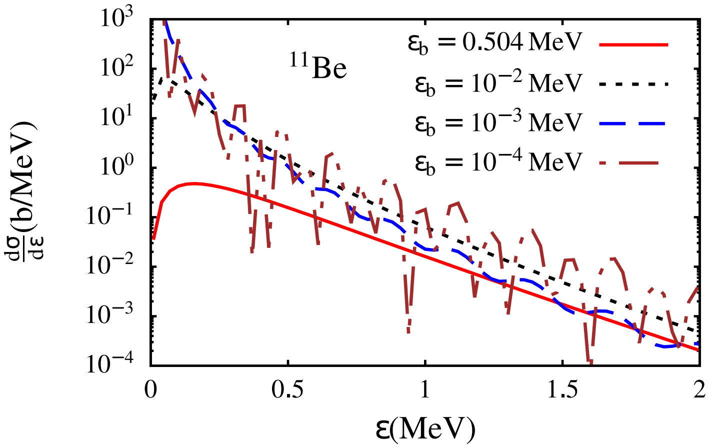

Figure 4.9: First-order Coulomb breakup cross section obtained through equation (2.103), as function of the projectile continuum energy ε.

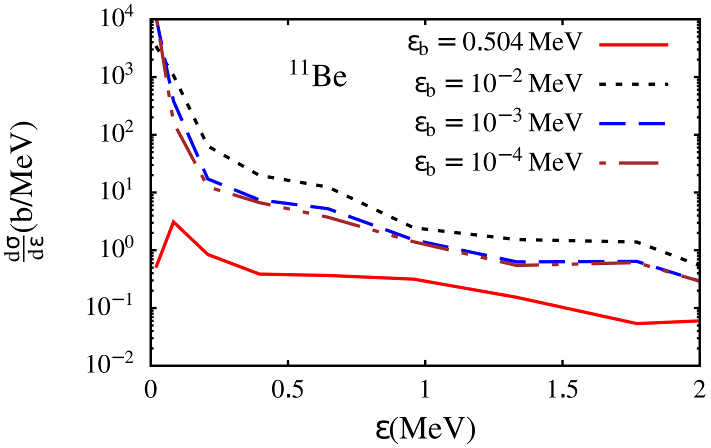

Figure 4.10: Breakup cross sections as functions of ^{11}Be continuum energy ε for different values of the ground-state binding energy ε_b.

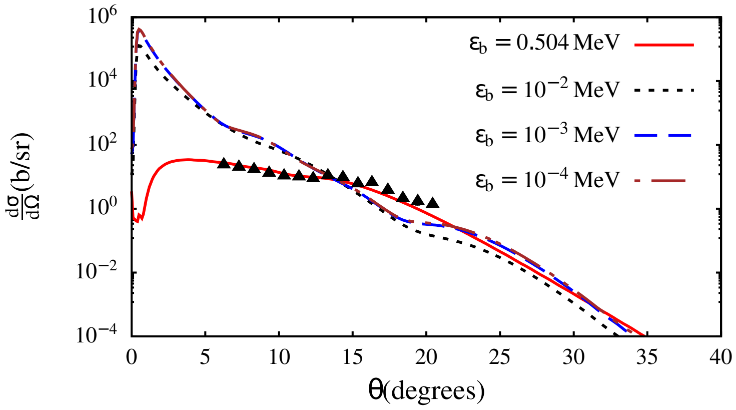

Figure 4.11: Angular distributions breakup cross sections corresponding to ^{11}Be projectile, for different values of the ground-state binding energy ε_b.

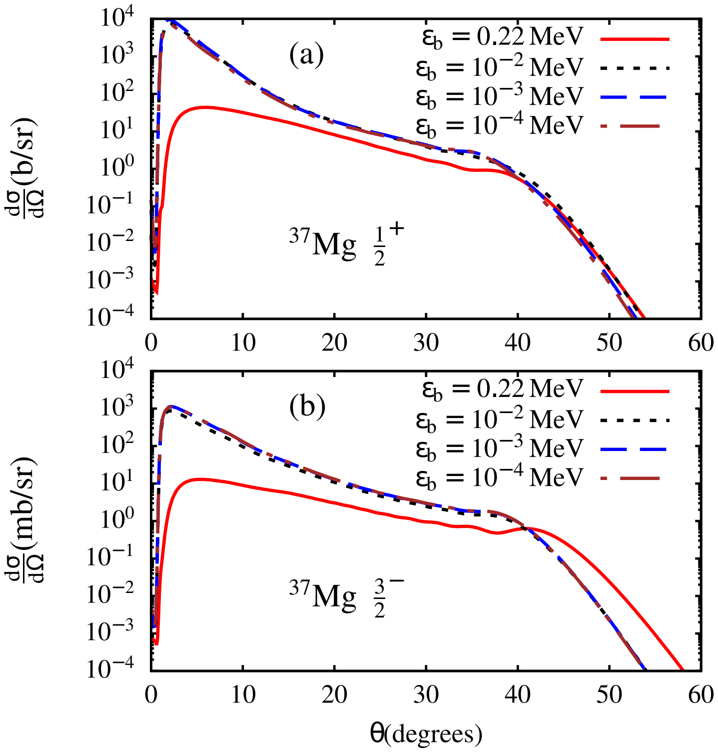

Figure 4.12: Angular distributions breakup cross sections corresponding to ^{37}Mg projectile, for different values of the ground-state binding energy ε_b.

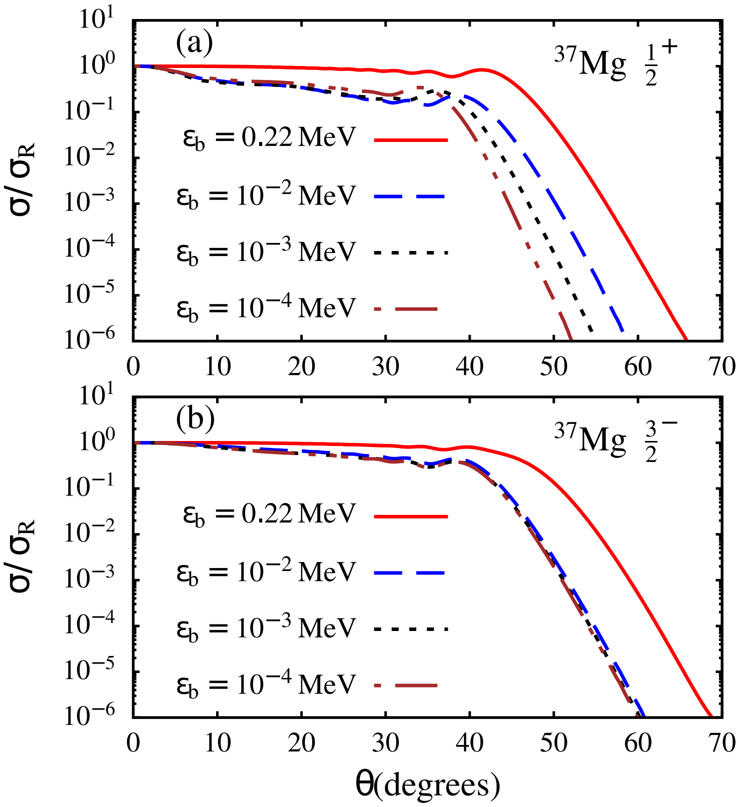

Figure 4.13: Elastic scattering cross sections corresponding to ^{37}Mg projectile, for s-wave configuration (a) and p-wave configuration (b), for different values of the ground-state binding energy ε_b.

Chapter 5

^{15}C breakup and the importance of the multi-step process

The results of the Coulomb and nuclear breakups of ^{15}C nucleus on heavy target at incident energy of E_{lab} =68 MeV/nucleon are analyzed in this chapter. The importance of the higher-order multipole transition and the continuum-continuum couplings effects on the nuclear and Coulomb breakups are reported. This reaction is regarded as dominated by the Coulomb breakup, due to the large charge of the target nucleus and the long-range nature of Coulomb forces. The main concern in this study is to check whether the two factors can justify the strong dominance of the Coulomb breakup over its nuclear counterparts. The same CDCC method described in chapter 2 and used in previous chapters, is utilized to determine the breakups of this reaction.

5.1 Description of a projectile

In the present work, we consider the following core-neutron s-wave ground-state configuration for the ^{15}C projectile $^{14}\mathrm{C} \otimes n(2s_{\frac{1}{2}^+})$ as suggested in Refs. [125, 126], where the valence neutron is loosely-bound to the ^{14}C core nucleus (which remains in its ground-state) by $\varepsilon_0 = 1.218\,\mathrm{MeV}$ binding energy [111]. Its first excited $\frac{5}{2}^+$ state has an excitation energy $\varepsilon_1 = 0.478\,\mathrm{MeV}$, and a resonance in $\frac{3}{2}^+$ partial-wave with a resonance energy of $\varepsilon_{res} = 3.56 \pm 0.1\,\mathrm{MeV}$ [127]. We identify the ground-state by $\alpha_0 \equiv (\varepsilon_0, \ell_0, s, j_0)$, [where $\ell_0 = 0$, is the angular momentum associated with the core-neutron relative motion, s, the neutron's spin, and j_0, the total angular momentum ($\boldsymbol{j}_0 = \boldsymbol{\ell}_0 + \boldsymbol{s}$)], and the scattering states by $\alpha \equiv (\varepsilon, \ell, s, j)$.

5.2 Results and Discussion

The description of the numerical calculations, i.e., the parameters of the different potentials and the parameters used in the solution of the coupled equations (2.65), are summarized in tables 2 and 3 of in Ref. [72], where the same reaction at the same incident energy is analyzed. We therefore, do not repeat the detail here. In figure 5.1, we show the dipole electric response function for the transition from the s-wave ground-state to the p-wave continuum state as function of the excitation energy, where we observe a satisfactory agreement with the experimental data taken from Ref. [107]. In figure 5.2, we show the first-order Coulomb breakup cross section as function of the projectile excitation energy, calculated using equation (2.110), at the projectile incident energy E_{lab} =68 MeV/nucleon, which corresponds to projectile velocity $v = 0.36c$ (c, being the speed of light in the vacuum). The theoretical calculations are compared with the experimental data taken from Ref. [107]. Observing this figure, one notices that the first set of data "data1" (full black triangles) is well fitted by the theoretical calculations performed with a cutoff angle $\theta_c = 6.23°$ (which corresponds to a minimum impact parameters of b_{min} =7.44 fm). The other set of data "data2"(open brown circles) is set fitted by the calculations performed with $\theta_c = 3.50°$ (corresponding to a minimum impact parameters of b_{min} =16.19 fm). The results corresponding to $\theta_c = 2.70°$ are included just to check

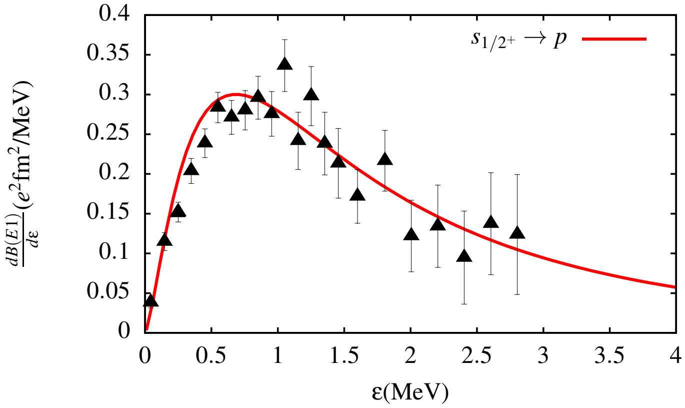

Figure 5.1: Dipole electric response function plotted as function of the excitation energy, for the transition from the s-wave ground-state to the p-wave continuum state, compared with the experimental data taken from Ref. [107].

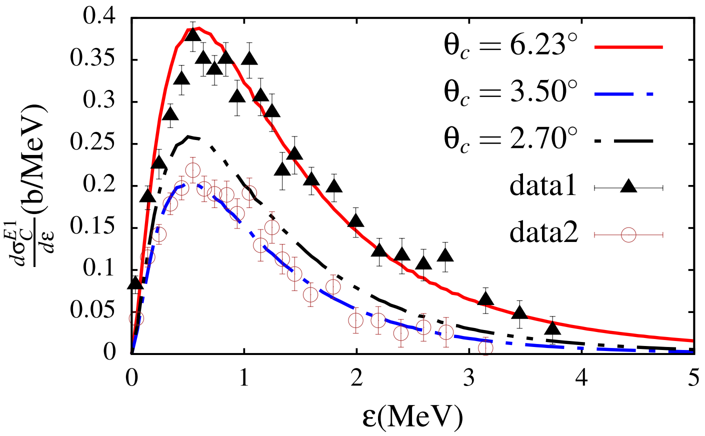

Figure 5.2: First-order Coulomb breakup cross sections, calculated using Eq.(2.103), for an incident energy of E_{lab} =68 MeV/nucleon, corresponding to a projectile velocity of $v = 0.36c$ (c, being the speed of light in the vacuum). The three angles correspond to minimum impact parameters b_{min} =7.44 fm, 12.41 fm and 16.19 fm. The theoretical calculations are compared with the experimental data from Ref. [107].

how the first-order Coulomb breakup cross section varies with θ_c. One sees that the angle θ_c plays a crucial role in the first-order approximation theory, and reveals to some extent the relevance of the nuclear breakup.

Let us now consider the CDCC calculations. In order to obtain the total, Coulomb and nuclear breakup cross sections, we numerically solved the coupled differential equations (2.65), the computer code Fresco [67]. The procedure adopted in obtaining the different breakup cross sections is outlined in Chapter 2, where the Coulomb breakup cross section is obtained by removing all the nuclear interactions in the coupling matrix elements. The nuclear breakup cross section is obtained by removing all the Coulomb interactions in the same coupling matrix elements. The total breakup cross section, is the coherent sum of Coulomb and nuclear breakup cross sections, obtained when Coulomb and nuclear forces are simultaneously included in the calculations. In figure 5.3, the total, Coulomb and nuclear breakup cross sections as functions of the projectile continuum energy are shown. We also show the case where the Coulomb breakup cross section is scaled by a factor of 0.69 is also shown. For comparison purpose, the first-order Coulomb breakup cross section of figure 5.2, is also included. The shown results were obtained at all-order transitions with all the different continuum-continuum couplings included in the coupling matrix elements. One notices in this figure that the total breakup cross section, provides a better fit of the experimental data “data1”, whereas the Coulomb breakup cross section

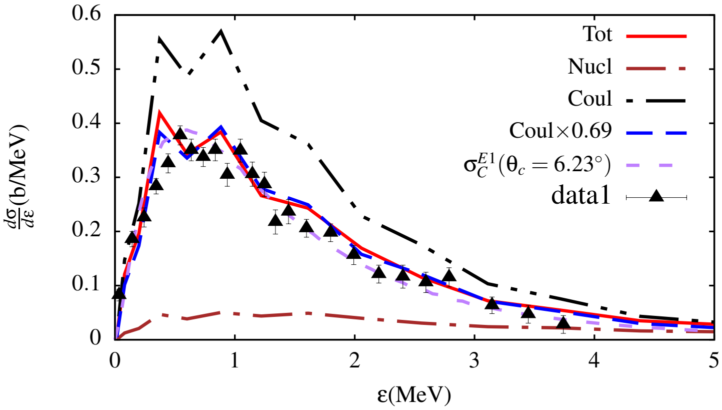

Figure 5.3: Differential total, Coulomb and nuclear breakup cross sections as functions of the projectile excitation energy ε, calculated by means of the CDCC formalism, at all order multipole transitions and when all the different couplings are included in the coupling matrix elements. The first-order Coulomb breakup cross section of Fig.5.2 is also included for comparison purpose. The results are compared with the experimental data which were taken from Ref. [107].

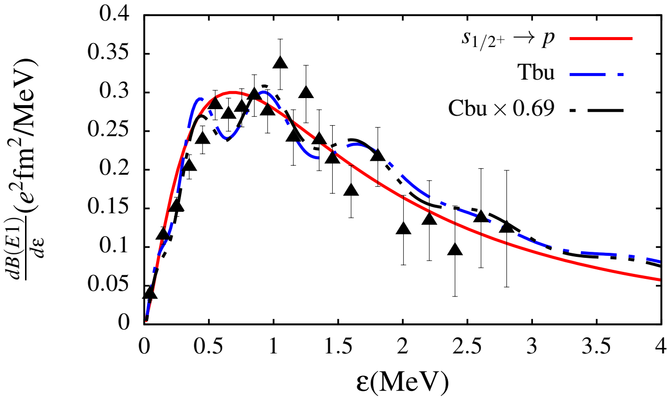

Figure 5.4: Electric response function as function of the excitation energy, obtained using Eq.(5.1). The dashed lines where obtained using the total ("Tbu") and Coulomb ("Cbu", scaled by a factor of 0.69) breakup cross sections calculated within the CDCC formalism. The experimental data were taken from Ref. [107].

largely overestimates the data, and is much larger than both the total and nuclear breakup cross sections. The fact that both total and first-order Coulomb breakup cross section provide as satisfactory fit of the experimental data, implies that both cross sections are in agreement. We observe that the Coulomb breakup cross section is nearly similar to the total breakup cross section when it is scaled by a factor of 0.69. We recall that in the calculations of the Coulomb breakup, the nuclear interaction is not included in the elastic scattering channel, such that the Coulomb breakup cross section is not affected by any there nuclear absorption which would reduce it. Therefore, the factor of 0.69 could

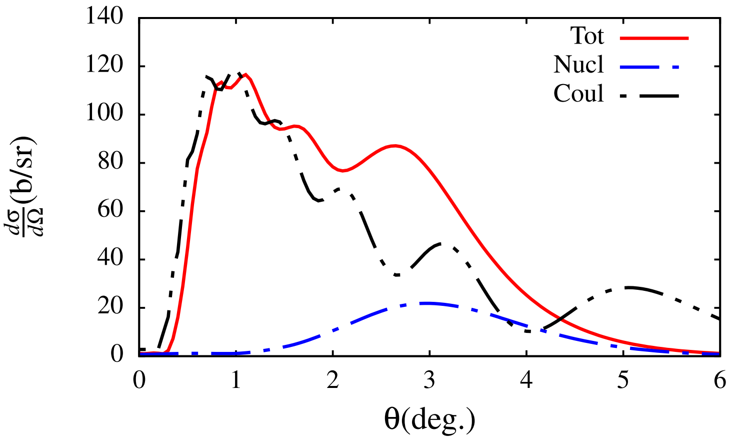

Figure 5.5: Angular distributions differential total,Coulomb and nuclear breakup cross sections as functions of the projectile-target centre-of-mass angle θ, calculated at all order multipole transitions and when all the different couplings are included in the coupling matrix elements.

emanate from the effect of the nuclear absorption and Coulomb-nuclear interference on the Coulomb breakup cross section. It would be interesting to investigate this aspect in a different study. The agreement of the experimental data with the total breakup cross section and the disagreement with the Coulomb breakup cross section, further emphasises the relevance of the nuclear breakup cross section even though it is rather small compared to the Coulomb breakup cross section. This serves to highlight the fact that small nuclear breakup contribution does not necessarily imply negligible Coulomb-nuclear interference effect.

The analytical expression (2.110), can be used in an indirect approach to obtain an information on the projectile structure from the breakup cross section data. Such procedure has been adopted in various works such as Refs. [75,107,128,129]. Once the dipole electric response is obtained from equation (2.110), other projectile properties such as root-mean-square radius, among others can be extracted from it. In terms of the Coulomb breakup cross section, the dipole electric response function is given by

$$\frac{dB(E1)}{d\varepsilon} = \frac{9}{32\pi^2}\left(\frac{\hbar v}{Z_t e}\right)^2 \frac{1}{z_m \mathcal{K}_0(z_m)\mathcal{K}_1(z_m)} \frac{d\sigma_C^{E1}}{d\varepsilon}. \tag{5.1}$$

We use this equation to obtain from the total and Coulomb (scaled by the factor 0.69) breakup cross sections of the CDCC formalism, the projectile dipole electric response function for the transition from the s-wave ground-state to the p-wave continuum state.

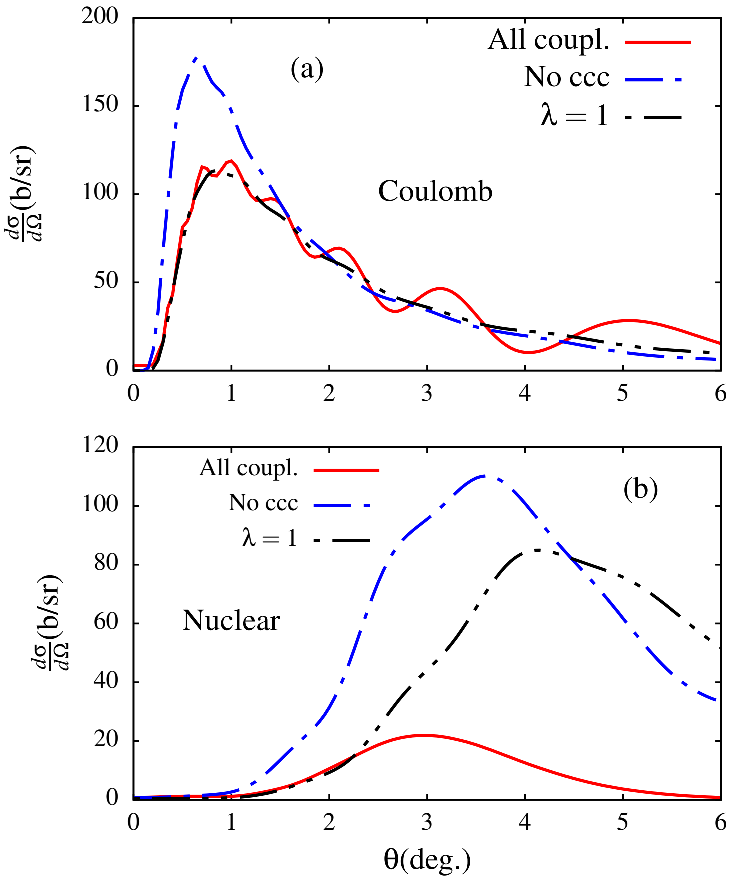

Figure 5.6: Angular distributions Coulomb and nuclear breakup cross sections as functions of the projectile-target centre-of-mass angle θ, calculated when: all the different couplings are included in the coupling matrix elements (“All coupl.’), all continuum-continuum couplings are excluded “No CCC”, and all different couplings are considered, but only for a single monopole transition ($\lambda = 1$).

The results are presented in figure 5.4, and compared with the experimental data. The dipole electric response function plotted in figure 5.1 is also shown to compare with. In this figure, “Tbu” stands for total breakup, and “Cbu” Coulomb breakup. As one would expect based on figure 5.3, the dipole electric response functions computed from equation (5.1), exhibit an oscillatory pattern that is consistent with the experimental data. We also observe a fair agreement with the result in figure 5.1, particularly a lower excitation energies.

So far, we have limited our discussion to the different breakup cross sections as functions of the projectile excitation energy ε, and when all the different couplings and all-order transition effects are included in the calculations. Before considering the effects of the continuum-continuum couplings and higher-order transitions on the different breakup

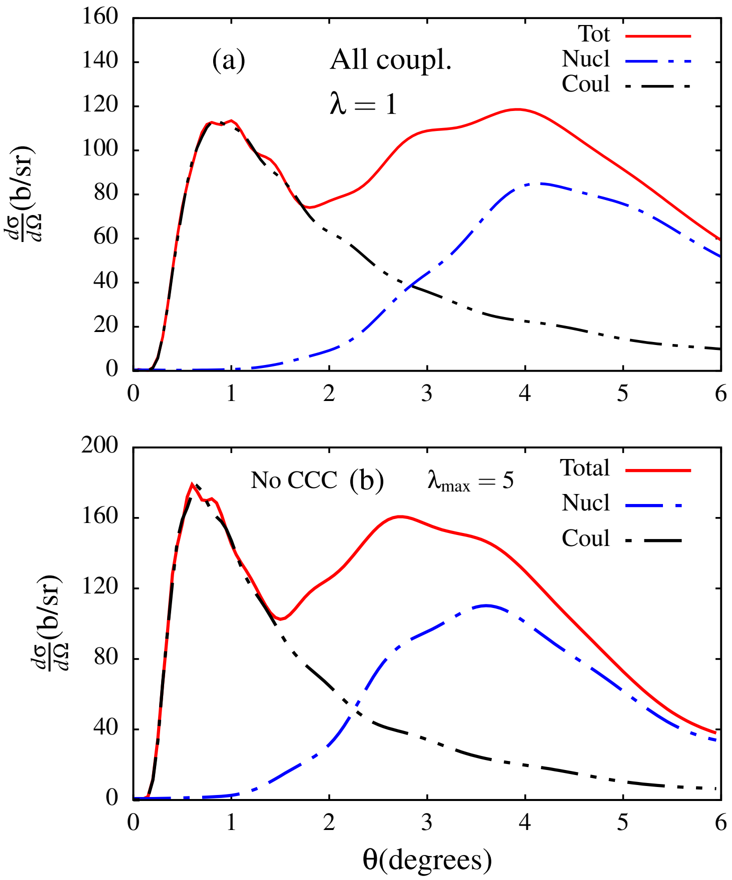

Figure 5.7: Total, Coulomb and nuclear breakup cross sections as functions of the projectile-target centre-of-mass angle θ, calculated when: all the different couplings are included in the coupling matrix elements, but for only a single multipole transition ($\lambda = 1$), and all continuum-continuum couplings are excluded "No CCC", with all the different multipole transitions included ($\lambda_{\max} = 5$).

cross sections, we present in figure 5.5, the total, Coulomb and nuclear breakup cross sections as functions of the center-of-mass angle θ, in order to get a glimpse on the dependence of the first-order Coulomb breakup cross section on the cutoff angle θ_c in figure 5.2. Contemplating this figure, one sees that the nuclear breakup cross section appears to exhibit a Gaussian distribution with a maximum around 3°, meaning that around this angle, the first-order Coulomb breakup should be minimum according to the first-order approximation theory, as observed in figure 5.2. The longer tail of the Coulomb breakup cross section at larger angles reflects the lack of nuclear absorption.

Finally, let us consider the higher-order multipole and continuum-continuum coupling effects. In order to assess the importance of higher-order multipole effect, we compare the results obtained with only the monopole multipole order ($\lambda = 1$), and those obtained with the full calculations ($\lambda_{\max} = 5$), which is the maximum multipole order considered in the multipole expansion of the potential $U_{pt}(\boldsymbol{r}, \boldsymbol{R})$. Likewise, we obtain the effect of the continuum-continuum couplings by comparing the results obtained when all the different couplings are included in the calculations with those obtained when the continuum-continuum couplings are removed. In figure 5.6, we plot the Coulomb breakup cross sections [panel (a)] obtained with full calculations, with only the monopole multipole order ($\lambda = 1$), but all different couplings are included, and with all order multipole transitions ($\lambda_{\max} = 5$), but the continuum-continuum couplings are removed. The nuclear breakup cross sections corresponding to the same calculations, are shown in panel (b). If we compare both panels, it resorts that the CCC and higher-order multipole transition effects are stronger on the nuclear breakup cross section than on the Coulomb breakup cross section. This figure displays the fact that the CCC and higher-order multipole transition effects are removed, the nuclear breakup cross section would be larger or comparable to its Coulomb counterpart, despite the larger target charge. This is well depicted in figure 5.7, where the total, Coulomb and nuclear breakup cross sections are plotted on the same panels, for the single monopole multipole transition ($\lambda = 1$) [panel (a)], and in the absence of the CCC [panel (b)]. We notice that at larger angles, the total and nuclear breakup cross sections are larger than the Coulomb breakup cross section. This amount to saying that a larger target charge alone cannot justify the larger magnitude of the Coulomb breakup cross section over the nuclear breakup cross section in a reaction involving a heavy target. Therefore, the concept *Coulomb-dominated reaction* might prove to be mainly relative to the prevailing reaction dynamics and not only a larger charge of the target nucleus.

In summary, we investigated the comparison of the total, Coulomb and nuclear breakup cross sections when all the different couplings are included or excluded in the coupling matrix elements in the reaction that involve heavy target. We found that our results are in agreement with the calculated data and the larger set of experimental data for $\theta_c = 6.23°$, whereas for the set of lower data, for $\theta_c = 2.70°$. It is shown that the Coulomb and nuclear has an effect on the reaction that involve the heavy target which is regarded as Coulomb-dominated, due to the large charge of the target nucleus and the long-range nature of Coulomb forces. We found that the continuum-continuum couplings and the higher-order multipole transitions have stronger effects on the nuclear breakup cross section compared to the Coulomb breakup cross section. In the following chapter, we investigated the angular distributions differential breakup cross section and the integrated breakup cross section when the resonant and non-resonant states are included or exclude in the coupling matrix elements.

Chapter 6

Strong continuum-continuum couplings between ^{6}Li resonant states

The effects of the resonant and non-resonant states on the breakup cross sections of $^6\text{Li} + {}^{209}\text{Bi}$ reaction is investigated in this chapter. The concern here is to find out if these states have an impact on the angular distributions differential breakup cross section and integrated breakup cross section when both states are included or excluded in the coupling matrix elements. And also when the continuum-continuum couplings are included or excluded for both resonant and non-resonant states. In order to understand better about these effects, the CDCC method is also used to perform the numerical calculations as indicated below.

6.1 Numerical calculations and Results

6.1.1 Projectile description and parameters of numerical calculations

We recall that the ^{6}Li projectile considered in this thesis, is modeled as alpha particles a core nucleus plus deuteron a valance nucleus $^6\text{Li} \to {}^4\text{He} + {}^2\text{H}$, with ground-state binding energy $\varepsilon_b = 1.47\,\text{MeV}$. The ^{6}Li ground-state is identified by $n = 2, \ell_0 = 0, s = 1, j_0^\pi = 1^+$ quantum numbers, where s is the deuteron spin, with $\boldsymbol{j}_0 = \boldsymbol{\ell}_0 + \boldsymbol{s}$, with $\boldsymbol{\ell}$ the orbital angular momentum, and $\boldsymbol{j}_0$ the total angular momentum of the system. This ^{6}Li nucleus has three resonances ($j^\pi = 1^+, 2^+, 3^+$) in the $\ell = 2$ continuum states. The resonances were obtained with the Woods-Saxon potentials in the energy range up to 11 MeV. The Woods-Saxon potentials were calculated with the RADCAP code program [130] which is designed to determined only the two-body system or to locate the resonance energy states. These potential parameters were calculated in equation (2.10) with $V_0 = -59.20\,\text{MeV}$, $R_0 = 2.09\,\text{fm}$ and $a_0 = 0.7\,\text{fm}$ and the spin-orbit coupling term (2.10) with $V_{so} = -2.50\,\text{MeVfm}^2$, $R_{so} = 2.9\,\text{fm}$ and $a_{so} = 0.7\,\text{fm}$ [131]. The resonances are obtained by adjusting the depth of the potentials. The resonance phase shifts are represented in figure 6.1. The resonance states ($f_{1^+}, f_{2^+}, f_{3^+}$) are observed at resonance energies $\varepsilon_{res} = 4.67\,\text{MeV}$, $\varepsilon_{res} = 3.09\,\text{MeV}$ and $\varepsilon_{res} = 0.73\,\text{MeV}$, respectively. The Coulomb potential is calculated as a point-charge in equation (2.12) with $R_C = 2.09\,\text{fm}$. The convergence are achieved with the following parameters calculated with the Fresco code [92] shown in Table 6.1.

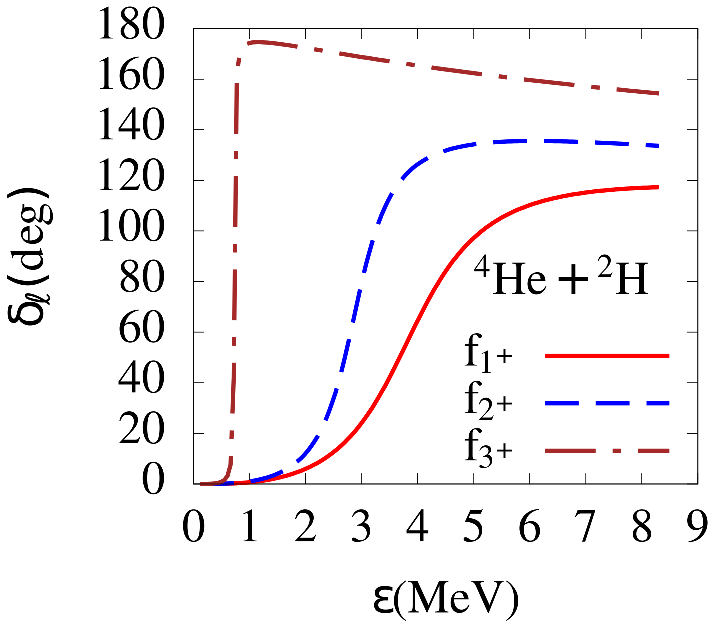

Figure 6.1: A schematic representation of the resonance phase shifts for the ^{6}Li → ^{4}He+^{2}H system.

These states are calculated with the different incident energies in the range of $23-40$ MeV and partial waves ℓ_{max} =0, 1, 2, 3, 4, 5 and 6. The convergence are obtained with the maximum excitation energy up to $\varepsilon_{max} = 8\,\text{MeV}$. The maximum excitation energies are discretized into energy bins with the Coulomb radius included $R_c = 1.25\,\text{fm}$.

Table 6.1: Core-target and fragment-target optical potential parameters were obtained from Ref. [132]

Syst.	V_0 (MeV)	r_0 (fm)	a_0 (fm)	W_V (MeV)	r_V (fm)	a_V (fm)
$^2\mathrm{H} + {}^{209}\mathrm{Bi}$	-100.2	1.150	0.973	-15.37	1.45	0.559
$^4\mathrm{He} + {}^{209}\mathrm{Bi}$	-107.4	1.361	0.578	-13.50	1.412	0.299

6.1.2 Radial integrals

In figure 6.2, we analyzed the radial integrals for the transitions from the ground state to $\ell = 2$ scattering states. We compare the resonance states observed in the continuum wave functions in figure 6.2 (a), figure 6.2 (b) and figure 6.2 (c). The observed peaks in figure 6.2 (a) and figure 6.2 (b) are rather oscillatory than clear peaks. There are clear peaks observed in the figure 6.2 (c) compare to figure 6.2 (a) and figure 6.2 (b). One can see a maximum peak in figure 6.2 (c) occurring at $r = 20\,\mathrm{fm}$. The minimum peak is also observed at $r = 90\,\mathrm{fm}$. The observed changes are due to the exponential decay of the different resonance states ($j^\pi = 1^+, 2^+, 3^+$). From this one can notice that resonance ($j^\pi = 3^+$) is more important than resonance ($j^\pi = 1^+, 2^+$).

6.1.3 Angular distributions differential breakup cross sections

In figure 6.3, we show the convergence of the angular distributions differential breakup cross section obtained when the resonant and non-resonant states are included in the coupling matrix elements. The convergence are achieved with the incident energies of $E_{cm} = 30.0, 32.0, 34.0$ and $40.0\,\mathrm{MeV}$ and the different partial waves up to ℓ_{max} =0, 1, 2, 3, 4, 5 and 6. From this figure it can be seen that the differential breakup cross sections are hardly distinguishable for the maximum partial waves from ℓ_{max} =2 to 6. The results demonstrates the good convergence at ℓ_{max} =2, 3, 4, 5 and 6. The partial wave ℓ_{max} =2 is more dominant compare to other partial waves ℓ_{max} =0 and 1. This is due to the fact that the partial wave ℓ_{max} =2 contains both resonant and non-resonant states. One can concluded that the resonance states has an effects on the breakup cross sections. In figure 6.4, we presents the angular distributions differential breakup cross section, obtained when the resonant and non-resonant states are included in the coupling matrix elements. One can notice a strong dominant of resonant state for lower energies $E_{cm} = 30.0, 33.0$, and 34.0 MeV compare to non-resonant state for high energies $E_{cm} = 36.0, 38.0$, and 40.0 MeV. All and Sum are dominant for all energies. But All is strongly dominant than Sum for all energies. The resonant and Sum are more important for lower energies at backward angles ($80° \leq \theta \geq 140°$). These results provides confirmation about the effects of resonant and non-resonant states on the breakup cross sections.

6.1.4 Integrated breakup cross sections

Furthermore, we discuss this effects in more details. Figure 6.5 (a) reports the integrated breakup cross section obtained when both the resonant and non-resonant states are include in the coupling matrix elements, whereas figure 6.5 (b) represents the results when the continuum-continuum couplings are excluded for both resonant and non-resonant states. Our results are in agreement with the experimental data obtained from Ref. [133], as this is seen with the dot line and the Full integrated breakup cross sections in figure 6.5 (a). The integrated breakup cross section in meth2 is more important at incident energy below 35 MeV compare to meth1. They are hardly distinguishable above the incident energy 38 MeV. The integrated breakup cross sections increases as the incident energies increases as shown in figure 6.5 (b). The non-resonant integrated breakup cross section is prominent compare to resonant integrated breakup cross section. The Full integrated breakup cross section and non-resonant breakup cross sections are hardly distinguish. This indicates good convergence. From this we observed that non-resonant integrated breakup cross section is dominant when the coupling matrix elements are included or when the continuum-continuum coupling are excluded. Further analysis will be done to investigate in more detail the resonances effects (see figure 6.6). From this figure it can be seen that the ratio of the non-resonant integrated breakup cross section is dominant throughout the spectrum, whereas the resonant integrated breakup cross section is slightly important at incident energy between 25 MeV and 30 MeV. The full integrated breakup cross section is dominant at the incident energy below 25 MeV compare to resonant integrated breakup cross sections. They contributes equally at incident energy 27 MeV and 34 MeV.

In summary, we studied the effects of resonant and non-resonant states on the angular distributions differential breakup cross section and the integrated breakup cross section when the coupling matrix elements are included or excluded. We shown that the angular distributions differential breakup cross section obtained when the resonant and non-resonant states are included in the coupling matrix elements convergences. It is also found that resonant states are strongly dominant for lower energies whereas non-resonant states dominate for higher energies. The calculated data are in agreement with the experimental data for the integrated breakup cross section obtained when both the resonant and non-resonant states are included in the coupling matrix elements. In the following chapter, we analyzed the effect of the Helium-dimer continuum-continuum couplings on the elastic and dissociation cross sections in the $^4\mathrm{He}_2 + {}^4\mathrm{He} \rightarrow {}^4\mathrm{He} + {}^4\mathrm{He} + {}^4\mathrm{He}$ reaction.

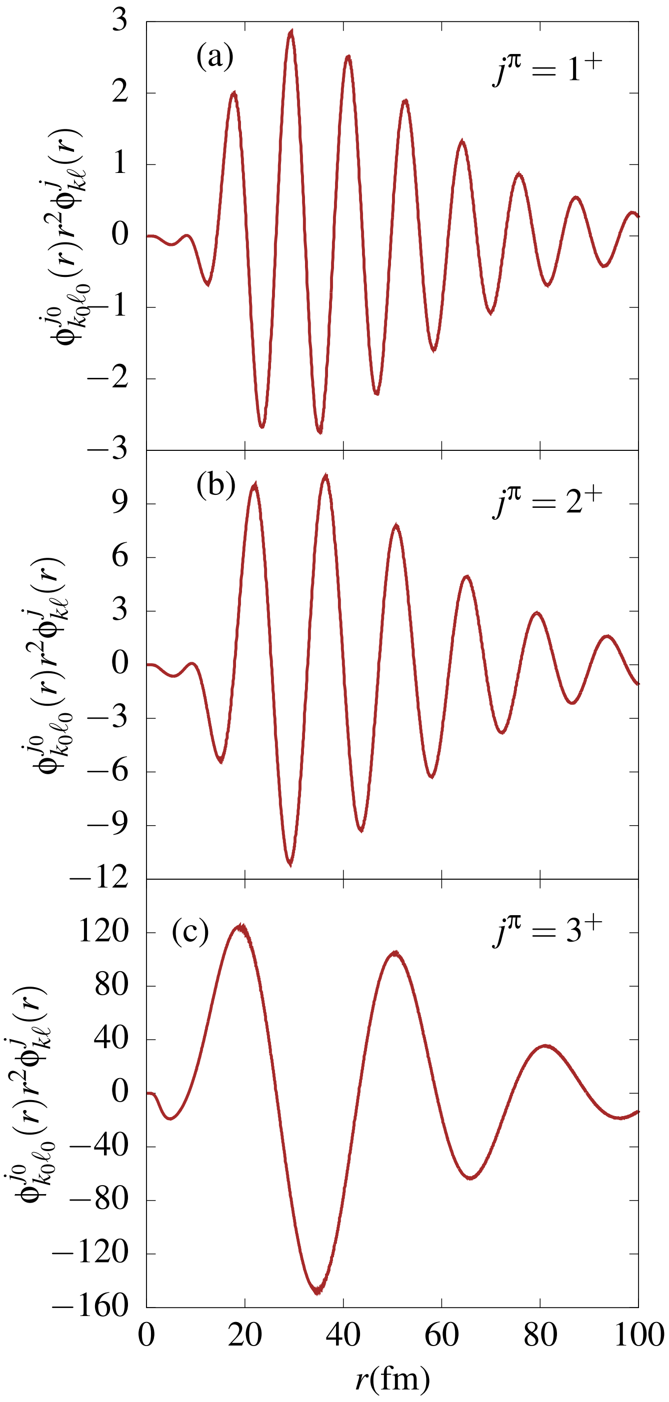

Figure 6.2: The radial integrals for the transitions from the ground state to $\ell = 2$ scattering states.

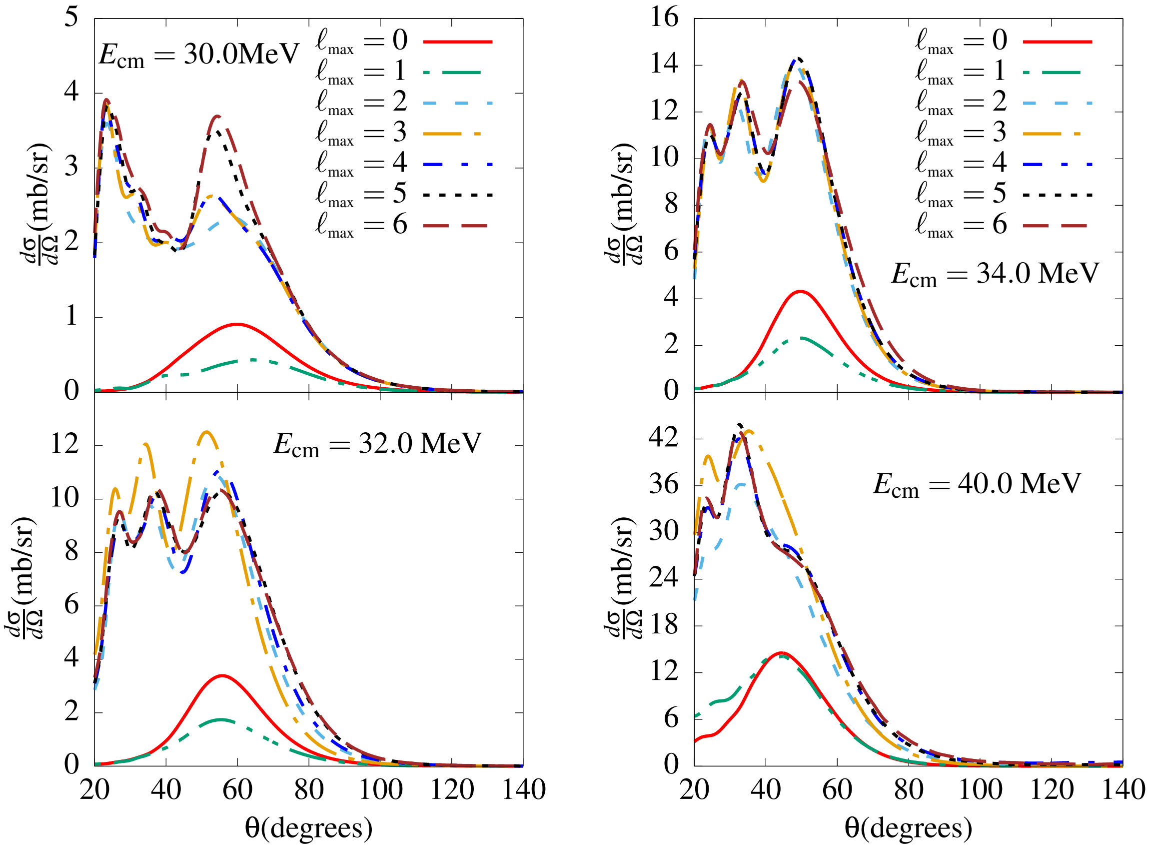

Figure 6.3: Convergence of the angular distributions differential breakup cross section, obtained when resonant and non-resonant stated are included in the coupling matrix elements.

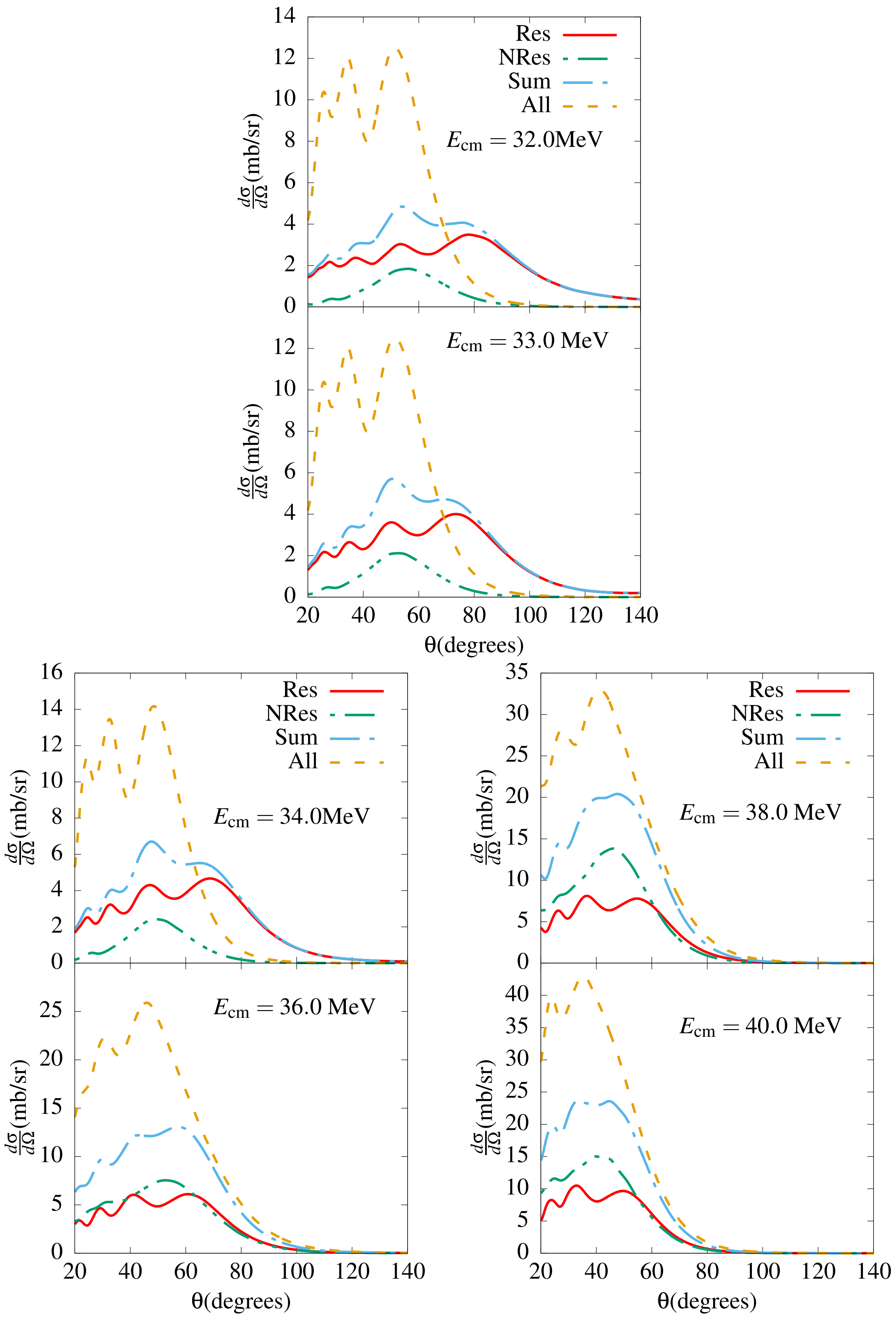

Figure 6.4: The angular distributions differential breakup cross section, obtained when the resonant and non-resonant states are included in the coupling matrix elements.

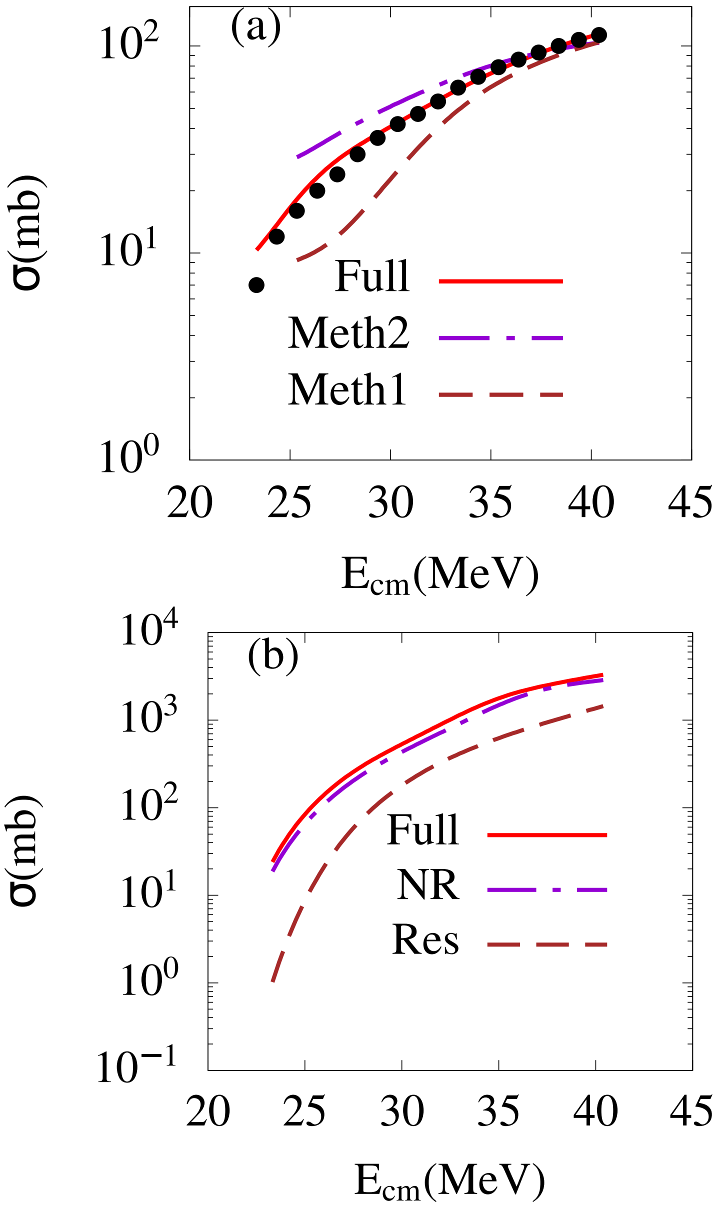

Figure 6.5: Integrated breakup cross section, obtained when (a) the resonant and non-resonant states are included in the coupling matrix elements (b) the continuum-continuum couplings are exclude for both resonant and non-resonant states.

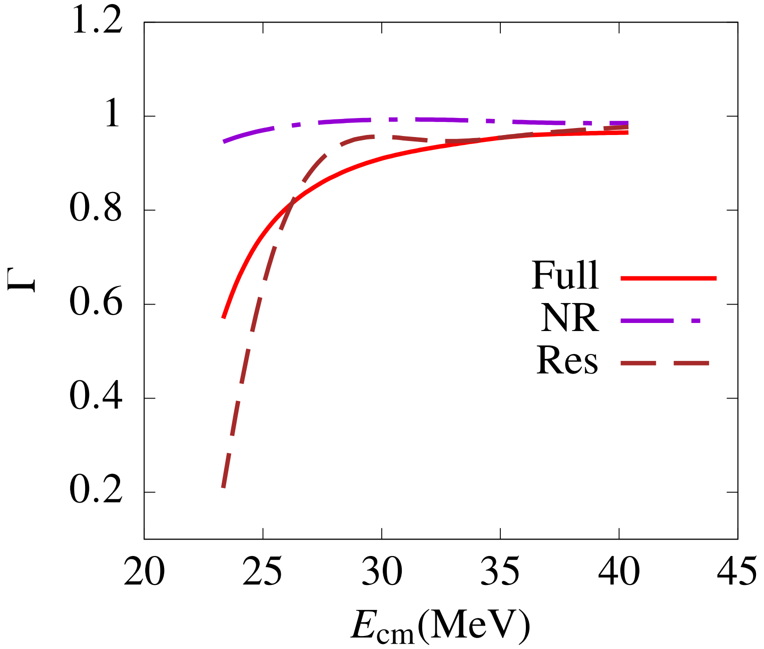

Figure 6.6: The ratio of the non-resonant and resonant integrated breakup cross sections obtained when the continuum-continuum coupling are excluded or included in the coupling matrix elements.

Chapter 7

Breakup dynamics of Helium dimer

In this chapter, the $^4\mathrm{He}_2 + {}^4\mathrm{He} \to {}^4\mathrm{He} + {}^4\mathrm{He} + {}^4\mathrm{He}$ dissociation reaction of Helium-dimer continuum-continuum couplings on the elastic and dissociation cross sections are analyzed using the CDCC method. Our concern here is to check the importance of the continuum-continuum couplings and the higher-order multipole transitions in the breakup of a weakly-bound atomic system. One would expect couplings among continuum states to play an important role in this reaction. And also to find out if the breakup process affects the elastic scattering cross sections. In order to understand the breakup dynamics of a weakly-bound atomic reaction. We start with the detail of the numerical calculations.

7.1 Details of numerical calculations

In this present study, we consider the breakup of Helium dimer on a Helium target, the so-called Helium trimer as shown in figure 7.1. This figure shows the projectile-target spacial configuration, where particles 1, 2 and 3 are Helium atoms, with particles 2 and 3 forming the Helium-dimer (He_2) projectile. $\boldsymbol{R}$ is the projectile-target relative coordinates as discussed in chapter 2, where $\boldsymbol{R}_{13} = \boldsymbol{R} + \frac{1}{2}\boldsymbol{r}$, and $\boldsymbol{R}_{12} = \boldsymbol{R} - \frac{1}{2}\boldsymbol{r}$, with $\boldsymbol{r}$ the internal projectile coordinates. In order to numerically solve the coupled differential equations (2.65), the dimer ground-and scattering wave functions are needed. The Helium-dimer ground-state is identified as an s-state, with $\ell_b = 0$, and $j_b^\pi = 0^+$ quantum number, with a binding energy $\varepsilon_b = 1.31\,\mathrm{mK}$ [134, 135]. To calculate the bound and scattering wave functions, we used two different potentials, two Helium-Helium soft core potentials

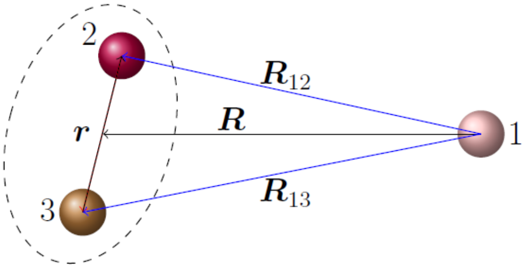

Figure 7.1: Illustration of the relative position vectors describing a Helium-Trimer system.

$[V_{23}(r)]$, namely an exponential one and a Gaussian soft core potential, given by equation (7.1)

$$\begin{aligned} V_{23}(r) &= v_1 e^{-r/R_1} \\ V_{23}(r) &= v_2 e^{-r^2/R_2^2}, \end{aligned} \tag{7.1}$$

where $v_1 = -3.909\,\mathrm{K}$, $R_1 = 2.179\,\text{Å}$. and $v_2 = -1.227\,\mathrm{K}$, $R_2 = 5.308\,\text{Å}$, taken from Ref. [136]. These two potentials are plotted in figure 7.2, where we notice that they both vanish for $r \geq 10\,\text{Å}$. For the numerical solution of the coupled equations (2.65), the dimer orbital angular momentum was truncated by $\ell_{\max} = 4$, the dimer-Helium potential was expanded into multipole order up to $\lambda_{\max} = 4$, the maximum matching radius for bin potential integration was truncated by $r_{\max} = 800\,\text{Å}$. The maximum matching radius in the numerical integration of the coupled differential equations was truncated by $R_{\max} = 1000\,\text{Å}$, the maximum angular momentum of the relative center-of-mass motion, by $L_{\max} = 10$. The continuous dimer momentum k, was truncated by $k_{\max}$, with the condition that $\hbar^2 k_{\max}^2/2\mu_{23} < E_{\text{c.m.}}$. The $[0 : k_{\max}]$ interval was then sliced into 10 equally spaced bins in each dimer partial-wave. The numerical calculations are carried out using Fresco [67].

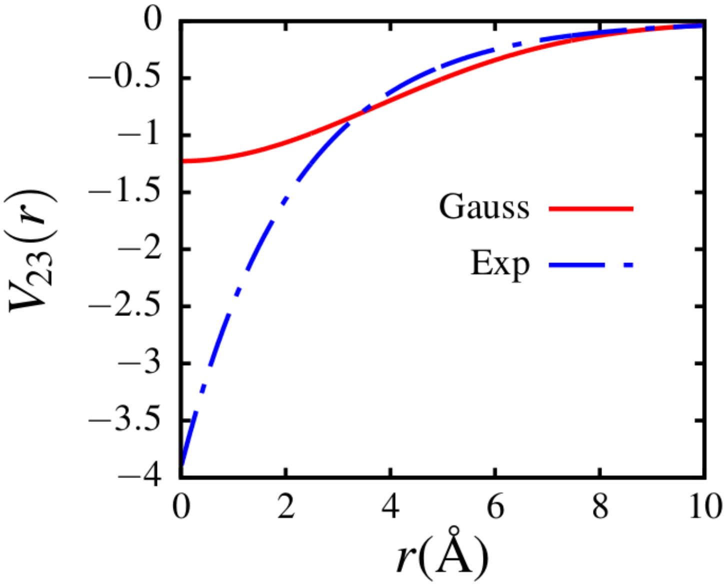

Figure 7.2: Helium dimer soft core Gaussian and exponential potentials.

7.2 Results and Discussion

The elastic scattering phase shifts are shown in figure 7.3, for Gaussian potential [panels (a) and (b)] and for the exponential potential [panels (c) and (d)]. This figure shows the results obtained when the dimer continuum among continuum states are removed from the coupling matrix elements ("No CCC"), and when all the different couplings are considered ("All coupl."). A closer look at this figure shows that the phase shifts obtained in the absence of the continuum-continuum couplings are in agreement with those obtained in Refs. [137, 138], with the same Gaussian potential. The positive phase shifts obtained with the exponential potential [panel (c)] can be attributed to the fact that this potential is more attractive compared to the Gaussian one (see figure 7.2). Positive phase shifts are also obtained with the hard core LM2M2 potential (see more information in Appendix A), for the same reaction (see for example [139]). Notice that the approaches used in Refs. [60, 140–144], correspond to single step transition from the ground-state to the continuum, which correspond to the CDCC calculations in the absence of the continuum-continuum couplings. The effect of these couplings is plainly clear in panels (b) and (d). For example, when these couplings are included, we obtained that at $E_{c.m.} = 1\,\text{mK}$, the phase shift is deviated from $-60°$ to $-11°$ for the Gaussian potential, and from 90° to

-14° for the exponential potential. We also notice that when these couplings are included, the phase shift has a weak dependence on the dimer potential.

In figure 7.4, we show the breakup (dissociation) cross section. In the present case, the breakup process $^4\mathrm{He}_2 + {}^4\mathrm{He}$, where all three Helium atoms are in the continuum. We observe in this figure that the breakup cross section is negligible at $E_{c.m.} \leq 4\,\mathrm{mK}$ incident energy. This would imply that for incident energies around 4 mK, the breakup cross section would already be significant given the fact that this energy is well above the dimer breakup threshold. However, this energy remains way below the trimer breakup threshold, which is about 120 mK. Therefore, these results may suggest that at $E_{c.m.} \leq 4\,\mathrm{mK}$ incident energies, this reaction is still dominated by atom recombination. This indicates that the probability that all three atoms are already freely flying in the continuum at $E_{c.m.} \leq 4\,\mathrm{mK}$, is quite negligible, hence a negligible dissociation cross section. Another interesting aspect in this figure is the appearance of a relative minimum around 8 mK. This minimum has been also observed in the dissociation probability, as in Refs. [18, 145–148], of this reaction. Now concerning the relevance of the continuum-continuum couplings, we notice that their effect is mainly quantitative and serve to reduce the breakup cross section. The suppression of the breakup cross sections owing to these couplings is a well-known feature of these couplings in nuclear reactions induced by loosely-bound projectiles, as shown for example in Refs. [43–46, 149]. It is interesting to find that this feature also extends to loosely-bound atomic systems. The elastic scattering cross sections are shown in figure 7.5, obtained in the absence of the continuum-continuum couplings and when all the different couplings are included in the coupling matrix elements.

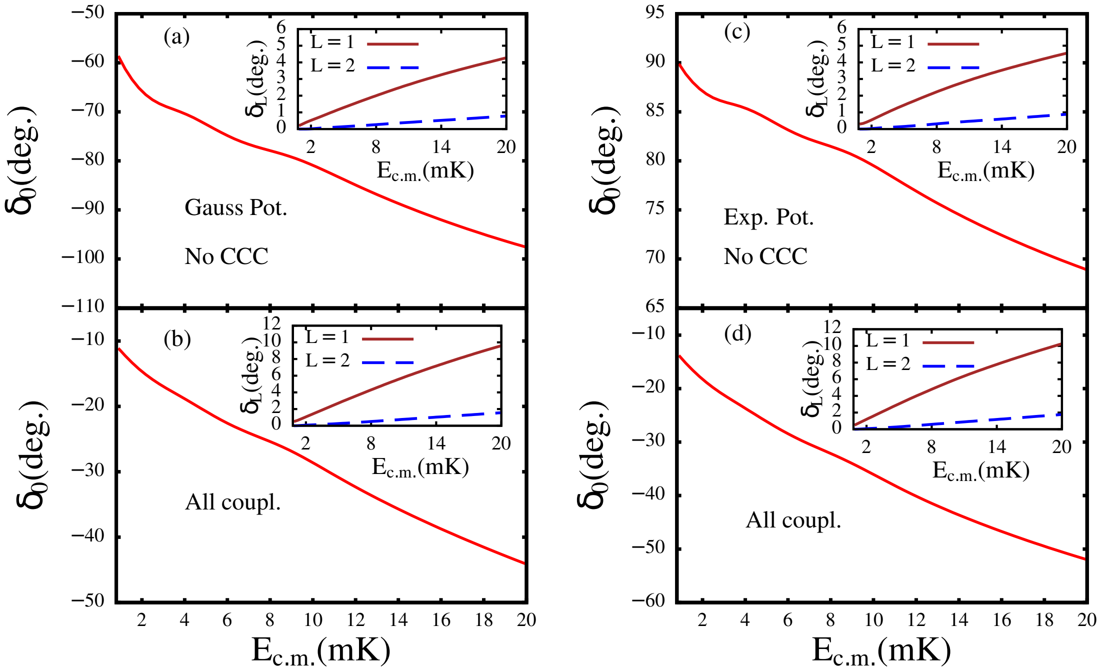

Figure 7.3: Elastic scattering phase shifts for $L = 0$, obtained with the Gaussian potential. “No CCC” stands for the calculations in the absence of the continuum-continuum couplings, and “All coupl.” represents the calculations performed when all the different couplings are included in the coupling matrix elements.

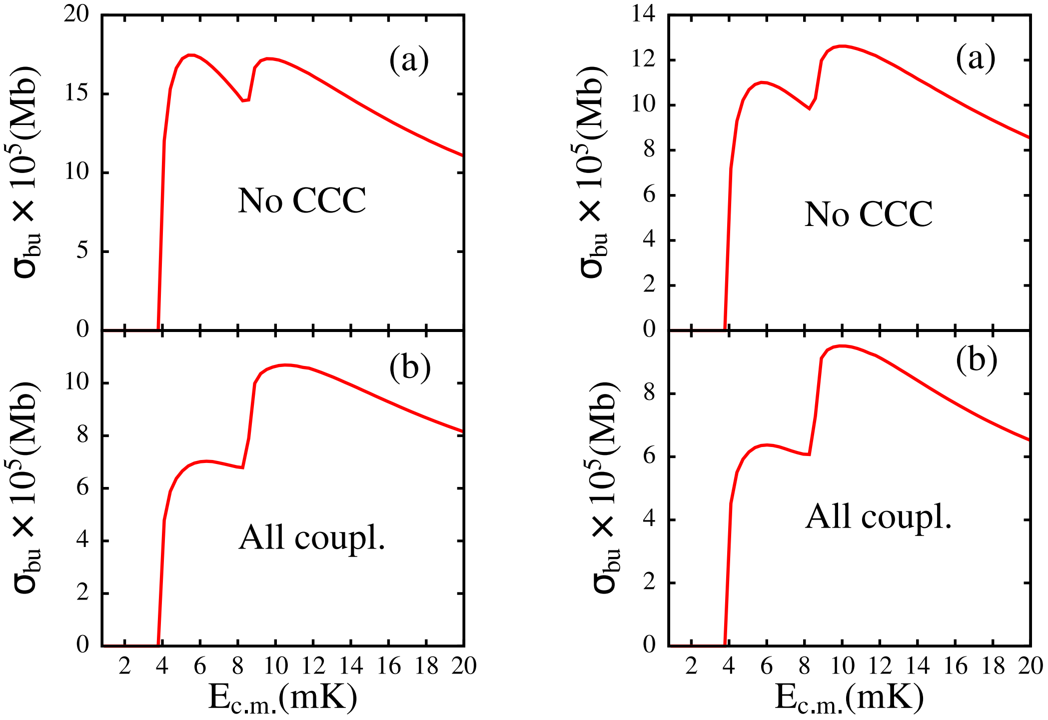

Figure 7.4: Breakup (dissociation) cross sections, obtained with the Gaussian potential. “No CCC” stands for the calculations in the absence of the continuum-continuum couplings, and “All coupl.” represents the calculations performed when all the different couplings are included in the coupling matrix elements.

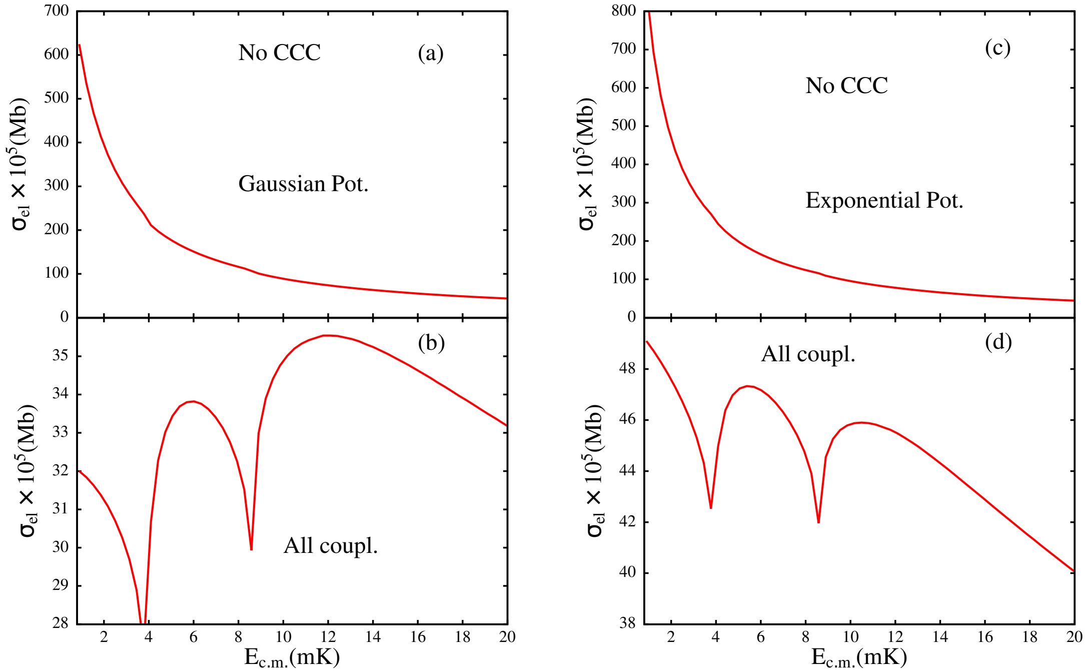

Figure 7.5: Elastic scattering cross sections, obtained with the Gaussian potential. "No CCC" stands for the calculations in the absence of the continuum-continuum couplings, and "All coupl." represents the calculations performed when all the different couplings are included in the coupling matrix elements.

Chapter 8

Concluding remarks and Future perspectives

8.1 Concluding remarks

We studied the breakup dynamics of the ^{8}B+^{208}Pb, ^{11}Be+^{64}Zn, ^{11}Be+^{208}Pb, ^{37}Mg+^{208}Pb, ^{15}C+^{208}Pb, ^{6}Li+^{209}Bi, and ^{4}He$_2$+^{4}He reactions with the use of the continuum discretized coupled channels (CDCC) method. For the ^{8}B + ^{208}Pb reaction, we investigated the effect of the continuum-continuum couplings on the complete fusion and breakup cross sections at deep sub-barrier, around, and above the incident energies. It is found that when the continuum-continuum couplings are included in the coupling matrix elements enhanced the breakup cross section at deep sub-barrier energies. In this case, for a large projectile binding energy becomes strongly enhanced. It is shown that in the absorption region the enhancement occurs. This enhancement is related to the outgoing trajectory of the breakup projectile due to the continuum-continuum couplings. To this end, we compared the total fusion cross section, breakup cross section, and reaction cross section.

It is observed that the breakup cross section accounts for about 92% of the total reaction cross section. This result confirms the conclusion that was made in Ref. [68]. From this, we conclude that at deep sub-barrier energies the breakup cross section is enhanced, whereas at energies above the barrier is suppressed. This will elucidate the breakup channel predominance at deep sub-barrier energies. It is found that the total fusion cross section is negligible when compared to the total reaction and breakup cross sections. We demonstrated that the measurement of a total fusion for ^{8}B + ^{208}Pb reaction may be performed at deep sub-barrier incident energies. As suggested in Ref. [68] which could be an important measurement from an astrophysics perspective. The complete fusion cross section due to the effect of the continuum-continuum couplings is also analyzed in this study. It is found that at sub-barrier energies the complete fusion cross sections is enhanced and at above-barrier energies is suppressed due to the continuum-continuum couplings. As it has been reported in various studies, we assert that not only couplings amount resonant states and any couplings among continuum states would procedure a complete fusion suppression. We conclude that at deep sub-barrier incident energies these continuum-continuum couplings can play a crucial role in the breakup process. The results of these continuum-continuum couplings can reveal an important effect on nuclear astrophysical quantities of interest. It would be of great interest to study further in this direction.

We investigated the breakup dynamics of an open neutron-halo reaction in the binding energy limit ($\varepsilon_b \to 0$) for the ^{11}Be + ^{64}Zn reaction. The linearity ground-state wave function in the asymptotic region is the characteristic of an open quantum system with $\varepsilon_b \to 0$, where ε_b is the ground-state binding energy. A lack of the breakup observables convergence of such systems would be naively expected owing to a linear ground-state wave function. In this study, the main goal was to show that, despite the linearity of the ground-state wave function, converged breakup cross sections can still be obtained. This is mainly due to the orthogonality of the continuum bin wave functions. To this end, we considered the breakup of an open two-body neutron halo system. Since such system is not yet available, in this work we considered the breakup of the well-known two-body neutron-halo system ^{11}Be on a ^{64}Zn target, where apart from its experimental ground-state binding energy ($\varepsilon_b = 0.504\,\mathrm{MeV}$). We arbitrarily selected four other values, $\varepsilon_b = 0.10\,\mathrm{MeV}$, $10.0\,\mathrm{keV}$, $0.10\,\mathrm{keV}$, and $0.01\,\mathrm{keV}$, obtained by adjusting the depth of the $^{10}\mathrm{Be} + n$ interaction. It is found that for $\varepsilon_b \leq 0.10\,\mathrm{keV}$, the $^{10}\mathrm{Be} + n$ ground-state wave function converges to a nonzero constant, outside the core nucleus radius, confirming its linearity. It is first shown that this low binding energy corresponds to a linear ^{11}Be ground-state wave function, outside of the core nucleus.

Due to the linearity of the ground-state wave function it is found that the elastic scattering cross section fails to converge as $\varepsilon_b \to 0$. This implies that the elastic scattering cross section convergence cannot be obtained in the scattering of an open neutron-halo system. However, the convergence of the breakup cross section is achieved, albeit at larger radial distances. We argue that this mainly comes from the orthogonality of the bin wave functions. It is shown that the ground-state wave function becomes nearly insensitive to the variation of the ground-state binding energy in the $\varepsilon_b \to 0$. As a result, the breakup observables such as total fusion cross section, breakup cross section, and reaction cross section are also reported to become almost independent of the ground-state binding energy in this limit. The convergence in this limit ($\varepsilon_b \to 0$), is a rather important finding that can be interesting for further investigations from experimental perspective. This study, which to the best of our knowledge presents the first attempt in this direction, can serve as a basis to analyze future experimental data for extremely loosely-bound systems.

The breakups of ^{11}Be and ^{37}Mg neutron halo nuclei on a ^{208}Pb target in the zero binding energy limit were investigated for both $^{11}\mathrm{Be} + {}^{208}\mathrm{Pb}$ and $^{36}\mathrm{Mg} + {}^{208}\mathrm{Pb}$ reactions. In the reaction of ^{37}Mg projectile on a ^{208}Pb target, it is found that the ground state density extends to infinity in the zero binding energy for an s-wave neutron halo system, whereas the ground state centrifugal barrier prevents the extension to infinity of the ground state density for p-wave. The same trend is observed for the ^{11}Be projectile. Due to the zero binding energy limit where the density becomes unbound for s-wave neutron halo systems, the matrix elements will not converge. For p-wave neutron halo system is found that the elastic scattering cross section converges as it becomes fairly independent of the variations of the binding energy zero limit. This is due to the ground state density that appears to remain finite even as $\varepsilon_0 \to 0$. It is also observed that the breakup cross section becomes insensitive to the variation of the binding energy $\varepsilon_b \leq 10^{-3}\,\mathrm{MeV}$, and $\varepsilon_b \leq 10^{-2}\,\mathrm{MeV}$, for both ^{208}Pb and ^{37}Mg projectiles. These results confirm those observed in earlier studies in Refs. [65, 66], for different reactions with non-zero ground state orbital angular momentum.

Due to the natural asymptotic behavior of the ground state wave function, the integrand quickly converges to zero for $r \leq 20\,\mathrm{fm}$ in the reaction of ^{11}Be nucleus on a ^{208}Pb target. It is shown that the ground state wave function is unbound, the integrand behaves as a scattering wave function. As a result the radial integral will not converge. Consequently, the first-order Coulomb breakup cross section will highly oscillate and can not converge in the zero binding energy limit. The radial integral, converges when the pure scattering wave functions are replaced by the square-integral bin wave functions. We have shown that the first-order theory can not handle the breakup of a system whose ground state wave function becomes unbound. On the other hand, we observed that in the CDCC calculations, the breakup matrix elements have no converges issue for the projectile pure scattering wave functions. It is found that there are no oscillations in the cross section even for $\varepsilon_b = 10^{-4}$ MeV, which reflects a smoother convergence of the radial integral. It is also noticed that the cross section converges to a finite value as $\varepsilon_0 \to 0$. We believe that these results are important in the analysis of future experimental data for extremely weakly-bound neutron halo systems.

In this study, we are interested to investigated the importance of the higher-order multipole transition and the continuum-continuum couplings effects on the nuclear and Coulomb breakups of the ^{15}C nucleus on heavy target at incident energy of $E_{lab} = 68$ MeV/nucleon. The purpose is to investigate whether the large target charge alone can justify the importance of the Coulomb breakup over its nuclear counterpart. The continuum-discretized coupled channels (CDCC) and the first-order approximation approaches were used to determine the effects of the Coulomb and nuclear breakup cross sections. In order to make the comparison of the Coulomb and nuclear breakup cross sections. For the Coulomb breakups, all nuclear interactions are removed from the coupling matrix elements. In the case of the nuclear breakups, the nuclear cross section is obtained when all the Coulomb potential is removed from these matrix elements, except the bare Coulomb potential in the projectile-target centre-of-mass. The Total, Coulomb and nuclear breakup cross sections are also performed when all the different couplings are included and excluded in the coupling matrix elements. It is observed that for $\theta_c = 6.23°$, the calculations are in agreement with the larger set of experimental data, while for $\theta_c = 2.70°$, are in agreement for the set of lower data. The maximum cutoff angle θ_c represents the Coulomb breakup which is dominant over its nuclear counterpart. In this case the nuclear breakup is not negligible. From this, it is observed that the nuclear breakup cross section peaks around $\theta = 3°$ and extends to $\theta = 6°$. As results, it is shown that the values $\theta_c = 2.70°$ and $\theta_c = 3.50°$, are located in the region where the nuclear breakup cross section is more significant. This study has found that the breakup cross section corresponding to $\theta = 6.23°$

is larger due to a negligible nuclear breakup at this angle. These findings demonstrate that the Coulomb and nuclear breakups have an impact in the reaction that involve the heavy target which is regarded as Coulomb-dominated.

The Coulomb breakup cross section is regarded as Coulomb-dominated in this reaction, due to the large target nucleus. In this regards, the Coulomb breakup cross sections is expected to be larger than the nuclear breakup cross sections. It is found that the continuum-continuum couplings and the higher-order multipole transitions have stronger effects on the nuclear breakup cross section compared to the Coulomb breakup cross section. The nuclear breakup cross section is observed to be largely important at larger incident angles. We found that the large target charge alone cannot justify the dominance of the Coulomb breakup over its nuclear counterpart. It is demonstrated that the concept of *Coulomb-dominated reaction* might prove to be mainly relative to the prevailing reaction dynamics and not only a large charge of the target nucleus. We conclude that the long-range nature of the Coulomb forces and the large target charge alone cannot explain the strong dominance of the Coulomb breakup over the nuclear breakup in reactions involving heavy targets. These findings can motivate further improvements on the theoretical approaches used in pure Coulomb breakup calculations.

We also studied the effects of resonant and non-resonant states on the breakup cross sections of $^{6}\mathrm{Li} + {}^{209}\mathrm{Bi}$ reaction. In this investigation, we have shown that the angular distributions differential breakup cross section obtained when the resonant and non-resonant states are included in the coupling matrix elements convergences. We found that resonant is strongly dominant for lower energies compare to non-resonant states for higher energies. It is also observed that the calculated data are in agreement with the experimental data for the integrated breakup cross section obtained when both the resonant and non-resonant states are included in the coupling matrix elements. These findings demonstrate that understanding the effects of resonant as well as non-resonant states on the breakup observables play an important role in the investigation of the nuclear structure.

Furthermore, we have analyzed the relevance of Helium-dimer continuum-continuum couplings on the elastic and dissociation cross sections in the $^{4}\mathrm{He}_2 + {}^{4}\mathrm{He} \to {}^{4}\mathrm{He} + {}^{4}\mathrm{He} + {}^{4}\mathrm{He}$ dissociation reaction. We have shown that when the continuum-continuum couplings are included in the coupling matrix elements produces minima and maxima in the elastic scattering cross section, whereas, when they are excluded, the elastic scattering cross section exhibits the well-known behavior, with a maximum in the $E_{c.m.} \to 0$ incident energy region. We also found that these couplings suppress the dissociation cross section, as it is the case in the nuclear dissociation cross sections.

We conclude that the benchmark calculations presented in this study reveal the importance of the continuum-continuum couplings in atomic reactions induced by loosely-bound molecules is exposed for the first time. We argue that these couplings are as important in atomic reactions as they are in nuclear reactions, and should be given attention in the analysis of reactions involving loosely-bound molecules. It could be interesting to extend this study to other loosely-bound molecular systems.

8.2 Future perspectives

One of the envisaged study applying our method, is to investigated the importance of the continuum-continuum coupling in the formation mechanisms for super-heavy elements. A further study of continuum-continuum couplings at deep sub-barrier incident energies with other reaction should be investigated since these couplings reveal an important effect on nuclear astrophysical quantities of interest. Investigated in more detail the importance of the higher-order multi-pole transition and the effects of the continuum-continuum couplings on the nuclear and Coulomb breakups in a reaction that involve a heavy target. In order to further improves on the theoretical approaches used in the calculations of pure Coulomb breakup. Calculated the effects of resonant and non-resonant states on the breakup cross sections of ^{7}Li + ^{209}Bi reaction when both states are included or excluded in the coupling matrix elements with the different incident energies in the range of $23-40$ MeV and partial waves ℓ_{max} =0, 1, 2, 3, 4, 5 and 6. Since the breakup observables of these states play an important role in the investigation of the nuclear structure. One should also investigated the importance of the continuum-continuum couplings in other atomic reactions induced by loosely-bound molecules.

Appendix A: The LM2M2 potential

The general structure of the Helium-Helium semi-realistic LM2M2 potential is [150],

$$V_{\text{HeHe}}(r) = \epsilon[V_b(\zeta) + V_a(\zeta)], \tag{1}$$

where $\zeta = r/r_m$, and $V_b(\zeta)$, is defined as

$$V_b(\zeta) = A\exp(-\alpha\zeta + \beta\zeta^2) - \left(\frac{C_6}{\zeta^6} + \frac{C_8}{\zeta^8} + \frac{C_{10}}{\zeta^{10}}\right)F(\zeta), \tag{2}$$

with

$$F(\zeta) = \begin{cases} \exp[-(D/\zeta - 1)]^2 \text{ if } \quad \zeta \leq D \\ 1 \text{ if } \quad \zeta > D. \end{cases} \tag{3}$$

and

$$V_a(\zeta) = \begin{cases} A_a\Big\{ \sin\left[\frac{2\pi(\zeta-\zeta_1)}{\zeta_2-\zeta_1}\right] + 1\Big\} \text{ if } \quad \zeta_1 \leq \zeta \leq \zeta_2 \\ 0 \text{ if } \quad \zeta \notin [\zeta_1, \zeta_2]. \end{cases} \tag{4}$$

The different parameters are listed in Table 9 of Ref. [139].

Bibliography

[1] I. Tanihata *et al.*, Measurements of interaction cross sections and nuclear radii in the light *p*-shell region, *Phys. Rev. Lett.* **55** 2676 (1985).

[2] I. Tanihata, H. Savajols and R. Kanungo, Recent experimental progress in nuclear halo structure studies, *Prog. Part. Nucl. Phys.* **68** 21 (2013).

[3] V. Jha, V. V. Parkar and S. Kailas, Incomplete fusion reactions using strongly and weakly bound projectiles, *Phys. Rep.* **845** 1 (2020).

[4] L. F. Canto *et al.*, Recent developments in fusion and direct reactions with weakly bound nuclei, *Phys. Rep.* **596** 1 (2015).

[5] L. F. Canto *et al.*, The total reaction cross section of heavy-ion reactions induced by stable and unstable exotic beams: the low-energy regime, *Eur. Phys. J.* **A 56** 281 (2020).

[6] B. B. Back *et al.*, Recent developments in heavy-ion fusion reactions, *Rev. Mod. Phys.* **86** 317 (2014).

[7] H. L. Crawford *et al.*, First Spectroscopy of the Near Drip-line Nucleus ^{40}Mg, *Phys. Rev. Lett.* **122** 052501 (2019).

[8] D. S. Ahn *et al.*, Location of the neutron dripline at fluorine and neon, *Phys. Rev. Lett.* **123** 212501 (2019).

[9] K. J. Cook *et al.*, Halo Structure of the Neutron-Dripline Nucleus ^{19}B, *Phys. Rev. Lett.* **124** 212503 (2020).

[10] J. Casal, Weakly-bound three-body nuclear systems: Structure, reactions and astrophysical implications. Diss. Ph. D. thesis, Universidad de Sevilla (2016).

[11] P. Capel, D. Baye and Y. Suzuki, Coulomb-corrected eikonal description of the breakup of halo nuclei, *Phys. Rev.* **C 78** 054602 (2008).

[12] T. Matsumoto *et al.*, New treatment of breakup continuum in the method of continuum discretized coupled channels, *Phys. Rev.* **C 68** 064607 (2003).

[13] M. Rodríguez-Gallardo, J. M. Arias and J. Gómez-Camacho, Analytical transformed harmonic oscillator basis for three-body nuclei of astrophysical interest: Application to ^{6}He, *Phys. Rev.* **C 69** 034308 (2004).

[14] A. M. Moro *et al.*, Analytical transformed harmonic oscillator basis for continuum discretized coupled channels calculations, *Phys. Rev.* **C 80** 054605 (2009).

[15] J. A. Lay *et al.*, Exploring continuum structures with a pseudo-state basis, *Phys. Rev.* **C 82** 024605 (2010).

[16] T. Matsumoto *et al.*, Four-body CDCC analysis of $^6\mathrm{He} +^{12} \mathrm{C}$ scattering, *Nucl. Phys.* **A 738** 471 (2004).

[17] R. Y. Rasoanaivo and G. H. Rawitscher, Discretization methods of the breakup continuum in deuteron-nucleus collisions, *Phys. Rev.* **C 39** 1709 (1989).

[18] E. Nielsen *et al.*, The three-body problem with short-range interactions, *Phys. Rep.* **347** 373 (2001).

[19] P. Descouvemont, C. Daniel and D. Baye, Three-body systems with Lagrange-mesh techniques in hyperspherical coordinates, *Phys. Rev.* **C 67** 044309 (2003).

[20] M. Rodríguez-Gallardo *et al.*, Three-body continuum discretization in a basis of transformed harmonic oscillator states, *Phys. Rev.* **C 72** 024007 (2005).

[21] I. J. Thompson *et al.*, Pauli blocking in three-body models of halo nuclei, *Phys. Rev.* **C 61** 024318 (2000).

[22] J. Casal, M. Rodríguez-Gallardo and J. M. Arias, Analytical transformed harmonic oscillator basis for three-body nuclei of astrophysical interest: Application to ^{6}He, *Phys. Rev.* **C 88** 014327 (2013).

[23] M. V. Zhukov *et al.*, Bound state properties of Borromean halo nuclei: ^{6}He and ^{11}Li, *Phys. Rep.* **231** 151 (1993).

[24] E. H. S. Burhop *et al.*, K-meson capture by nuclei and the existence of a neutron halo in heavy nuclei, *Nucl. Phys.* **A 132** 625 (1969).

[25] D. J. Millener *et al.*, Strong E1 transitions in ^{9}Be, ^{11}Be, and ^{13}C, *Phys. Rev.* **C 28** 497 (1983).

[26] I. Tanihata *et al.*, Measurements of interaction cross section and radii of He isotopes, *Phys. Lett.* **B 160** 380 (1985).

[27] E. Arnold *et al.*, Quadrupole moment of ^{11}Li, *Phys. Lett.* **B 281** 16 (1992).

[28] J. A. Lay *et al.*, Particle motion in a deformed potential using a transformed oscillator basis, *Phys. Rev.* **C 85** 054618 (2012).

[29] K. Riisager, Nuclear halo states, *Rev. Mod. Phys.* **66** 1105 (1994).

[30] P. G. Hansen, A. S. Jensen and B. Jonson, Nuclear halos, *Annu. Rev. Nucl. Part. Sci.* **45** 591 (1995).

[31] B. Mukeru, T. Frederico and L. Tomio, Weakly bound halo breakup of neutron-^{7}Li and nucleon-^{7}Be on a lead target, *Phys. Rev.* **C 102** 064623 (2020).

[32] B. M. Sherrill, The nature and reactions of halo nuclei, *Nucl. Phys.* **A 685** 134 (2001).

[33] J. S. Al-Khalili, *Lect. Notes Phys.* **651** 77 (2004).

[34] M. Cubero *et al.*, Do Halo Nuclei Follow Rutherford Elastic Scattering at Energies Below the Barrier? The Case of ^{11}Li, *Phys. Rev. Lett.* **109** 262701 (2012).

[35] A. M. Moro and J. A. Lay, Interplay between valence and core excitation mechanisms in the breakup of halo nuclei, *Phys. Rev. Lett.* **109** 232502 (2012).

[36] J. P. Fernández-García *et al.*, Simultaneous analysis of the elastic scattering and breakup channel for the reaction ^{11}Li $+^{208}$ Pb at energies near the Coulomb barrier, *Phys. Rev.* **C 92** 044608 (2015).

[37] R. de Diego *et al.*, Continuum-discretized coupled-channels calculations with core excitation, *Phys. Rev.* **C 89** 064609 (2014).

[38] D. R. Otomar *et al.*, Theoretical study of the elastic breakup of weakly bound nuclei at near-barrier energies, *Phys. Rev.* **C 92** 064609 (2015).

[39] G. R. Kelly *et al.*, α breakup of ^{6}Li and ^{7}Li near the Coulomb barrier, *Phys. Rev.* **C 63** 024601 (2000).

[40] N. C. Summers and F. M. Nunes, Extracting (n, γ) direct capture cross sections from Coulomb dissociation: Application to ^{14}C (n, γ) ^{15}C, *Phys. Rev.* **C 78** 011601(R) (2008).

[41] R. Chatterjee, Beam energy dependence of Coulomb-nuclear interference in the breakup of ^{11}Be, *Phys. Rev.* **C 75** 064604 (2007).

[42] T. Tarutina and M. S. Hussein, Interference effects in the Coulomb dissociation of ^{15,17,19}C, *Phys. Rev.* **C 70** 034603 (2004).

[43] B. Mukeru, M. L. Lekala and A. S. Denikin, Role of the diagonal and off-diagonal continuum–continuum couplings in the breakup of ^{8}B and ^{19}C on ^{58}Ni and ^{208}Pb targets, *Nucl. Phys.* **A 935** 18 (2015).

[44] L. F. Canto *et al.*, Continuum-continuum coupling and polarization potentials for weakly bound systems, *Phys. Rev.* **C 80** 047601 (2009).

[45] J. Lubian *et al.*, Effects of breakup couplings on ^{8}B $+^{58}$ Ni elastic scattering, *Phys. Rev.* **C 79** 064605 (2009).

[46] F. M. Nunes and I. J. Thompson, Nuclear interference effects in ^{8}B sub-Coulomb breakup, *Phys. Rev.* **C 57** R2818-R2820 (1998).

[47] B. Mukeru, G. J. Rampho and M. L. Lekala, Breakup and fusion cross sections of the ^{6}Li nucleus with targets of mass A= 58, 144 and 208, *J. Phys. G: Nucl. Part. Phys.* **45** 045101 11 (2018).

[48] K. J. Cook *et al.*, Interplay of charge clustering and weak binding in reactions of ^{8}Li, *Phys. Rev.* **C 97** 021601(R) (2018).

[49] K. J. Cook *et al.*, Origins of Incomplete Fusion Products and the Suppression of Complete Fusion in Reactions of ^{7}Li, *Phys. Rev. Lett.* **122** 102501 (2019).

[50] K. J. Cook *et al.*, Importance of lifetime effects in breakup and suppression of complete fusion in reactions of weakly bound nuclei, *Phys. Rev.* **C 93** 064604 (2016).

[51] S. Kalkal *et al.*, Asymptotic and near-target direct breakup of ^{6}Li and ^{7}Li, *Phys. Rev.* **C 93** 044605 (2016).

[52] E. C. Simpson *et al.*, Disintegration locations in $^{7}\mathrm{Li} \rightarrow ^{8}$ Be transfer-triggered breakup at near-barrier energies, *Phys. Rev.* **C 93** 024605 (2016).

[53] M. Tokieda and K. Hagino, A new approach for open quantum systems based on a phonon number representation of a harmonic oscillator bath, *Ann. Phys.* **412** 168005 (2020).

[54] C. A. Bertulani and G. Baur, Electromagnetic processes in relativistic heavy ion collisions, *Phys. Rep.* **163** 299 (1988).

[55] G. Baur and H. Rebel, Coulomb breakup of nuclei—applications to astrophysics, *Annu. Rev. Nucl. Part. Sci.* **46** 321 (1996).

[56] F. Luo, C. F. Giese and W. R. Gentry, Direct measurement of the size of the helium dimer, *J. Chem. Phys.* **104** 1151 (1996).

[57] U. Buck and H. Meyer, Electron bombardment fragmentation of Ar van der Waals clusters by scattering analysis, *J. Chem. Phys.* **84** 4854 (1986).

[58] O. Echt, K. Sattler and E. Recknagel, Magic numbers for sphere packings: experimental verification in free xenon clusters, *Phys. Rev. Lett.* **47** 1121 (1981).

[59] E. A. Kolganovay, A. K. Motovilovz and S. A. Sofianos, Three-body configuration space calculations with hard-core potentials, *J. Phys. B: At. Mol. Opt. Phys.* **31** 1279 (1998).

[60] A. K. Motovilov, S. A. Sofianos and E. A. Kolganova, Bound states and scattering processes in the $^4He_3$ atomic system, *Chem. Phys. Lett.* **275** 168 (1997).

[61] T. P. Russell, B. W. Robert and B. K. Kendrick, Three-body collision contributions to recombination and collision-induced dissociation. I. Cross sections, *J. Chem. Phys.* **109** 6701 (1998).

[62] Y. Iseri *et al.*, Chapter IV. Coupled-Channels Approach to Deuteron and 3He Breakup Reactions, *Prog. Theor. Phys. Suppl.* **89** 84 (1986).

[63] N. Austern *et al.*, Continuum-discretized coupled-channels calculations for three-body models of deuteron-nucleus reactions, *Phys. Rep.* **154** 125-204 (1987).

[64] F. d. A. Souza *et al.*, Reaction mechanisms in the ^{6}Li+^{59}Co system, *Nucl. Phys.* **A 821** 36-50 (2009).

[65] B. Mukeru, Proton-halo breakup dynamics for the breakup threshold in the $\varepsilon_0 \to 0$ limit, *Chin. Phys.* **C 45** 054107 (2021).

[66] B. Mukeru, Coulomb and nuclear interactions in the dynamics of weakly-bound neutron-halo breakup on heavy target, *J. Phys. Comm.* **5** 075004 (2021).

[67] I. J. Thompson, Coupled reaction channels calculations in nuclear physics, *Comput. Phys. Rep.* **7** 167 (1988).

[68] A. Pakou *et al.*, Dominance of direct reaction channels at deep sub-barrier energies for weakly bound nuclei on heavy targets: The case $^8\mathrm{B} +^{208}\mathrm{Pb}$, *Phys. Rev.* **C 102** 031601(R) (2020).

[69] C. A. Bertulani, The astrophysical reactions $^{12}\mathrm{C}(\alpha,\gamma)^{16}\mathrm{O}$ and $^7\mathrm{Be}(\mathrm{p},\gamma)^8\mathrm{B}$ and Coulomb dissociation experiments, *Phys. Rev.* **C 49** 2688 (1994).

[70] H. Esbensen, G. F. Bertsch and K. A. Snover, Reconciling Coulomb dissociation and radiative capture measurements, *Phys. Rev. Lett.* **94** 042502 (2005).

[71] A. Di Pietro *et al.*, Elastic scattering and reaction mechanisms of the halo nucleus ^{11}Be around the Coulomb barrier, *Phys. Rev. Lett.* **105** 022701 (2010).

[72] B. Mukeru and M. L. Lekala, First-order and higher-order interferences in the ^{15}C+^{208} Pb and ^{11}Be +^{208} Pb reactions, *Phys. Rev.* **C 91** 064609 (2015).

[73] P. Capel, D. Baye and V. S. Melezhik, Time-dependent analysis of the breakup of halo nuclei, *Phys. Rev* . **C 68** 014612 (2003).

[74] A. Di Pietro *et al.*, Experimental study of the collision ^{11}Be+^{64}Zn around the coulomb barrier, *Phys. Rev.* **C 85** 054607 (2012).

[75] N. Fukuda *et al.*, Coulomb and nuclear breakup of a halo nucleus ^{11}Be, *Phys. Rev.* **C 70** 054606 (2004).

[76] W. Y. So *et al.*, Inelastic scattering of ^{11}Be +^{197} Au to the first excited state in ^{11}Be, *Phys. Rev.* **C 92** 044618 (2015).

[77] R. Palit *et al.*, Exclusive measurement of breakup reactions with the one-neutron halo nucleus ^{11}Be, *Phys. Rev.* **C 68** 034318 (2003).

[78] T. Tarutina, L. C. Chamon and M. S. Hussein, Coulomb excitation of ^{11}Be reexamined, *Phys. Rev.* **C 67** 044605 (2003).

[79] R. Chatterjee and R. Shyam, Coulomb-nuclear interference in the breakup of ^{11}Be, *Phys. Rev.* **C 66** 061601(R) (2002).

[80] V. K. Lukyanov *et al.*, Microscopic analysis of ^{10,11}Be elastic scattering on protons and nuclei, and breakup processes of ^{11}Be within the ^{10}Be $+ n$ cluster model, *Phys. Rev.* **C 91** 034606 (2015).

[81] A. M. Moro and R. Crespo, Core excitation effects in the breakup of the one-neutron halo nucleus ^{11}Be on a proton target, *Phys. Rev.* **C 85** 054613 (2012).

[82] V. Pesudo *et al.*, Scattering of the Halo Nucleus ^{11}Be on ^{197}Au at Energies around the Coulomb Barrier, *Phys. Rev. Lett.* **118** 152502 (2017).

[83] A. Di Pietro *et al.*, Insights into the dynamics of breakup of the halo nucleus ^{11}Be on a ^{64}Zn target, *Phys. Lett.* **B 798** 134954 (2019).

[84] A. Diaz-Torres and I. J. Thompson, Effect of continuum couplings in fusion of halo ^{11}Be on ^{208}Pb around the Coulomb barrier, *Phys. Rev.* **C 65** 024606 (2002).

[85] S. Typel and R. Shyam, Dynamical description of the breakup of one-neutron halo nuclei ^{11}Be and ^{19}C, *Phys. Rev.* **C 64** 024605 (2001).

[86] M. Y. M. Hassan *et al.*, Elastic scattering and breakup effect analysis of $^{11}\mathrm{Be} +^{12}\mathrm{C}$ at 38.4 MeV/nucleon, *Phys. Rev.* **C 79** 064608 (2009).

[87] Y. Y. Yang, X. Liu and D. Y. Pang, Distinction between elastic scattering of weakly bound proton-and neutron-rich nuclei: The case of ^{8}B and ^{11}Be, *Phys. Rev.* **C 94** 034614 (2016).

[88] T. Kido, K. Yabana and Y. Suzuki, Coulomb breakup mechanism of neutron-halo nuclei in a time-dependent method, *Phys. Rev.* **C 53** 2296 (1996).

[89] A. Abramowitz and A. I. Stegun, Handbook of Mathematical Functions with Formulas, Graphs, and Mathematical Tables (Washington, DC: National Bureau of Standards 1964).

[90] K. Riisager, A. S. Jensen and P. Moller, Two-body halos, *Nucl. Phys.* **A 548** 393 (1992).

[91] J. Okolowicz *et al.*, Asymptotic normalization coefficients and continuum coupling in mirror nuclei, *Phys. Rev.* **C 85** 064320 (2012).

[92] I. J. Thompson and F. M. Nunes, Nuclear Reactions for Astrophysics (Cambridge University Press, New York 2009). See also www.fresco.org.uk.

[93] F. M. Nunes and I. J. Thompson, Multistep effects in sub-Coulomb breakup, *Phys. Rev.* **59** 2652-2659 (1999).

[94] D. Baye, Breakup reaction models for exotic nuclei, *Eur. Phys. J. Sp. Top.* **156** 93-122 (2008).

[95] Y. Sukaragi, Energy and target dependence of projectile breakup effect in elastic scattering of ^{6}Li, *Phys. Rev.* **C 35** 2161 (1987).

[96] Y. Hirabayashi and Y. Sukaragi, Evidence for strong nuclear-breakup contribution to α+d breakup by ^{208}Pb at forward angles, *Phys. Rev. Lett.* **69** 1892 (1992).

[97] D. M. Brink and G. R. Satchler, Angular Momentum (Clarendon Press 1994), 3rd ed.

[98] P. Fröbrich and P. Lipperheide, Theory of Nuclear Reactions, Oxford (1996).

[99] R. Bass, Nuclear Reactions with heavy ions, Springer-Verlag (1980).

[100] K. Alder and A. Winther, Electromagnetic Excitation: Theory of Coulomb Excitation with Heavy Ions (North-Holland, Amsterdam 1975).

[101] J. A. Tostevin, F. M. Nunes and I. J. Thompson, Calculations of three-body observables in ^{8}B breakup, *Phys. Rev.* **C 63** 024617 (2001).

[102] T. Matsumoto *et al.*, Smoothing method of discrete breakup S-matrix elements in the theory of continuum-discretized coupled channels, *Progr. Theor. Phys.* **121** 885-894 (2009).

[103] T. Egami *et al.*, Description of four-body breakup reaction with the method of continuum-discretized coupled-channels, *Progr. Theor. Phys.* **121** 789-807 (2009).

[104] G. Goldstein, Description de la dissociation de noyaux á halo par l'approximation eikonale dynamique, PhD thesis, Université Libre de Bruxelles (2007).

[105] G. Baur, K. Hencken and D. Trautmann, Electromagnetic dissociation as a tool for nuclear structure and astrophysics, *Prog. Part. Nucl. Phys.* **51** 487 (2003).

[106] K. Alder *et al.*, Study of nuclear structure by electromagnetic excitation with accelerated ions, *Rev. Mod. Phys.* **28** 432 (1956).

[107] T. Nakamura *et al.*, Neutron capture cross section of ^{14}C of astrophysical interest studied by Coulomb breakup of ^{15}C, *Phys. Rev.* **C 79** 035805 (2009).

[108] D. Baye and P. Capel, In Clusters in Nuclei, *vol.* **2**, pp. 121-163. Springer, Berlin, Heidelberg (2012).

[109] T. Nakamura *et al.*, Coulomb dissociation of a halo nucleus ^{11}Be at 72A MeV, *Phys. Lett.* **B 331** 296-301 (1994).

[110] H. Esbensen and C. A. Bertulani, Multipole expansion for relativistic Coulomb excitation, *Phys. Rev.* **C 65** 024605 (2002).

[111] W. Wang *et al.*, The AME2016 atomic mass evaluation, *Chin. Phys.* **C 41** 030003 (2017),

See also at https://www.nndc.bnl.gov/nudat2/.

[112] H. Esbensen and G. F. Bertsch, Effects of E2 transitions in the Coulomb dissociation of ^{8}B, *Nucl. Phys.* **A 600** 37 (1996).

[113] M. Mazzocco *et al.*, Elastic scattering for the ^{8}B and ^{7}Be $+^{208}$ Pb systems at near-Coulomb barrier energies, *Phys. Rev.* **C 100** 024602 (2019).

[114] J. Cook, Global optical-model potentials for the elastic scattering of ^{6,7}Li projectiles, *Nucl. Phys.* **A 388** 153 (1982).

[115] L. C. Chamon *et al.*, Toward a global description of the nucleus-nucleus interaction, *Phys. Rev.* **C 66** 014610 (2002).

[116] A. Diaz-Torres and I. J. Thompson, Effect of continuum couplings in fusion of halo ^{11}Be on ^{208}Pb around the Coulomb barrier, *Phys. Rev.* **C 65** 024606 (2002).

[117] Evaluated Nuclear Structure Data File (NNDC, BNL, USA),

http://www.nndc.bnl.gov/ensdf/.

[118] F. D. Becchetti and G. W. Greenless, Nucleon-nucleus optical-model parameters, A$>$ 40, E$<$ 50 MeV, *Phys. Rev.* **C 182** 1190 (1969).

[119] H. Esbensen and G. F. Bertsch, Soft dipole excitations in ^{11}Li, *Nucl. Phys.* **A 542** 310 (1992).

[120] N. Kobayashi *et al.*, Observation of a *p*-Wave One-Neutron Halo Configuration in ^{37}Mg, *Phys. Rev. Lett.* **112** 242501 (2014).

[121] K. Yoshida *et al.*, Extracting the electric dipole breakup cross section of one-neutron halo nuclei from inclusive breakup observables, *Prog. Theor. Exp. Phys.* 053D03 (2014).

[122] F. F. Duan *et al.*, Scattering of the halo nucleus ^{11}Be from a lead target at 3.5 times the Coulomb barrier energy, *Phys. Lett.* **B 811** 135942 (2020).

[123] R. O. Akyuz and A. Winther 1979 Proc. Enrico Fermi Int. School of Physics, Nuclear structure and heavy-ion reactions, ed. R. A. Broglia, C. H. Dasso and R. Ricci (North-Holland, Amsterdam 1981) p.491.

[124] B. Mukeru, Comparative analysis of s-wave and p-wave breakups in ^{37}Mg $+^{208}$ Pb reaction, *Int. J. Mod. Phys.* **E 30** 2150006 (2021).

[125] E. Sauvan *et al.*, One-neutron removal reactions on neutron-rich *psd*-shell nuclei, *Phys. Lett.* **B 491** 1 (2000).

[126] D. Bazin *et al.*, Probing the halo structure of ^{19,17,15}C and ^{14}B, *Phys. Rev.* **C 57** 2156 (1998).

[127] F. Ajzenberg-Selove, Energy Levels of Light Nuclei A= 14, *Nucl. Phys.* **A 523** 1 (1991).

[128] A. S. Jensen *et al.*, Structure and reactions of quantum halos, *Rev. Mod. Phys.* **76** 215 (2004).

[129] T. Nakamura *et al.*, Coulomb Dissociation of ^{19}C and its Halo Structure, *Phys. Rev. Lett.* **83** 1112 (1999).

[130] C. A. Bertulani, RADCAP: A potential model tool for direct capture reactions, *Comput. Phys. Commun.* **156** 123-141 (2003).

[131] A. Diaz-Torres, I. J. Thompson and C. Beck, How does breakup influence the total fusion of ^{6,7}Li at the Coulomb barrier?, *Phys. Rev.* **C 68** 044607 (2003).

[132] S. Santra, Reaction mechanisms involving weakly bound ^{6}Li and ^{209}Bi at energies near the Coulomb barrier, *Phys. Rev.* **C 83** 034616 (2011).

[133] D. Patel *et al.*, Fusion barrier distributions in ^{6,7}Li+^{209}Bi reactions from quasi-elastic and fusion excitation function measurements, *Phys. Rev.* **C 89** 064614 (2014).

[134] F. Luo *et al.*, The weakest bond: Experimental observation of helium dimer, *J. Chem Phys.* **98** 3564 (1993).

[135] W. Schöllkopf and J. P. Toennies, Nondestructive mass selection of small van der Waals clusters, Science **266** 1345 (1994).

[136] E. Nielsen, D. V. Fedorov and A. S. Jensen, The structure of the atomic helium trimers: halos and Efimov states, *J. Phys.* **B 31** 4085 (1998).

[137] A. Kievsky *et al.*, The helium trimer with soft-core potentials. Few-Body Syst., **51** 259-269 (2011).

[138] A. Kievsky *et al.*, Structure and dynamics of few-helium clusters using soft-core potentials, *Phys. Atomic Nucl.* **77** 463-471 (2014).

[139] A. K. Motovilov *et al.*, Binding energies and scattering observables in the ^{4}He$_3$ atomic system, *Eur. Phys. J.* **D 13** 33 (2001).

[140] H. S. Huber and T. K. Lim, A study of the Efimov states and binding energies of the helium trimer through the Faddeev-coordinate–momentum approach, *J. Chem. Phys.* **68** 1006-1012 (1978).

[141] S. Rybak, K. Szalewicz and B. Jeziorski, An accurate calculation of the first-order interaction energy for the helium dimer, *J. Chem. Phys.* **91** 4779-4784 (1989).

[142] V. F. Lotrich and K. Szalewicz, Perturbation theory of three-body exchange nonadditivity and application to helium trimer, *J. Chem. Phys.* **112** 112-121 (2000).

[143] D. Blume and C. H. Greene, Monte Carlo hyperspherical description of helium cluster excited states, *J. Chem. Phys.* **112** 8053-8067 (2000).

[144] M. I. Haftel and T. K. Lim, Atom–diatom processes in helium: The multiple-scattering description of elastic and dissociative collisions, *J. Chem. Phys.* **77** 4515-4521 (1982).

[145] H. Suno and B. D. Esry, Adiabatic hyperspherical study of triatomic helium systems, *Phys. Rev.* **A 78** 062701 (2008).

[146] E. Garrido *et al.*, Integral relations and the adiabatic expansion method for 1+ 2 reactions above the breakup threshold: Helium trimers with soft-core potentials, *Phys. Rev.* **A 86** 052709 (2012).

[147] A. Deltuva, Momentum-Space Calculation of ^{4}He Triatomic System with Realistic Potential, *Few-Body Syst.* **56**, 897-903 (2015).

[148] E. Garrido, M. Gattobigio and A. Kievsky, Recombination rates from potential models close to the unitary limit, *Phys. Rev.* **A 88** 032701 (2013).

[149] B. Mukeru B, M. L. Lekala and A. S. Denikin, Study of the effects of nuclear and Coulomb interactions in the breakup of ^{19}C on ^{208}Pb, *J. Phys. G: Nucl. Part. Phys.* **42** 015109 (2014).

[150] R. A. Aziz and M. J. Slaman, An examination of abinitio results for the helium potential energy curve, *J. Chem. Phys.* **94** 8047 (1991).